International Materials Reviews

ISSN: (Print) (Online) Journal homepage: https://www.tandfonline.com/loi/yimr20

Physical metallurgy of medium-Mn advanced high-strength steels

Binhan Sun, Alisson Kwiatkowski da Silva, Yuxiang Wu, Yan Ma, Hao Chen, Colin Scott, Dirk Ponge & Dierk Raabe

To cite this article: Binhan Sun, Alisson Kwiatkowski da Silva, Yuxiang Wu, Yan Ma, Hao Chen, Colin Scott, Dirk Ponge & Dierk Raabe (2023): Physical metallurgy of medium-Mn advanced high-strength steels, International Materials Reviews, DOI: 10.1080/09506608.2022.2153220

To link to this article: https://doi.org/10.1080/09506608.2022.2153220

Published online: 12 Jan 2023.

INTERNATIONAL MATERIALS REVIEWS
https://doi.org/10.1080/09506608.2022.2153220

Physical metallurgy of medium-Mn advanced high-strength steels

Binhan Sun [a,b], Alisson Kwiatkowski da Silva[b], Yuxiang Wu[b], Yan Ma[b], Hao Chen[c], Colin Scott[d], Dirk Ponge[b] and Dierk Raabe[b]

[a]Key Laboratory of Pressure Systems and Safety, Ministry of Education, School of Mechanical and Power Engineering, East China University of Science and Technology, Shanghai, People's Republic of China; [b]Max-Planck-Institut für Eisenforschung, Düsseldorf, Germany; [c]Key Laboratory for Advanced Materials of Ministry of Education, School of Materials Science and Engineering, Tsinghua University, Beijing, People's Republic of China; [d]CanmetMATERIALS, Natural Resources Canada, Hamilton, Canada

ABSTRACT

Steels with medium manganese (Mn) content (3~12 wt-%) have emerged as a new alloy class and received considerable attention during the last decade. The microstructure and mechanical response of such alloys show significant differences from those of established steel grades, especially pertaining to the microstructural variety that can be tuned and the associated micromechanisms activated during deformation. The interplay and tuning opportunities between composition and the many microstructural features allow to trigger almost all known strengthening and strain-hardening mechanisms, enabling excellent strength-ductility synergy, at relatively lean alloy content. Previous investigations have revealed a high degree of microstructure and deformation complexity in such steels, but the underlying mechanisms are not adequately discussed and acknowledged. This encourages us to critically review and discuss these materials, focusing on the progress in fundamental research, with the aim to obtain better understanding and enable further progress in this field. The review addresses the main phase transformation phenomena in these steels and their mechanical behaviour, covering the whole inelastic deformation regime including yielding, strain hardening, plastic instability and damage. Based on these insights, the relationships between processing, microstructure and mechanical properties are critically assessed and rationalized. Open questions and challenges with respect to both, fundamental studies and industrial production are also identified and discussed to guide future research efforts.

ARTICLE HISTORY
Received 5 June 2022
Accepted 22 November 2022

KEYWORDS
Medium-Mn steels; advanced high-strength steels; microstructure; mechanical properties; phase transformation; damage

Introduction

Medium-Mn steels (MMnS) commonly refer to a class of Fe-based alloys with an Mn content between low-Mn (<3 wt-%) first-generation and high-Mn (>13 wt-%) second-generation advanced high-strength steels (AHSS). These materials, originally introduced in the 1970s by Miller [1], have received considerable attention in the last decade. This interest was driven by the increasing demand for sustainable, compositionally lean, strong and ductile steels, especially in the automotive sector, for enabling parts with high weight reduction and good damage tolerance. Although first considered as a composition-efficient, lean alternative to high-Mn AHSS, they have now emerged as an entirely new material class which shows great potential to become one of the next-generation AHSS (the so-called third generation). They differ significantly from other types of steels, particularly with respect to composition and microstructure along four dimensions of complexity, which can all be tuned, individually, or in concert. These include (a) chemical composition and inter-phase solute partitioning [2–10]; (b) microstructure variety in terms of phases and microstructure constituents (e.g. austenite, ferrite, martensite, bainite, pearlite and carbides), including their size, dispersion, morphology, distribution and percolation [2–6,11–19]; (c) microscopic solute enrichment/segregation to the multiple defects with several opportunities for segregation functionalization [15,19–23]; (d) austenite mechanical stability/metastability design and the associated dislocation and athermal deformation mechanisms and defect patterning phenomena [3,4,6,7,9,10,14,18,24]. The interplay and tuning among these several alloy dimensions allow to trigger practically almost all known strengthening and strain-hardening mechanisms, e.g. solid solution strengthening, interface strengthening, precipitation strengthening, dislocation strengthening, transformation-induced plasticity (TRIP) effect, twinning-induced plasticity (TWIP) effect, dynamic strain

CONTACT Binhan Sun binhan.sun@ecust.edu.cn Key Laboratory of Pressure Systems and Safety, Ministry of Education, School of Mechanical and Power Engineering, East China University of Science and Technology, Shanghai 200237, People's Republic of China, Max-Planck-Institut für Eisenforschung, Düsseldorf 40237, Germany; Hao Chen hao.chen@mail.tsinghua.edu.cn Key Laboratory for Advanced Materials of Ministry of Education, School of Materials Science and Engineering, Tsinghua University, Beijing 100084, People's Republic of China; Dierk Raabe d.raabe@mpie.de Max-Planck-Institut für Eisenforschung, Düsseldorf, Germany

aging and multiphase composite strengthening effect. This large variety of micromechanical strengthening mechanisms, all assembled within a well-tuneable composition and processing range, opens wide access to the design of materials with excellent strength-ductility synergy (tensile strength up to ~2400 MPa [25], total elongation up to ~95% [26], product of tensile strength and total elongation up to 80 GPa% [14,26,27]) at relatively lean alloy content. These features qualify MMnS as a generic novel material class. However, such complexity brings about the necessity to better understand the alloys' underlying thermodynamics, kinetics and deformation mechanisms, as well as the underlying interplay among composition, microstructure and transformation when they are manufactured and exposed to complex mechanical loading scenarios. A comprehensive and critical review of the physical and micromechanical foundations of this material class is missing, which impedes their further development, efficient processing and responsible use.

Although a few reviews related to MMnS exist [4,6,7,28], they have mainly summarized the engineering and phenomenological features of processing-microstructure-property relations and have mainly covered ultrafine grained grades (globular grain diameter or laminated grain width near or below 1 μm). The present overview aims to focus more on the fundamental microstructure and deformation mechanisms in all types of steels containing a medium-Mn content. Particular focus is placed on the variety of microstructural features and their formation thermodynamics and kinetics. Key differences between these steels and other low-alloyed steels are highlighted. The mechanical behaviour, covering the whole inelastic deformation regime, including yielding, strain hardening, plastic instability and damage (with and without the presence of H) are systematically reviewed and critically evaluated. Based on these insights, the interplay between various available processing routes, resulting microstructure and mechanical response is critically assessed and rationalized, accompanied by a systematic comparison to other high-strength steels. The review aims to provide not only a theoretical framework for accelerating the development of this class of steels, but also to highlight open scientific questions and challenges in this field that require future research efforts, both from an academic and industrial perspective.

Effects of alloying elements

The most common alloying elements in MMnS, in addition to Mn, are carbon (C), aluminium (Al) and silicon (Si), spanning a wide compositional spectrum. Alloy variants discussed so far in the literature have shown to yield most promising mechanical performance at around 0.01~0.7 wt-% for C [29,30], 0~10 wt-% for Al [30] and 0~3 wt-% for Si [9,31]. The complex relationships between the rich microstructure cosmos of these alloys and their many thermomechanical treatment-dependent metallurgical variants (e.g. phase constituents and fractions, grain size and morphology, austenite stability and deformation mechanisms) that have been studied so far, make it challenging to isolate the direct effects of specific elements on the materials' microstructure-related properties [8–10]. As a result, this section focuses primarily on the effect of solutes on phase transformation thermodynamics and individual phase characteristics.

As the most prominent alloy ingredient in MMnS, Mn plays a critical role in stabilizing austenite and retaining it at room temperature. Adding 1 wt-% Mn to austenite results in around 30~40°C reduction in Ms temperature (martensite start temperature) [32–34] and ~10°C decrease in Md_{30} temperature (the temperature where half of the austenite is transformed to martensite at a strain of 30%) [35,36]. As a result, a higher Mn content increases the maximum fraction of accessible retained austenite. For instance, an increase of ~20 vol.-% of retained austenite for an additional content of 2~3 wt-% Mn has been reported in Refs. [3,10]. Mn also decreases the Ae_1 and Ae_3 temperatures, thus shifting the austenite-ferrite intercritical temperature range to lower temperatures [10]. It has been shown for binary Fe-Mn alloys, that the austenite's stacking fault energy (SFE) at room temperature first decreases and then increases with increasing Mn concentration [37–39], resulting in a typical parabolic dependence of the austenite's SFE on the Mn content. It is worth noting that the lowest SFE (bottom portion of the parabolic curve) is obtained for Mn concentrations ranging from 10 to 16 wt-% [39], which is about the actual Mn concentration partitioned into the austenite in the most widely investigated MMnS variant (with 5~10 wt-% Mn). This knowledge is critical for the partitioning design of such alloys, in order to yield the desired effect of the global and partitioned Mn content on the SFE of the austenite. Other important features associated with Mn include: (a) its tendency to segregate to lattice defects (e.g. dislocations, triple points and interfaces [19,20,22,40,41]) and (b) its low diffusivity especially inside the austenite phase [17,18,24]. The former phenomenon, driven by the reduction of the free energy of specific defects in terms of the Gibbs adsorption theorem, alters the chemical composition locally, thus influencing a variety of microstructure and mechanical features including austenite formation and damage tolerance [19,20,22,31,40,41]. The latter feature, namely, the slow diffusion of Mn inside austenite, in relation to rapid austenite reversion, can be used as a fundamental principle for designing unique microstructures with controlled Mn patterning or local enrichment for superior mechanical performance [17,18,24,42].

Carbon, like Mn, has a substantial stabilizing effect on austenite and lowers the Ae_1 and Ae_3 temperatures. It also has a strong solid solution hardening effect, especially for the ferrite/α′-martensite phase: per one wt-% of C, a hardening effect of a few thousands of MPa is possible [10,43]. Furthermore, a higher C content increases the SFE of the austenite significantly, with about 2.5∼4 mJ m^{-2} increase per 0.1 wt-% C [44–46], which strongly influences the deformation behaviour and strain-hardening capability of austenite. Discontinuous yielding and the Portevin-Le Chatelier (PLC) phenomenon (dynamic strain aging) are also profoundly influenced by interactions between C atoms and lattice defects (e.g. dislocations) [23,47–50].

The addition of Al to MMnS is typically used to increase the size of the austenite-ferrite two-phase domain (due to its ferrite stabilizing effect), allowing for improved microstructure control. At the same time, Al reduces the mass density of the steels (by ∼1.3% per 1 wt-% Al addition [2,51]). As a result, a considerable portion of Al (up to 10 wt- %) is sometimes used in MMnS. These steels are also referred to as low-density or lightweight medium-Mn steels [2,5]. Literature shows that an increase of 1 wt-% Al in solid solution results in an increase of the austenite's SFE by ∼8.5 mJ m^{-2} [52–56]. This explains why Al has a suppressive effect on the formation of deformation-induced ε-martensite [57]. In addition, for high-Mn austenitic steels where the austenite can have a similar composition to the austenite in a multiphase MMnS, some further effects of Al have been discovered. These effects were discussed in terms of two main aspects: (a) Al was reported to improve the resistance of TWIP steels to H embrittlement [58]. One possible reason for this might be that Al atoms, acting as weak trapping sites for H due to the local expansion around them, can reduce the effective diffusivity of H inside austenite [59,60]. Another possibility is that, when Al gets enriched in the surface oxides, it suppresses H permeation into the material [61]. (b) The observation that Al increases the apparent activation energy for the initiation of the PLC effect in TWIP steels suggests that Al may reduce the C diffusivity within the core of dislocations [62,63]. However, it should be noted that these apparent activation energies are usually calculated only from the stress serrations on flow curves, an approach which can be error-prone and lead to incorrect interpretations.

In terms of stabilizing ferrite, expanding the intercritical range and lowering mass density, Si has a similar impact as Al. Compared with Al, Si is a more effective solution strengthening element, resulting in an increase in yield strength of ∼120 MPa and up to ∼65 MPa per 1 wt-% Si for ferrite and austenite [9], respectively. The influence of Si on austenite's SFE is complex. It was predicted by Dumay et al. [64], using a thermodynamic model, that Si first increases the SFE for small contents and then decreases it at higher concentrations. However, experimental data showed a decreasing effect of Si on austenite SFE (by 2∼3.5 mJ m^{-2} per 1 wt-% Si) [9]. It should be noted that the addition of Si and Al has a negative impact of promoting the formation of ordering phases such as B2 and $D0_3$ inside ferrite [65,66], an effect which has indeed been observed in a recent study on a 0.2C-10Mn-3Al-3Si (in wt-%) steel [31]. Such ordering effect can induce the formation of dissociated superlattice dislocations, which reduces the dislocation cross-slip frequency and results in high stress concentrations, thereby promoting damage formation in the ferrite phase [31].

In addition to the above-mentioned primary alloying elements, micro-alloying elements, e.g. V [67,68], Nb [69] and Ti [70], have sometimes also been added to MMnS, to provide precipitation hardening. In the field of H embrittlement, there has been a history of using the related carbides as H trapping sites to mitigate H embrittlement [71], although the potency of such measures in MMnS seems not as high as that in ferritic steels [72]. The co-doping of Cu and Ni has also been shown to be effective in introducing a high density of Cu-rich nanosized coherent precipitates [73]. For some MMnS grades that are press-hardened, Cr is sometimes added to improve the oxidation resistance at high temperatures [74]. An enhanced corrosion resistance can also be achieved in MMnS by Cr addition [75].

Phase transformation in medium-Mn steels

Austenite reversion in medium-Mn steels

The mechanical properties of MMnS are highly influenced by the fraction and stability of austenite, which has a significant impact on the steels' strain-hardening capacity and damage tolerance. The thermodynamics and kinetics of austenite formation/reversion during the annealing treatment are thus crucial details that must be understood, in order to enable improved microstructural design via adequate processing pathways. Figure 1 shows the calculated austenite fraction for two MMnS compositions as a function of temperature, as well as the corresponding retained austenite after quenching to room temperature (estimated based on the Koistinen-Marburger equation). The retained austenite fraction in MMnS shows an increase followed by a drop with higher annealing temperatures, due to the reduced thermal stability of austenite (decreased enrichment of C and Mn within austenite) and the formation of quenched-in martensite. While the thermodynamic limit of austenite formation during annealing is indeed clearly defined by these calculations, the actual austenite fraction and solute partitioning are kinetically regulated and they

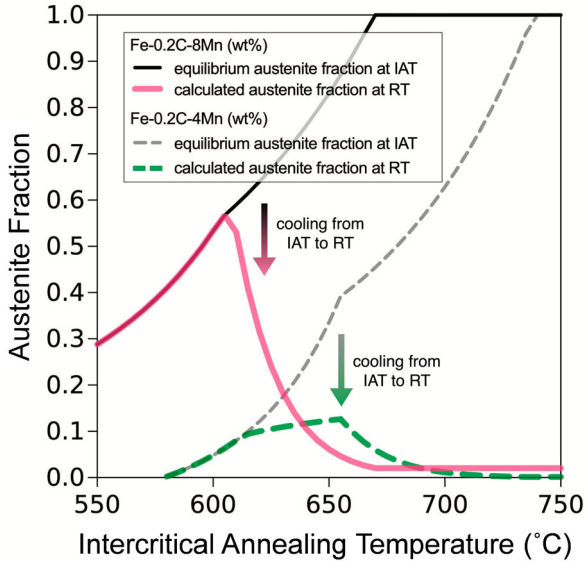

Figure 1. Calculated austenite fraction at the intercritical annealing temperature (IAT) and retained austenite fraction after quenching to room temperature (RT) for two MMnS compositions (Fe-0.2C-8Mn and Fe-0.2C-4Mn, in wt-%). The calculation follows Ref. [76], using the Thermo-calc software in conjunction with the TCFE9 database for a full equilibrium calculation. The Koistinen-Marburger parameters stem from Ref. [77].

frequently diverge significantly from the thermodynamic equilibrium.

A detailed summary of the kinetic aspects of austenite formation in modern AHSS has recently been reviewed by Dai et al. [78]. Here in this contribution, we only focus on the aspects that are most relevant for MMnS. Moving-boundary simulations between austenite and ferrite under a local equilibrium assumption can be used to produce a simplified picture of the austenite growth kinetics [79–81]. A detailed analysis of this approach, in terms of the interfacial tie-line evolutions between austenite and ferrite, has been given by Wei et al. [81]. The diffusional mechanisms in the two phases govern different stages of austenite growth, as shown in Figure 2 (a). The typical operative interfacial tie-lines for stages I and II are indicated in the isothermal sections in Figure 2(b, c), with schematics of C and Mn solute profiles across austenite and ferrite. In this model, austenite transformation starts with a rapid growth controlled by C diffusion in ferrite and in austenite (Figure 2(a) stage I). This is under negligible partitioning local equilibrium (NPLE) interfacial conditions, under which Mn undergoes practically no (hence negligible) partitioning across the interface (schematic solute profile shown in Figure 2(b)). This C diffusion-governed stage is followed by an Mn diffusion-controlled austenite growth stage (stage II), where Mn diffusion in ferrite dominates the increase in austenite fraction. Now the interfacial condition changes from NPLE to the partitioning local equilibrium (PLE), where the interfacial Mn content at both the ferrite and austenite sides changes (Figure 2(c)).

This model picture suggests that the growth of austenite for most MMnS compositions will encounter a first NPLE stage under local equilibrium conditions [82]. Yet, this NPLE stage is usually not observed experimentally at typical intercritical annealing conditions. This suggests that several other factors, such as the interfacial dissipation at the austenite/ferrite migrating interface (i.e. a deviation of local equilibrium assumption) and the presence of carbides in the starting microstructure, might need to be included to improve this simplistic growth model. For example, when carbides are considered during austenite formation, the interfacial thermodynamics for austenite growth will be completely changed in comparison to the consideration of only ferrite and austenite shown in Figure 2 [83,84]. In MMnS, the presence/formation of Mn-partitioned carbides is sometimes inevitable before the formation of intercritical austenite, stemming either from the upstream processing [83,85] or from the heating process during intercritical annealing [82]. These carbides (primarily cementite) can affect the controlling diffusion mechanisms and thus the austenite growth kinetics. Assuming austenite (γ) nucleating and growing from cementite (θ)/ferrite (α) interface (Figure 3(a)), it is possible to compare the C activity at the θ/γ interface and γ/α interface at the beginning of austenite growth. This determines whether a positive C activity gradient in austenite exists and consequently results in C diffusion-controlled austenite growth. In this scenario, the austenite growth mode and growth kinetics are influenced by both the cementite Mn composition and the intercritical annealing temperature. Figure 3(b, c) compare the austenite growth mode between two steel compositions, Fe-0.1C-2Mn vs. Fe-0.2C-5Mn (in wt-%). The data show that at relatively low intercritical temperatures, the austenite growth is Mn diffusion-controlled when carbides are considered in the initial microstructure (simulation configuration shown in Figure 3(a)). At higher temperature, C diffusion-controlled austenite growth becomes prevalent. It is important to compare the transition line separating the two austenite growth modes in respect to the Ae3 temperature. For the medium-Mn composition (Figure 3(c)), it shows that the transition between C- and Mn diffusion-controlled regimes becomes very close to the Ae_3 temperature. This means that only a very small temperature window (less than 40°C) exists for the C-controlled growth of austenite for this MMnS. When the initial cementite is more enriched with Mn (>30% Mn U-fraction in Figure 3(c)), the austenite growth will always be Mn-controlled throughout the whole intercritical range. This agrees with the commonly observed relatively slow austenite reversion

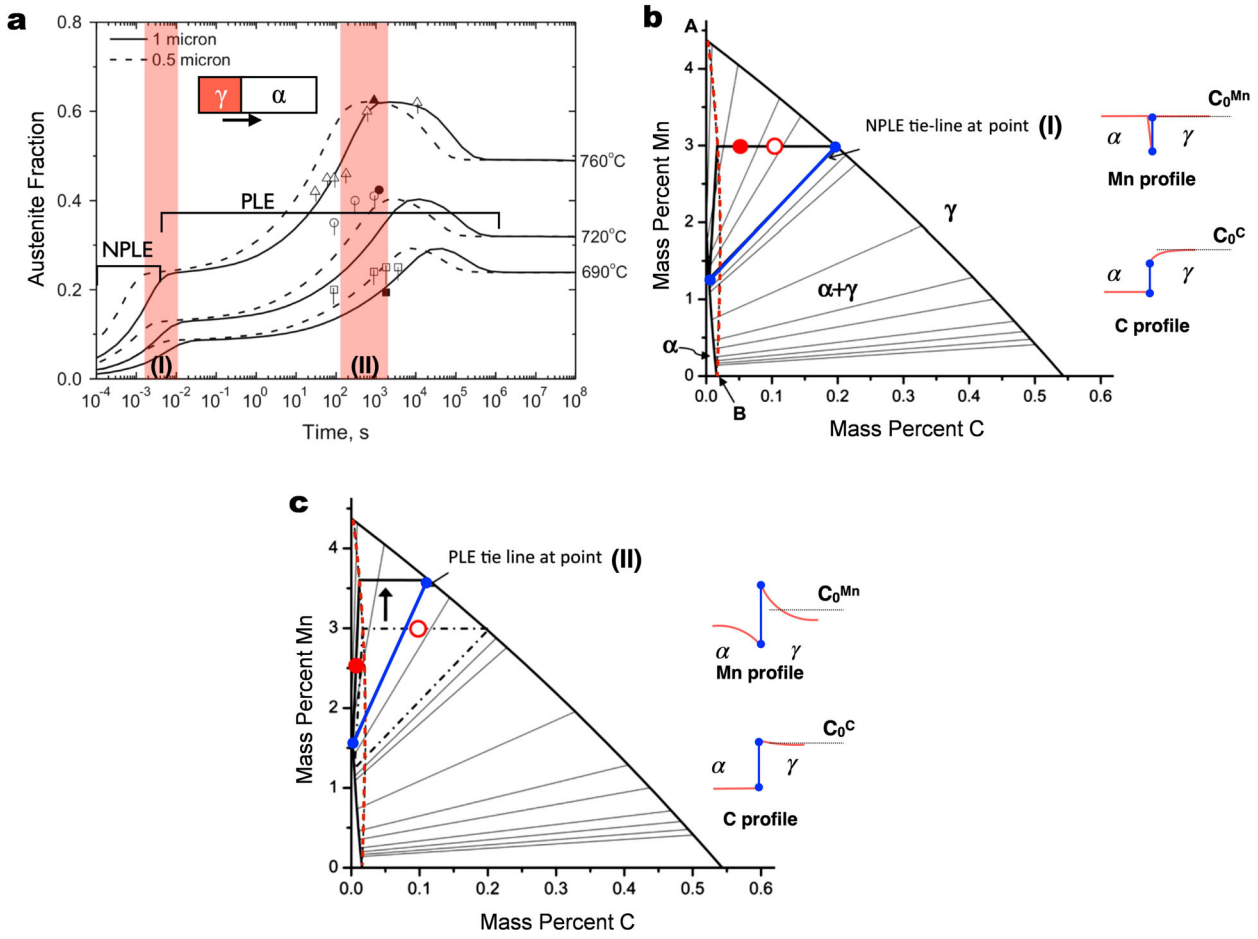

Figure 2. (a) Austenite volume fraction as a function of time for a 0.1C-3Mn-1.5Si (wt-%) steel simulated by using DICTRA for different temperatures, with different growth stages ranging from NPLE boundary conditions to PLE boundary conditions, as highlighted in the figure (two simulation cells with different sizes, 0.5 and 1 μm, have been considered here). (b–d) Illustration of the selection of interfacial tie-lines based on Fe-C-Mn isothermal sections (open circles represent bulk composition and solid circle represent mean composition of ferrite in its current stage): (b) growth under NPLE with fixed tie-line; (c) growth transition from NPLE to PLE with tie-line shifting towards maximum interfacial Mn content in austenite. The schematics of solute profile across the austenite/ferrite interfaces at different stages are included with operative tie-line highlighted. The figure is reconstructed with permission from Ref. [81].

kinetics in MMnS containing carbides in their initial microstructure [86–88].

Another complication related to austenite growth in MMnS is when austenite exists in the initial microstructure. During intercritical annealing, the pre-existing austenite continues to grow, concurrently with the formation of fresh austenite. The growth of pre-existing austenite is influenced by the original solute profiles (especially C and Mn) within it. These two populations of austenite (pre-existing and fresh), containing different solute profiles, would have different growth kinetics and solute partitioning with adjacent phases. Comprehensive thermodynamic and kinetic models that can simultaneously consider the growth of different populations of austenite still need to be developed.

This discussion also indicates the important role of austenite nucleation on its growth kinetics. The influence of this factor is associated with a number of further aspects: (a) The austenite nucleation on carbides changes the thermodynamic boundary conditions of growth models (e.g. Figure 3). The relative location of cementite dissolution, whether it is dissolving within austenite (i.e. austenite nucleating on cementite) or dissolving in the ferrite matrix, has different kinetic effects on austenite growth [86]; (b) The number density of nucleation sites dictates the diffusion field and hence is an important input parameter in any kinetic simulation of austenite growth. Taken the starting microstructure of quenched-in martensite as an example, the nucleation of austenite can occur at numerous interfaces including lath, block and sub-block boundaries (as shown schematically in Figure 4). The large number density of austenite nucleation sites might be relevant to the commonly observed ultrafine austenite grain size in MMnS, an aspect which might deserve further study; (c) The specific nucleation sites influence the interfacial crystallography and the resulting grain morphology and growth (Figure 4). Most laminated austenite, formed from an initial quenched-in martensite,

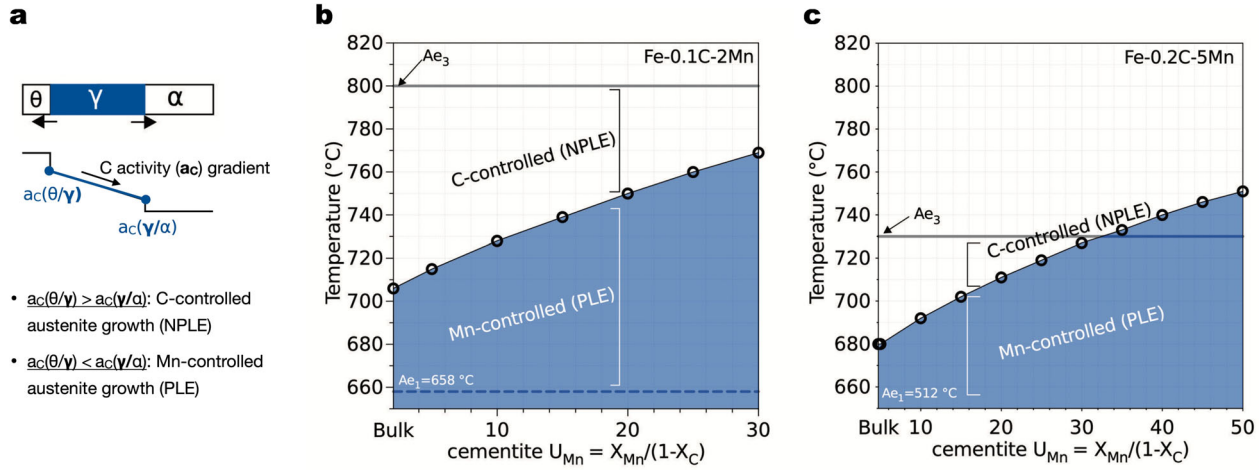

Figure 3. (a) Schematic illustrations of austenite (γ) growing from cementite (θ)/ferrite (α) interface. By comparing the C activity at the θ/γ interface and γ/α interface, this can be used to determine whether a positive C activity gradient in austenite exists and results in the C diffusion-controlled austenite growth; (b, c) The transition between C-diffusion-controlled austenite growth (NPLE) to Mn diffusion-controlled austenite growth (PLE) is plotted, as a function of intercritical annealing temperature and cementite Mn U-fraction. These thermodynamic assessments are made for the comparison between the steel compositions (b) 0.1C-2Mn and (c) 0.2C-5Mn (wt-%). Ae1 and Ae3 are the start and finish temperatures for austenite formation at equilibrium, respectively. The figure is reconstructed with permission from Ref. [83,84].

has a near Kurdjumov-Sachs (K-S) orientation relationship (OR) with the adjacent martensite matrix (Figure 4), i.e. they have almost the same orientation as that of the prior-austenite grain (i.e. the so-called austenite memory effect [89–91]). The growth of these laminated austenite regions is expected to be sluggish and may be explained by the low interface mobility of the semi-coherent K-S austenite-martensite interface. However, the quantitative relation between the interfacial crystallography (e.g. the K-S OR) and the phase boundary mobility has not yet been established [91–93].

In addition to the aforementioned influencing factors, the nucleation, growth kinetics and topological distribution of austenite are also affected by the defect populations introduced by pre-deformation (e.g. cold, warm and hot deformation) before intercritical annealing [94–96]. Although the complicated interaction between austenite formation and recrystallization has been most extensively studied in AHSS with lower Mn contents [94,95,97], the acquired knowledge should be suited to be extended to MMnS. Several studies have suggested an accelerated kinetics of austenite transformation from an initial pre-deformed

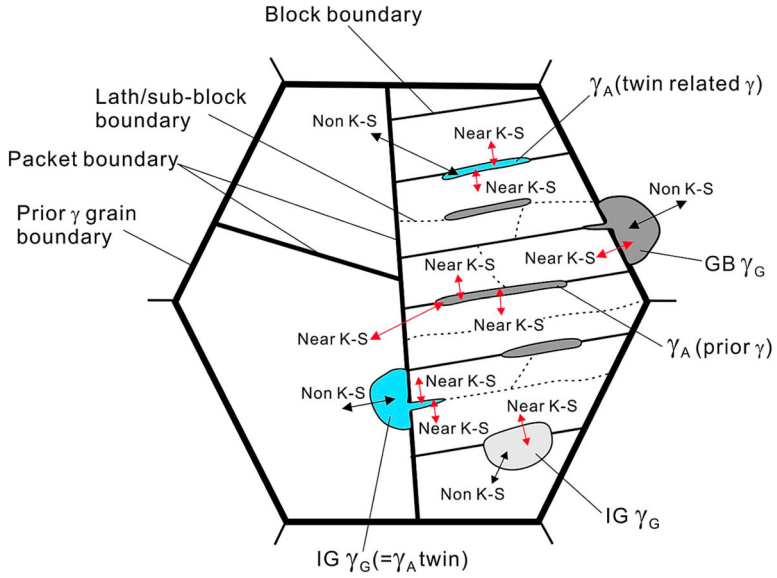

Figure 4. Schematics of austenite growth at different nucleation sites in lath martensite and the evolved OR with the neighbouring phase and the developed austenite morphology, in which GB γ_G represents grain boundary (GB) austenite with globular morphology and IG γ_G/γ_A is intragranular (IG) austenite with globular/acicular morphology. The figure is reprinted with permission from Ref. [91].

microstructure, given that the recrystallization of the microstructure is not complete before the start of austenite formation at the annealing temperature [12,97,98]. This has been explained in part by the increased density of austenite nucleation sites, the lower activation energy for the nucleation and the more rapid diffusivity of substitutional atoms in less recrystallized microstructures [96].

Chemical enrichment/segregation at microstructural defects

Solute segregation is a term that describes a wide variety of chemical heterogeneity features observed in materials. The term is often applied in the metallurgical community to refer to the macro-/micro-segregation which arises as a consequence of solute partitioning to the liquid during solidification [99]. It is also sometimes applied to refer to the phase separation which takes place inside a miscibility gap [100,101]. Here in this section, we refer specifically to the solute segregation to crystalline defects like grain boundaries and dislocations [102]. Solute segregation at defects is a process driven by the minimization of the system's free energy associated with defects. It proceeds via partitioning of solute elements to the defects, up to the composition at which local diffusional equilibrium between bulk and defect is established. The process is thermodynamically analogous to the adsorption of gaseous molecules from a gas phase to the surface of a solid phase. Gibbs described interfaces mathematically analogous to phases in order to explain the adsorption phenomena and obtained a simple expression for the free energy of the interface. When derived for a single temperature, this expression is known as the Gibbs adsorption isotherm.

Mn segregation to grain boundaries and dislocations in the Fe-Mn system has been investigated in some detail during the last years, due to its important role during the austenite reversion in Mn-containing steels [20,41,92,103–105]. The strong tendency for Mn segregation in these steel systems is connected to the ferromagnetism of Fe and the anti-ferromagnetism of Mn, which leads to a positive excess enthalpy of mixing of those elements. For substitutional solid solutions, bond-breaking models provide a good approximation of the Gibbs energy of mixing of the grain boundary by scaling the excess enthalpy of mixing of the solid solution with the coordination number [41,106–108]. According to this model, solid solutions with positive excess enthalpy of mixing tend to partition solutes at lower temperatures to regions of lower average coordination such as grain boundaries or dislocations. This model also successfully predicts the transition from lower to higher segregation regimes and the clustered type of segregation observed experimentally, which has been described as a transient interfacial spinodal phenomena [20,41,109]. Figure 5 shows segregation isotherms at different temperatures calculated using the bond-breaking model proposed in Ref. [41] assuming a fixed reduction of coordination at the grain boundary.

The associated advantage of heterogeneous nucleation at crystalline defects like grain boundaries over homogeneous nucleation lies in the gain in interface energy provided by such a substrate region, an energy that reduces the remaining interfacial area that has to be created by fluctuation. The efficiency of this energy reduction increases with improved wetting of the product phase on the substrate. Additionally, the composition fluctuations observed at solute segregated grain boundaries and dislocations provide a faster kinetic pathway for the nucleation of second phases such as austenite [20,103,104,110]. While the classical nucleation theory describes the formation of the nucleus from solution in a single step by statistical fluctuations, solute segregation may be described as an actual directed diffusional process (with associated interfacial Gibbs energy dissipation), assisting the stochastic process of the nucleus formation. The austenite nucleus will further grow, maintaining the local equilibrium at the interface and depleting both the matrix and the grain boundary in solute Mn. Concomitantly, the Mn content of the austenite decreases until the point where the chemical potential of the austenite equals that of the BCC bulk phase.

The interplay between austenite reversion and grain boundary segregation was proposed by Raabe et al. [19] while investigating the austenite reversion at grain boundaries in a precipitation hardened MMnS using atom probe tomography (APT). The

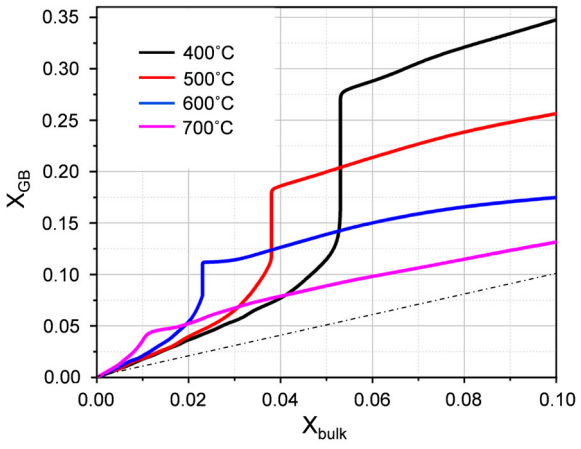

Figure 5. Segregation isotherms at different temperatures assuming metastable local diffusional equilibrium between the BCC bulk phase (coordination number $z = 8$) and the grain boundary (reduced coordination number $z = 6$). X_{Bulk} and X_{GB} refer to the molar fraction of Mn at the bulk and grain boundary, respectively. The figure is reprinted with permission from Ref. [41].

phenomenon was discussed in terms of the adsorption theory in conjunction with classical heterogeneous nucleation theory as well as a phase field model to describe the kinetics of austenite reversion. Kuzmina et al. [22,104] subsequently investigated a Fe-9Mn (wt-%) model alloy and revealed the complex interplay between solute segregation and the strain field of dislocations and its association to the austenite nucleation at those defects. Those studies were followed by the APT observation of compositional fluctuations both at grain boundaries and dislocations which resembled the ones expected for a confined spinodal decomposition [20,111]. Figure 6 exemplifies the detailed analysis in a typical APT dataset from the Fe-9Mn (wt-%) alloy annealed at 450°C for 6 h. The authors proposed that these composition fluctuations provided a non-classical pathway acting as precursors for austenite nucleation. They subsequently provided a thermodynamic model [41] (already discussed above in Figure 5) and a phase field model [109] to describe the observed Mn segregation at grain boundaries. Kwiatkowski da Silva et al. [103] also investigated the effect of C on the Mn segregation to grain boundaries. They found that segregation of C to grain boundaries and dislocations decreased locally the activity of Mn and, as a consequence, the segregation of Mn was enhanced by the presence of C. The increase of the local compositional fluctuations of Mn and C along grain boundaries and dislocations promoted the formation of a first austenite embryo when the amount of C available is not enough to lead to carbide nucleation [103,112].

Role of kinetically stimulated solute heterogeneity in microstructural evolution

In the previous sections, we discussed the redistribution of C and Mn on the basis of thermodynamic equilibrium conditions, both with regard to global and local defect-related partitioning phenomena. We also realized in that context that the kinetic decoupling of fast-diffusing C from the slow-diffusing Mn can be used as a microstructure design mechanism. With regard to the kinetic degrees of freedom, however, there are also a number of other possibilities to influence the distribution of Mn in the microstructure and to use this as an additional valuable design vehicle. The high-Mn content in MMnS, compared to low-alloyed steels, allows to trigger several kinetic mechanisms for producing locally Mn enriched regions in the microstructure, for instance in the form of a non-equilibrium heterogeneous distribution of Mn at the micro- and meso-scale [24,113–115]. Opportunities arise from this approach in terms of utilizing these chemical heterogeneities to kinetically architect novel chemically triggered microstructure patterns

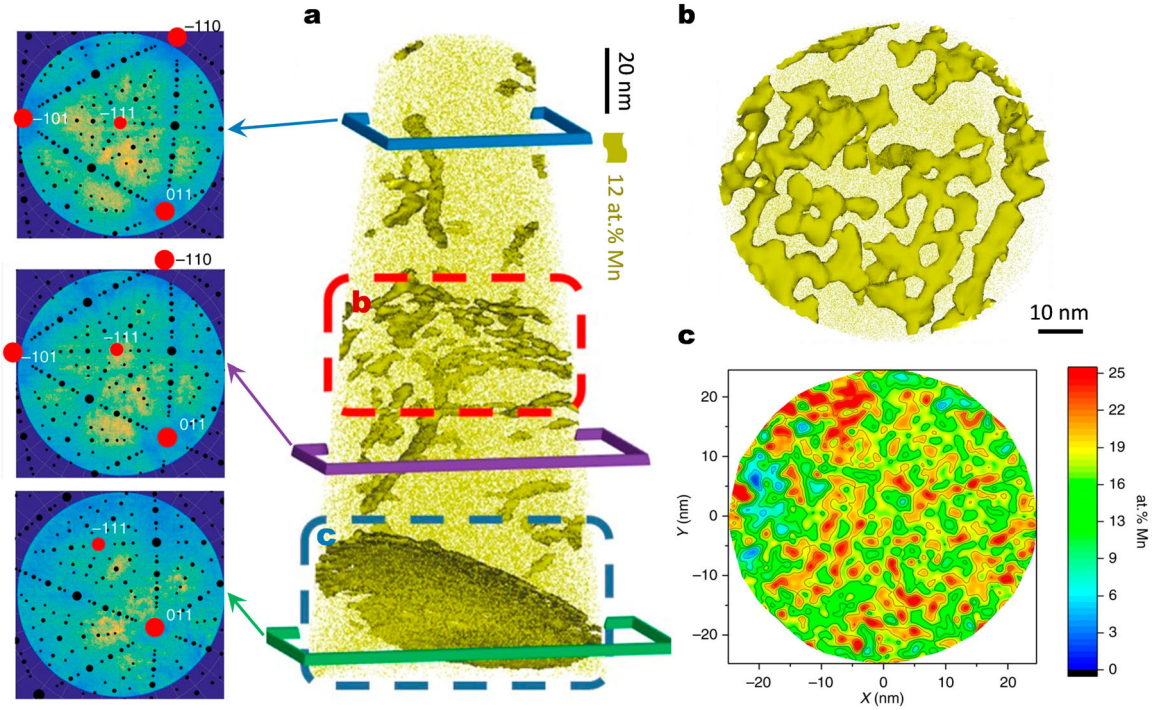

Figure 6. APT analysis of grain boundaries decorated with Mn after 6 h at 450°C. (a) The 12.5 at-% Mn iso-concentration surfaces (12.5 at-% Mn was chosen as a threshold value to highlight Mn-enriched regions). The detector map of the regions marked by the blue, purple and green frames, respectively. The corresponding stereographic projections (black dots) after the identification of the main poles in the map (red dots) were superimposed. (b) Detail of the twisted low-angle grain boundary marked by the red dashed box in (a) as revealed by the iso-concentration surfaces. The grain boundary highlighted by the blue dashed box in (a) was exported and displayed in (c) using an in-plane concentration analysis inside the grain boundary plane. The figure is reconstructed with permission from Ref. [20]).

for enhancing the steels' mechanical properties. Here we summarize several streams of activities being explored in the community along such lines.

The first category of such a kinetic microstructure engineering strategy uses the localized Mn bands inherited from Scheil-type solidification micro-segregation. These kinetically formed Mn composition patterns are a consequence of the gradually changing local and temporal tie-line conditions during liquid-to-solid interface migration. The detailed scales and the upper and lower bounds in Mn segregation that are accessible through this kinetic mechanism, depend on the diffusion rates of Mn and C in the solid and in the adjacent liquid, according to the Scheil model and on the solidification rate. For example, Lee et al. [113] have utilized Mn solidification segregation bands to tune the retained austenite distribution and the stability of these austenite regions in a hot-rolled MMnS. They found that the austenite evolved from Mn-rich and Mn-lean bands possessed different growth kinetics and compositions, thus leading to a spectrum of austenite mechanical stability and a correspondingly heterogeneous TRIP effect upon loading.

The second kinetically-motivated microstructure design approach utilizes chemical heterogeneities arising from different types of Mn enriched precursors formed during the upper stream processing steps, e.g. carbides [42,114,116,117], Mn-rich austenite [18,24,115,118,119] or Mn-rich deformation-induced martensite [120,121]. Such microstructure components and phases can serve as quasi reservoirs or vessel phases [21,115] for Mn (and sometimes C to some extent [21,115]). During the subsequent austenite reversion treatment, these element reservoirs (e.g. carbides and martensite) can be partially or completely dissolved, thus releasing Mn and C (and other) elements into the surrounding matrix. Depending on the diffusion range, such austenite-stabilizing elements can then be used as desirable tools to induce local heterogeneities. One such example was given by Sun et al. [42] using an initial pearlitic microstructure with Mn enriched cementite (Figure 7). By a fast austenitization at 770°C (above the Ae3) for 20 s, pearlitic cementite fully dissolved but the associated Mn modulation was mostly maintained. This resulted in an alternately arranged Mn-rich and Mn-lean austenite regions at the austenitization temperature, which enabled the formation of nano-lamellar of austenite (retained from the Mn-rich regions) and martensite (transformed from the Mn-lean regions) upon quenching. This was realized as an experimental demonstration of the austenite transformation regimes simulated by Enomoto et al. [122], where C diffusion-controlled interface migration could quickly dissolve cementite but maintain the Mn composition fluctuation. The underlying principle behind such microstructure architecturing method thus lies in the kinetic mismatch between sluggish Mn diffusion (especially within austenite) and rapid austenite formation [18,24,42,115].

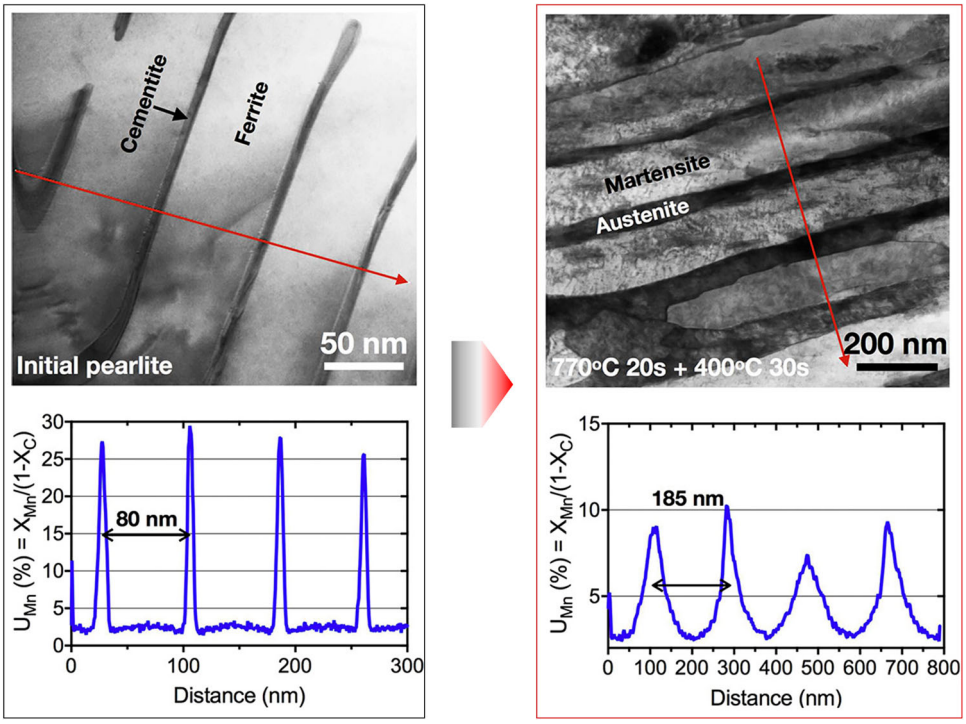

Figure 7. Scanning transmission electron microscopy (STEM) bright field images and energy-dispersive X-ray spectroscopy (EDX) line scans showing the transformation of an initially pearlite microstructure with Mn enriched cementite to a laminated microstructure consisting of alternately arranged martensite and austenite in a 0.5C-4.4Mn (in wt-%) steel subjected to re-austenitized at 770°C for 20 s followed by a tempering treatment at 400°C for 30 s. The figure is reconstructed with permission from Ref. [42].

In addition to solidification micro-segregation and kinetically produced Mn enriched precursors, the Mn heterogeneity in MMnS can also be produced using the different operative interfacial tie-lines that are available at different temperatures. For example, Wan et al. [123] proposed a two-step heat treatment for a 0.2C-7.8Mn-2Al (wt-%) steel, consisting of a first heating stage to 720°C followed by a direct cooling to 650°C and holding for 1 h. At the second annealing step, the gradual build-up of Mn at the ferrite-austenite phase boundaries along with interface migration resulted in a compositional core–shell austenite (with Mn-lean core and Mn-rich shell). The enveloped Mn-lean austenite core can gain additional thermal stability due to the suppression role of the Mn-rich shell on martensite nucleation upon quenching from 650°C.

In summary, besides the established thermodynamics means of material manipulation, we presented here an additional range of tools of heat treatments, different from conventional intercritical annealing, for the kinetics manipulation of chemical heterogeneity features in MMnS. The kinetic microstructure design target here is to achieve an optimized use of the solute Mn atoms, through enriching them to local regions which aids the formation of austenite with the optimum phase conditions towards better strain-hardening and damage tolerance [18,24,115,118,119]. The examples above have only listed a few thermomechanical processing options, showing how to kinetically exploit chemical heterogeneity for advanced microstructure design. More opportunities in this direction are still available and can be explored in the future with the help of an improved understanding of phase transformations in MMnS.

Deformation behaviour

Strain-hardening micromechanisms

Transformation-induced plasticity

A key feature of MMnS is the large fraction of austenite that can be designed in a way to be metastable and that is then accessible to transformation to martensite upon mechanical loading. Such deformation-driven transformation from a soft host phase (austenite) into a harder microstructure product (martensite) results in an extraordinarily high strain-hardening rate (exemplarily shown in Figure 8(a)), due to the high strength of the martensite and the volume expansion-induced dislocation accommodation processes [124]. It is this increased strain-hardening rate that leads to the better ductility of an alloy (due to the delay of Considère-type plastic instability or necking), a phenomenon known as the TRIP effect. This effect is particularly important for ultrafine grained materials like MMnS, as other dislocation accumulation-dependent strain-hardening mechanisms (e.g. forest dislocation hardening and dynamic Hall-Petch effect due to deformation twinning) are often suppressed when the grain size falls below ~1

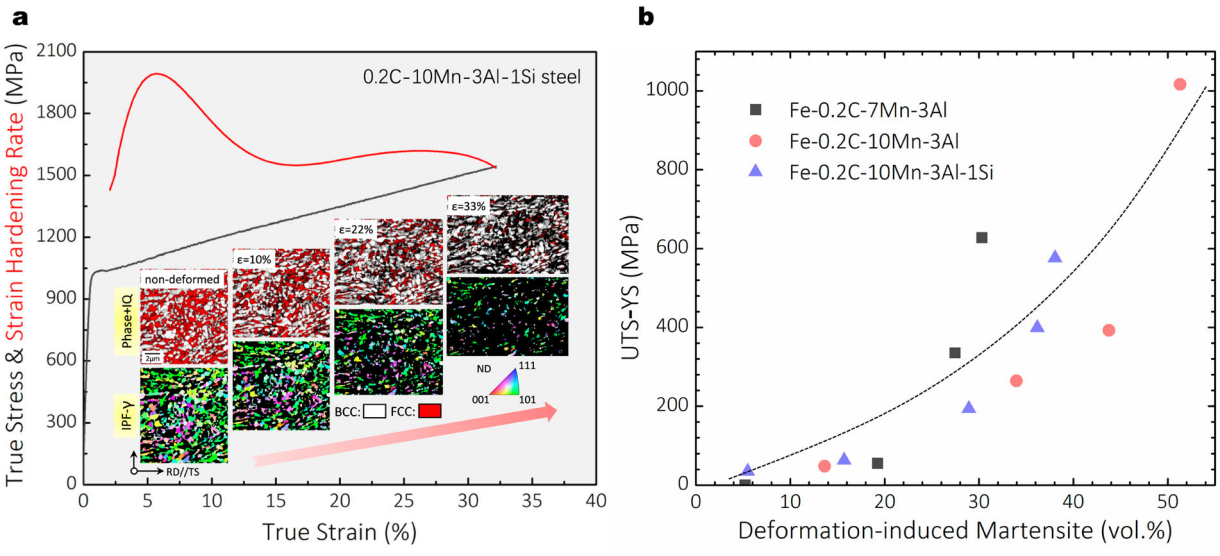

Figure 8. (a) True stress–strain curve, strain-hardening response and the evolution of microstructure upon deformation of an MMnS (0.2C-10Mn-3Al-1Si, in wt-%), intercritically annealed at 750°C for 5 min. The steel possesses an austenite-ferrite two-phase microstructure after heat treatment. The insets are the *ex-situ* EBSD phase plus image quality (IQ) map and austenite inverse pole figure probed at the same location, showing the progressive transformation of austenite to α′-martensite upon straining; (b) The dependence of strain-hardening capability (quantified here by the stress difference between yield strength, YS and ultimate tensile strength, UTS) on the amount of deformation-induced α′-martensite in MMnS. The figure contains the data of three MMnS grades (0.2C-7Mn-3Al, 0.2C-10Mn-3Al and 0.2C-7Mn-3Al, in wt-%), which were subjected to cold rolling and intercritical annealing at different temperatures. The volume fraction of deformation-induced martensite was calculated based on the austenite fraction before deformation and after deformation to the uniform strain level. Part of the data were published previous in Refs. [9,10].

μm [125–128]. This is revealed in Figure 8(b), which shows the strong dependence of the strain-hardening capability of MMnS on the amount of deformation-induced martensite.

The thermodynamics of deformation-induced martensite can be depicted based on the schematic diagram shown in Figure 9(a) [129]. For a temperature below T_0 where the chemical free energy of the austenite equals that of martensite, additional mechanical work (W) needs to be provided to achieve the critical transformation driving force ($\Delta G_{Ms}^{\gamma\rightarrow\alpha'}$, equals the transformation energy barrier contributed by elastic strain energy, E_{El}, interfacial energy, E_I, and frictional work related to the motion of the interface and the creation of defects during the transformation, E_f [130]). Stress-induced martensite is purely assisted by this mechanical work and has a similar nucleation behaviour as quench-induced martensite formed below the M_s temperature. Strain-induced martensite, on the other hand, is additionally aided by the creation of new highly-potent nucleation sites produced by the preceding plastic deformation [131]. The nucleation of strain-induced martensite in steels is generally believed to occur due to a double shear mechanism following the hard-sphere model initially proposed by Bogers and Burgers [132] and further developed by Olson and Cohen [131,133]. The model, as schematically shown in Figure 9(b) [134], suggests that α′-martensite nucleation can be accomplished by two shears of $\alpha_\gamma/18$ $[1\bar{2}\bar{1}]$ slip on each $(11\bar{1})_\gamma$ plane and $\alpha_\gamma/16$ $[\bar{1}2\bar{1}]$ slip on each $(111)_\gamma$ plane, occurring either successively or simultaneously [132–134]. These two shears correspond to one-third and three-eighths of the Burgers vector of a Shockley partial dislocation (or a twinning shear), respectively. Based on this model, Olson and Cohen proposed that α′-martensite is favourably nucleated at various intersections of deformation-induced hexagonal close-packed (HCP) ε-martensite, twins, stacking fault (SF) bundles or slip bands, where the two shearing conditions are more likely to be fulfilled [131]. Such martensite formation behaviour has been frequently observed and validated in metastable austenitic stainless and high-Mn steels [131,134–138], with one example shown in Figure 9(c) [136].

In MMnS, despite that a systematic study on the formation mechanisms of deformation-induced α′-martensite is still lacking, results from the literature [9,14,50,139] have suggested a similar nucleation mechanism as that proposed by Olson [131,133]. De Cooman et al. [14,139] have observed, in two MMnS grades (0.3C-10Mn-3Al-2Si and 0.3C-12Mn-3Al, in

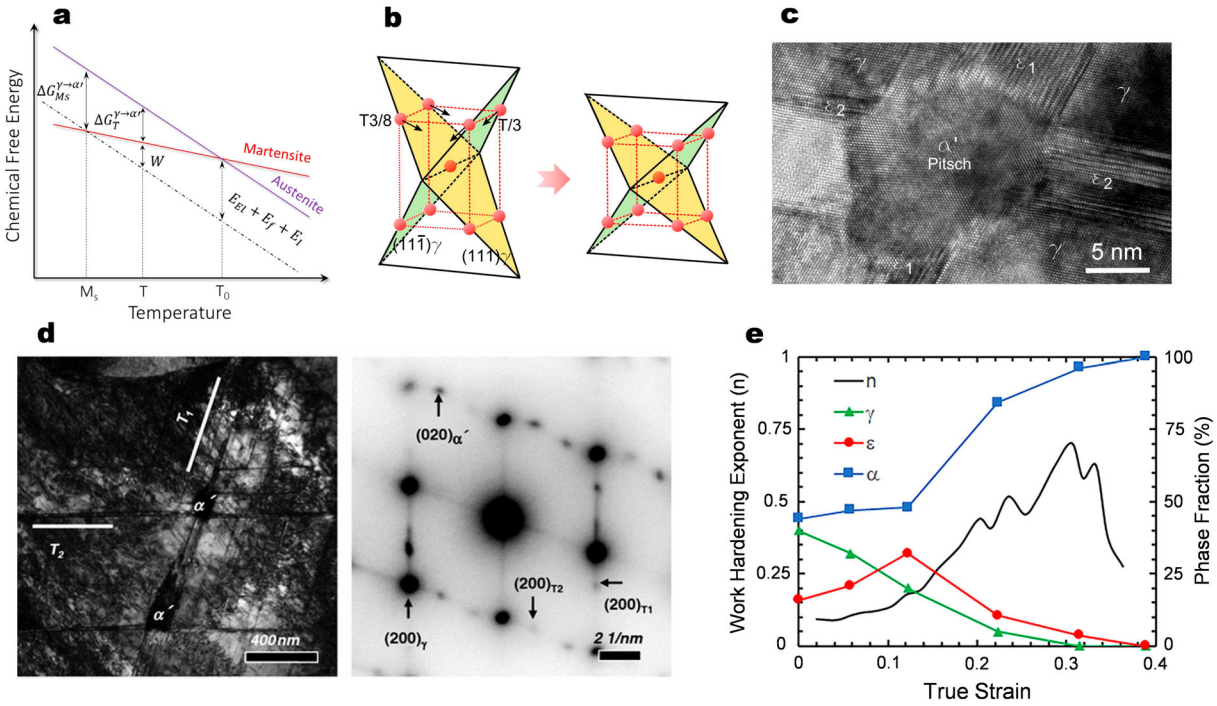

Figure 9. (a) Schematic illustration showing the chemical free energy change of austenite and martensite as a function of temperature [129]. (b) Schematic diagram of the Bogers and Burgers model for austenite-to-α′-martensite transformation [134]. The two shears of T/3 = $\alpha_\gamma/18$ < 112 > and 3 T/8 = $\alpha_\gamma/16$ < 112 > along $\{111\}_\gamma$ planes convert the face-centred cubic austenite into body-centred tetragonal martensite (T: twinning shear); (c) and (d) are typical examples showing α′-martensite nucleation at intersections of two shearing systems in metastable austenitic stainless steels [136] and intercritically annealed MMnS [14], respectively. (e) The influence of deformation-induced α′-martensite and ε-martensite on strain-hardening exponent (n) in an MMnS (0.2C-11Mn-2.1Si-1.5Al, in wt-%) [142]. The phase fraction in this study was measured by XRD. The maximum strain-hardening rate is only acquired when deformation-induced α′-martensite is formed. The figure is reconstructed with permission from Refs. [14,134,136,142].

wt-%), that α′-martensite was nucleated at intersections of deformation twins (Figure 9(d)), which was also observed by Sun et al. [9] in a 0.2C-10Mn-3Al-3Si (in wt-%) steel. This twinning-assisted α′-martensite nucleation was further confirmed by Nimaga et al. [140] who studied the martensite transformation in an MMnS (0.6C-9.5Mn, in wt-%) by micropillar compression. It was found in their study that the average critical stress for α′-martensite transformation in [100] oriented micropillars was much smaller than that in [110] micropillars (~483 MPa vs. ~700 MPa), due to the easier formation of twins in [100] oriented austenite grains upon compression [140]. In a separate work of Sun et al. [50], they conducted *in-situ* three-point bending tests combined with electron backscatter diffraction (EBSD) and electron channelling contrast imaging (ECCI) for a 0.2C-10Mn-3Al-1Si (in wt-%) steel and found that the SF interactions or SF-annealing twin interactions might also provide favourable nucleation sites for α′-martensite. This finding provides useful insights explaining the generally independent nature of α′-martensite formation on the occurrence of deformation twinning in MMnS.

However, the above-mentioned nucleation of α′-martensite in MMnS was questioned by Yen et al. [141] who investigated the deformation behaviour of a 0.08C-10.6Mn-V-Mo steel with an austenite-ferrite microstructure. They observed that the deformed structure of austenite contained only one shear system in the forms of single-variant lamellar SFs, deformation twins or ε-martensite. They attributed this to the fine grain size in their materials (average size ~300 nm). It was thus concluded that the α′-martensite transformation that had occurred in the plastic deformation regime was purely induced by local stress concentration at interfaces which provided sufficient transformation driving force, i.e. it was interpreted as an essentially stress-induced transformation mechanism. However, studies in stainless steels have found that even when the martensite nucleation is sometimes observed to occur at single shear system such as single ε-martensite lath or twin, the double shear model seems still valid when characterized in atomic scale [134,135]. Yang et al. [134] proposed that under such circumstance, the two shears can be satisfied by the transformation-induced lattice rotation and the associated continuous lattice elastic deformation at the diffuse ε/α′ interface.

In addition to α′-martensite formation, another form of martensite, ε-martensite, has also sometimes been observed in MMnS upon deformation [141,143,144], which is not surprising as the austenite's SFE in such steels is generally low enough (a few tens of mJ m^{-2} [9]) to trigger extensive dislocation dissociation into Shockley partials and the formation of stacking faults. The slip of such partial dislocation on every second $\{111\}_\gamma$ plane produces a bulk ε-martensite crystal with an HCP structure [133,136]. However, the amount of deformation-induced ε-martensite is often reported to be much lower than that of α′-martensite (typically only a few volume percent [144]). Also, there seems sufficient evidence showing that ε-martensite only behaves as an intermediate phase upon room temperature deformation and will eventually transform to α′-martensite at higher deformation levels [141–143], although whether the nucleation occurs at the intersections of ε-martensite laths or within single ε-martensite lath is not yet clear [141,143]. These factors make deformation-induced ε-martensite formation only as a weak strain-hardening contributor compared with α′-martensite, as shown in Figure 9(e) [142].

The extent of the TRIP effect is normally characterized by the change in the amount of martensite as a function of plastic strain, i.e. the kinetics of deformation-induced martensite. In MMnS, this can be affected by many microstructural and mechanical factors including composition, grain size, morphology, defect density, orientation and local deformation state (stress triaxiality, stress, strain and strain rate). The influence of many of these factors (e.g. grain size, morphology and defect density) on the austenite's mechanical stability is complex and controversial, partly due to the difficulty of deconvoluting one single factor from other influencing factors, particularly in multiphase steels with sometimes also heterogeneous chemical composition as outlined above. Since these points have already been overviewed in the recent literature [145,146], we do not attempt to cover all the influencing factors here and will only discuss some of them in Section 7, when discussion mechanical property-directed microstructural design approaches and the associated mechanical mechanisms.

Twinning-induced plasticity

The TWIP effect was originally targeted as the main deformation mechanisms for high-Mn austenitic steels (with typical composition ranges of 0-1% C, 15-30% Mn, 0-3% Al and 0-3% Si, in wt-% [63]) which exhibit a large amount of deformation-induced twins (typically 10~20 vol.-% [63]) and a progressively high strain-hardening rate. The main reason of the twin-induced enhancement of the strain-hardening lies in the influence of the gradually evolving deformation twin patterns on the dislocations. Two primary effects were identified to be relevant in that context: (a) The so-called 'dynamical Hall-Petch effect'. This refers to the gradually increasing number density of deformation-induced twins, the small spacing among which progressively reduces the effective mean free path of the dislocations, thus promoting dislocation storage and enhancing isotropic strain hardening [147,148]; (b) The back-stress effect (kinematic hardening), arising from dislocation pile-ups at twin

boundaries [149]. More details about these two effects have been reviewed elsewhere [63,150]. The frequently observed formation of deformation twins in MMnS gives rise to the argument that the TWIP effect is activated in such steels and serves as one important contributor to the strain-hardening ability [14,151–154]. Indeed, the austenite composition in MMnS can normally be adjusted by intercritical annealing and the associated solute partitioning to have an suited value of the intrinsic SFE (typically in the range of 15~45 mJ m^{-2}) that is required to trigger deformation twinning [9,14,18,24,63,154]. In most studies, only one twinning system is activated in single austenite grains in MMnS with a small twin spacing and twin thickness of typically a few tens of nanometres (as shown in Figure 10(a)) [9,24,153,154]. These twinning features are probably associated with the usually ultrafine grain scale in these steels. It has been documented in some high-Mn TWIP steels, that grain refinement tended to restrict the activated twinning systems and increased the number density (not the volume fraction) of deformation twins [155,156]. This was proposed to be due to a higher number of twin nucleation sites at grain boundaries in fine grained samples associated with the more homogenous dislocation distribution evolved prior to twin formation [156]. There are also some studies showing that a smaller grain size increases the critical twinning stress [126,157], which can strongly suppress the occurrence of mechanical twinning in austenite [128]. However, this factor might not necessarily influence the activation of deformation twinning in MMnS, as the yield strength in such steels can also achieve a high level (near or above 1 GPa) owing to the fine grain size and the multiphase composite effect.

Despite sufficient evidence of the TWIP effect in MMnS, its actual contribution to strain-hardening enhancement in such steels seems to be quite minor compared with other effects like the TRIP mechanism. Lee and De Cooman [14] have studied the tensile behaviour of a typical ultrafine grained two-phase MMnS using a constitutive model approach. The microstructure and the evolution of α′-martensite and deformation twinning upon straining are shown in Figure 10(b, c), respectively. It was found that the TWIP effect only slightly increases the steel's strain-

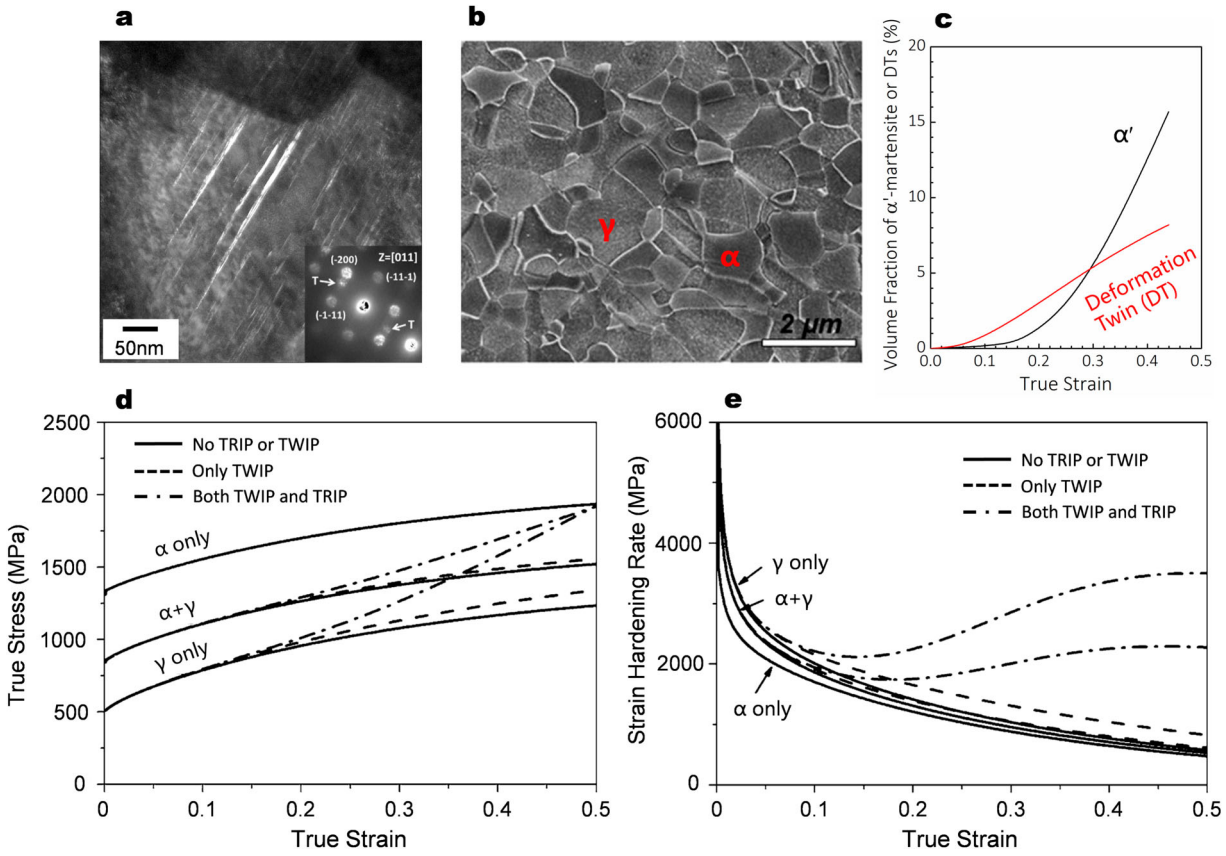

Figure 10. (a) Transmission electron microscopy (TEM) dark-field image with nano-beam diffraction pattern of an austenite grain in a 0.2C-10Mn-3Al-3Si (in wt-%) steel subjected to intercritical annealing at 750°C and subsequent tensile true strain of 15% [9], showing a typical behaviour of deformation twinning in MMnS; (b) Microstructure and (c) evolution of α′-martensite and deformation twinning upon straining in a 0.3C-10Mn-3Al-2Si (in wt-%) steel cold-rolled and intercritically annealed at 800°C (the curve of α′-martensite was fitted based on experimental data and the data of deformation twins were based on calculations; data of (c) was reconstructed from Ref. [14]); (d) simulated tensile curve and (e) strain-hardening response based on the microstructural information in (b) and (c) (the tensile behaviour of individual phase is also included) [14]. The figure is reconstructed with permission from Refs. [9,14].

hardening response and the strain-hardening curve only rises when the TRIP effect is activated (Figure 10(d, e)). Another evidence supporting this point comes from the experimental study of Sun et al. [9], who have carefully compared different MMnS samples with different degrees of TRIP and TWIP. As shown in Figure 11, Sample 1 is a reference steel with a weak effect of TRIP (inset in Figure 11(a)) and TWIP (only a few deformation twins in a few of austenite grains, as shown in the inset of Figure 11(b)). Sample 3 possesses a similar behaviour of TRIP [9] but a much stronger TWIP effect with a small twin spacing (<15 nm, i.e. higher twin density) and the activation of a secondary twinning system (inset in Figure 11 (b)). The density and fraction of deformation twins in this sample seem to be comparable to typical TWIP steels with an ultrafine grain size, although full quantitative data were not provided [155,157]. However, the comparison between Sample 1 and Sample 3 reveals only a slight enhancement in strain hardening caused by the stronger TWIP effect (Figure 11(b)), an overall effect which is much smaller than that which can be achieved by a more pronounced TRIP effect (see Sample 2, Figure 11(a, b)).

Dynamic strain aging

Dynamic strain aging (DSA) corresponds to a dynamic locking-unlocking process between mobile dislocations and diffusing solute atoms. Upon deformation, gliding dislocations can be temporarily arrested by obstacles (e.g. forest dislocations, precipitates and interfaces). During the waiting time the solutes (often interstitial atoms such as C or N) can decorate dislocations and lock them in-position until a higher stress is applied to unlock these arrested dislocations, providing a strengthening effect [158]. This is a longstanding viewpoint accounting for the PLC effect, a typical plastic instability phenomenon in alloys which is characterized by serrated plastic flow in the tensile stress–strain curves, the formation of spatio-temporal organized deformation bands and a negative strain rate sensitivity (NSRS). One example demonstrating the occurrence of such effect in MMnS at room temperature is shown in Figure 12.

Despite the distinct role of PLC in enhancing the materials' strain-hardening capacity, the underlying mechanisms for its occurrence is highly elusive in MMnS [49,159–161]. The first question is pertaining to whether this phenomenon is due to a specific behaviour of one single phase or a combined effect from many microstructural factors. The occurrence of this phenomenon in high-Mn steels and other austenitic steels, rather than in ferritic steels at room temperature, fuels the assumption that it is the austenite phase that constitutes the major contribution here. It should be noted that the PLC effect in high-Mn austenitic steels is difficult to be explained by the classical DSA model mentioned above, because the bulk diffusivity of C in austenite at room temperature is too low to arrest dislocations during the limited waiting time. Hence, several modified DSA models have been proposed for high-Mn steels. Rose and Glover [162] suggested that the dynamic locking of dislocations in austenite can be caused by the formation

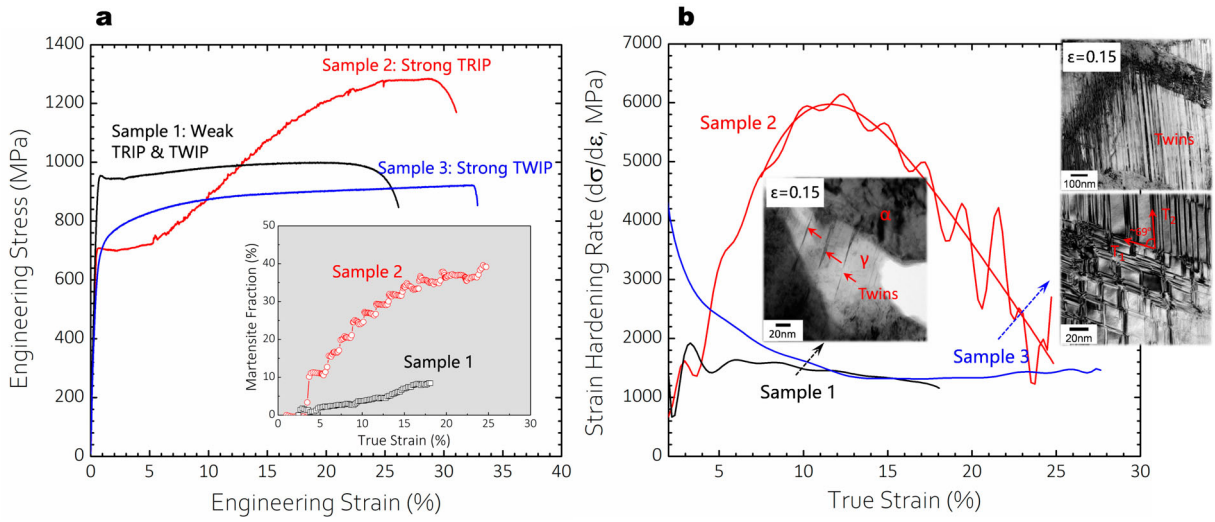

Figure 11. (a) Engineering stress–strain curves and (b) strain-hardening response of different MMnS samples tailored with different degrees of TRIP and TWIP. Sample 1: 0.2C-10Mn-3Al (in wt-%) steel intercritically annealed at 700°C for 5 min; Sample 2: 0.2C-10Mn-3Al-1Si (in wt-%) steel intercritically annealed at 800°C for 5 min. Sample 3: 0.2C-10Mn-3Al-3Si (in wt-%) steel intercritically annealed at 850°C for 5 min. All the samples have an austenite-ferrite microstructure. Samples 1 and 3 possess a similar austenite volume fraction (~30%) with a similar austenite mechanical stability (i.e. similar TRIP), and Sample 2 has a higher austenite fraction (~45%) and a lower austenite stability. The inset in (a) is the change of deformation-induced α′-martensite of Sample 1 and 2, and the inset in (b) is the deformation twinning behaviour of Sample 1 and 3 at a true strain of 0.15. The figure is reconstructed with permission from Ref. [9].

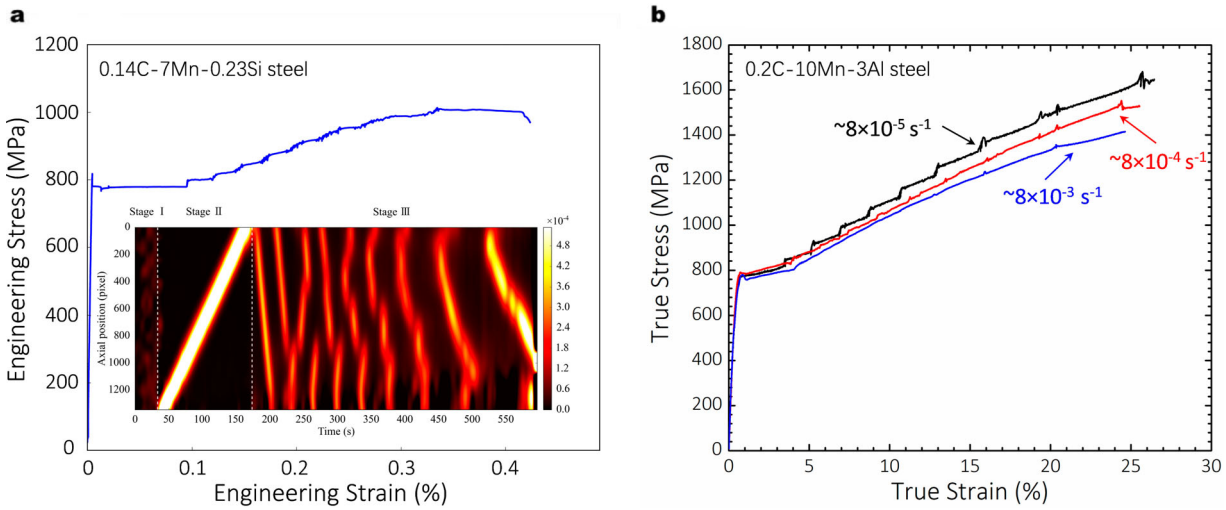

Figure 12. (a) Tensile curve and PLC banding behaviour of a 0.14C-7Mn-0.23Si (in wt-%) steel containing an ultrafine grained austenite-ferrite microstructure. The propagation of PLC bands is shown from the local strain rate map as a function of deformation time, quantified via the DIC technique. The marked Stages I, II and III correspond to the elastic deformation regime, Lüders banding regime and PLC banding regime, respectively. (b) Tensile curves of a 0.2C-10Mn-3Al (in wt-%) with a similar structure tested at different strain rates, showing a negative strain rate sensitivity [31]. The figure is reconstructed with permission from Refs. [31,48].

and rotation of a C-vacancy pair due to a Snoek-type mechanism. They further proposed that such rotation was more likely due to the short-range diffusion of vacancy rather than C, due to the relatively lower diffusion activation energy of vacancies in austenite. Lee et al. [163] attributed the DSA in high-Mn austenitic steels to the interaction between point defect C-Mn complexes ($CFe_{6-x}Mn_x$) and stacking faults. They proposed that the glide of a leading partial would transform a C atom in the stacking fault plane from the initial octahedral site to a tetrahedral site. Since the tetrahedral site is energetically unfavourable, the attraction between C and Mn atoms could allow the displaced C to be easily redistribute to a nearby octahedral site inside the stacking fault. Such relocation of C atoms was suggested to suppress the motion of the trailing partial thus resulting in strengthening (i.e. the strain aging effect). This process only requires a single diffusive jump of C atoms (i.e. no long-range diffusion is required), which might be fast enough to occur before the stacking fault is removed by the trailing partial. These two DSA models proposed for austenitic steels, however, have recently been questioned by Oh et al. [164] who proposed that DSA in high-Mn steels could be a result of pipe diffusion of C atoms. This conclusion was drawn based on their APT results and the determination of activation energies for the onset of PLC, for the pipe diffusion of C and for the reorientation of C in C-Mn complexes, where they found that the former two values were quite comparable. Similarly, the same research group also studied a TRIP-aided MMnS (0.15C-5.2Mn-0.4Si-0.004N, in wt-%) containing a mixture of austenite, ferrite and tempered martensite, in which the pipe diffusion of C atoms within austenite and the enabled rapid C-dislocation interactions were proposed as the key reason for the DSA phenomenon [159].

However, the aforementioned critical role of austenite in the occurrence of DSA/PLC in MMnS seems to be clouded by the fact that this phenomenon persists even after most of the austenite has mechanically transformed to α'-martensite. For example, Sun et al. [9] and Nam et al. [159] have shown in their MMnS, that the serrated plastic flow still occurs even with less than 10 vol.-% metastable austenite present in the microstructure. As the macroscopically measured tensile behaviour is a collective response of all the phases and the underlying phase-specific defect evolution, it is hard to believe that such a small amount of austenite can result in pronounced stress serrations (up to a few tens of MPa) and macroscopic PLC banding. Sun et al. [10,49] have noted that the room temperature PLC effect in MMnS only occurs in a certain range of austenite mechanical stability, i.e. when deformation-induced martensite occurs with a certain kinetics. They further hypothesized a possible trapping effect of small martensite embryos on mobile dislocations and such trapping effect might be maximized when martensite is continuously nucleated but not growing too fast [49]. A similar idea with a more detailed mechanistic picture was also recently proposed by Mola et al. [165] for a medium-Mn TRIP-aided stainless steel at a deformation temperature below 200°C. It was suggested that the α'-martensite formed within the operating slip bands locally blocked mobile dislocations and at the same time, transformed C atoms to a more mobile and super-saturated state

which could make them rapidly move to the martensite-austenite interface. Such C segregation can pin the dislocation sources at the hetero-interfaces thus increasing the critical stress needed to emit new dislocations. The pinning effect of C atoms on interfacial dislocation sources has actually been observed in an almost simultaneously reported work from Ma and Sun [23], which can serve as an important support to this TRIP-aided DSA model.

Multiphase composite effects

MMnS generally possess a multiphase microstructure consisting of austenite, ferrite and/or other accessible microstructure constituents in steels (e.g. martensite, bainite, pearlite, carbides, etc.). The mixture of these phases and/or microstructure features, which often have a high mechanical contrast relative to each other, produces a composite-like effect, which can also contribute substantially to the steels' strain-hardening ability. The steel type which can best showcase the importance of such effects is the ferrite-martensite dual-phase (DP) steel which shows a high strain-hardening rate at the initial plastic deformation stage [166]. One important contribution to this high initial strain-hardening is derived from the high density of geometrically necessary dislocations (GNDs) formed due to the plastic mismatch between the two phases and the resulting forest (isotropic) and long-range back-stress (kinematic) hardening [167–170]. The same strain-hardening mechanism also applies in MMnS, although its contribution has only been acknowledged by a few studies [9,171]. He and Huang [171] reported an MMnS (0.47C-10Mn-2Al-0.7 V, wt-%) which was tailored to be devoid of any occurrence of the TRIP, TWIP and DSA effects. They showed that this steel still possessed a good strain-hardening ability and thus a good uniform elongation (14%) at an ultrahigh yield strength level of 1.2 GPa. They attributed the observed high strain hardening to the composite hardening effect of the heterogeneous microstructure (a mixture of ferrite and stable austenite with different grain morphology).

In DP steels, the composite hardening effect is typically highest at the initial deformation regime, which is due to the initially very high mechanical contrast between ferrite and martensite and the initial rapid increase of GNDs [166,170]. The stored rate of GNDs would decrease when martensite starts to be plastically deformed, i.e. the level of strain incompatibility is reduced [168,169]. In contrast for MMnS, the strain incompatibility can be gradually increased with the progressive deformation-induced formation of fresh α′-martensite. This might lead to a more persistent increase in GNDs, promoting dislocation multiplication and local dislocation pile-ups even at relatively high strain regimes. Figure 13(a) demonstrates the EBSD results of an austenite-ferrite two-phase MMnS (0.2C-10Mn-3Al-1Si, in wt-%) in its undeformed and 20% strained states, showing a high local misorientation value (i.e. a high amount of GNDs) at the α-α′ and α′-γ interfaces after deformation. On the other hand, the generally ultrafine grain size in MMnS yields a very large area of phase boundaries, which can, in principle, provide a larger number of GNDs, thus give rise to a more pronounced strain hardening compared with DP steels with

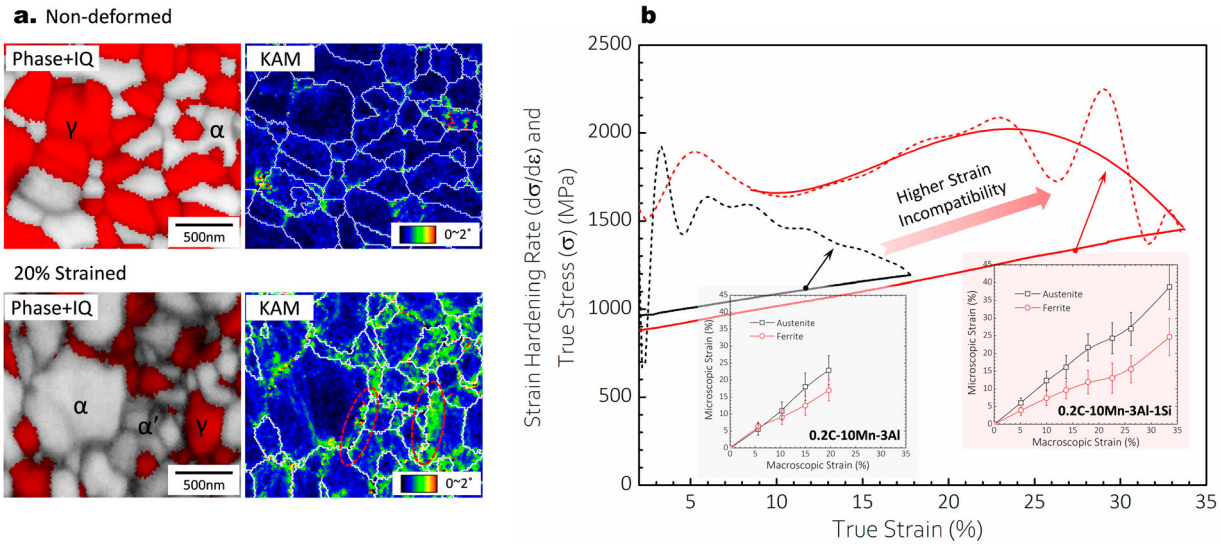

Figure 13. (a) EBSD phase plus image quality (IQ) map and kernel average misorientation (KAM) map of an intercritically annealed MMnS (0.2C-10Mn-3Al-1Si, in wt-%) before and after tensile deformation at 20% strain, showing a higher amount of GNDs (indicated by the higher misorientation values) at the phase boundary regions associated with the plastic mismatch among different phases (reconstructed with permission from Ref. [173]). (b) Comparison of the flow curve and the strain-hardening response between two ultrafine grained two-phase MMnS with a similar TRIP and TWIP effect but a different level of strain partitioning (or strain incompatibility, reconstructed with permission from Ref. [9]).

typically a coarser grain scale (often a few micrometers) [169,172]. Indeed, Sun et al. [9] have compared two MMnS samples which have a very similar microstructure and similar degrees of TRIP and TWIP. The only difference lies in the levels of strain partitioning between ferrite and the austenite-α′-martensite mixed phase, which is affected by the Si alloying and its resulting different solution strengthening effects for austenite and ferrite. They found that the sample, with a higher strain incompatibility upon deformation, possessed a higher strain hardening at the later deformation stages (Figure 13(b)) which is responsible for an almost doubled uniform elongation. It was further noted that the enhancement due to this multiphase composition effect is even higher than that caused by a more active TWIP effect inside the austenite phase (see Sample 3 in Figure 11(b)).

Strain/stress partitioning and localization

In MMnS, the individual phases and microstructure ingredients (e.g. ferrite, austenite and martensite) have different intrinsic properties, such as elastic modulus, strength and strain-hardening. These differences lead to their different mechanical response when exposed to mechanical stimuli, resulting in complex stress/strain redistribution patterns among them. This microscopic strain/stress partitioning behaviour plays a salient role in the overall mechanical behaviour of MMnS, including yielding [144], strain hardening [139,144,174] (discussed also in Section 4.1) and damage [175,176]. At the elastic deformation regime, it has been reported in ultrafine austenite-ferrite two-phase MMnS that both phases deform elastically, revealing a linear correlation between the elastic lattice strain (which can be measured by *in-situ* synchrotron X-ray or neutron diffraction experiments) and applied stress [23,50,144]. With an increase in applied stress, the soft phase plastically deforms first, marking the onset of the elastic-plastic transition stage at which stress partitions to the harder phase that still remains elastically deformed [23,50,144]. Both austenite [50,176–178] and ferrite [179,180] have been found as the softer phase in MMnS, depending on their respective phase constitution made up by their chemical composition, size, connectivity, texture and initial defect content.

During plastic deformation, the mechanical contrast among different phases leads to heterogeneous strain distribution that can be revealed by a variety of advanced characterization techniques. To give an example, Dutta et al. [174] have quantified the local

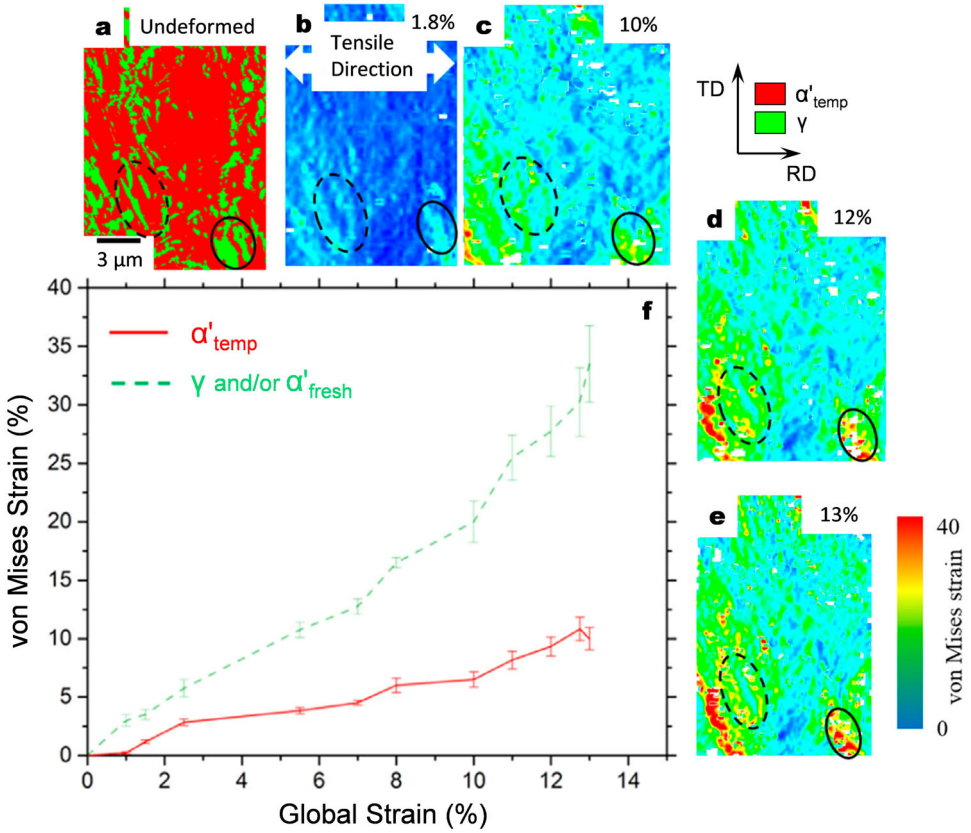

Figure 14. Strain partitioning between austenite (γ_R) and/or deformation-induced fresh martensite (α'_{fresh}) and tempered martensite (α'_{temp}) in a 0.05C-12Mn-3Al (wt-%) steel subjected to intercritical annealing at 555°C for 12 h. (a)–(e) EBSD phase map and the corresponding von Mises strain distribution maps at different global strains. (f) Quantitative measurement showing the evolution of the von Mises strains of the different phases as a function of the global strain. The figure is reconstructed with permission from Ref. [174].

von Mises strain distribution using the *in-situ* microscopic-digital image correlation (μ-DIC) technique in a 0.05C-12Mn-3Al (wt-%) steel consisting of austenite and tempered martensite. During deformation, the plastic strain was preferably accommodated by the softer austenite, e.g. about 20% strain was accommodated by austenite grains at a global strain of 10% (Figure 14). In contrast, only limited deformation (around 5% von Mises strain) was observed in tempered martensite at the same global strain. Therefore, austenite was rapidly strain hardened through TRIP, TWIP or dislocation planar glide. The rapid strain-hardening within austenite due to a high strain accommodation contributes to the overall strain hardening of the materials [9]. This might also lead to strain localization back to the ferritic phase when the flow stress of the hardened austenite exceeds that of its adjacent phase. The latter behaviour was numerically visualized by Latypov et al. [43] who modelled the flow behaviour of a 0.15C-6Mn-1.5Si-3Al (in wt-%) steel using an finite element approach.

Several microstructure features including grain size [139], grain morphology [12], crystallographic texture [174] and spatial alignment of phase islands relative to the loading direction [174] affect the behaviour of strain partitioning and localization in MMnS. This is especially true for those MMnS with a laminated grain morphology where the plastic flow of austenite lamellae was found to be strongly influenced by their spatial alignment and texture. Dutta et al. [174] have shown that when the austenite lamellae were aligned at an angle of 45° to the tensile direction, a maximum geometrical shear is expected and a high plastic strain was localized in these laminated grains. Moreover, the texture memory effect in laminated MMnS can lead to an identical crystallographic orientation of reverted austenite to the prior-austenite grains, resulting in a high degree of strain localization due to the co-deformation of these grains. In comparison, the crystallographic orientation of reverted austenite grains was more random in cold-rolled and intercritically annealed MMnS (as the texture memory effect is mitigated by cold deformation), thus a more homogenous strain distribution was developed upon plastic deformation [174].

Microscopic and macroscopic yielding behaviour

Austenite-ferrite two-phase MMnS, especially those with ultrafine and equiaxed grains, often show a discontinuous yielding phenomenon, which is characterized by a yield point drop followed by a stress plateau (also referred to as yield point elongation) in the tensile stress–strain curves and the formation of Lüders bands [12,181–184] (exemplarily shown in Figure 15 (a)). This yielding behaviour is not commonly observed in other composite-like multiphase materials. For the occurrence of discontinuous yielding, two essential conditions are required, namely, an initially low density of mobile dislocations and an avalanching-driven increase in the number of mobile dislocations (a rapid dislocation multiplication). Specifically, three mechanisms have been proposed [173], which are listed as follows. (a) The locking-unlocking mechanism based on Cottrell and Bilby's theory [185]. This is the most widely accepted mechanism that is often used to account for discontinuous yielding in C-containing ferritic steels. It describes a pinning/locking effect of segregating interstitial solutes (i.e. the Cottrell atmospheres) on grown-in dislocations, which requires a higher stress for them to escape the atmospheres. This unlocking process results in abrupt and rapid plastic flow avalanches,

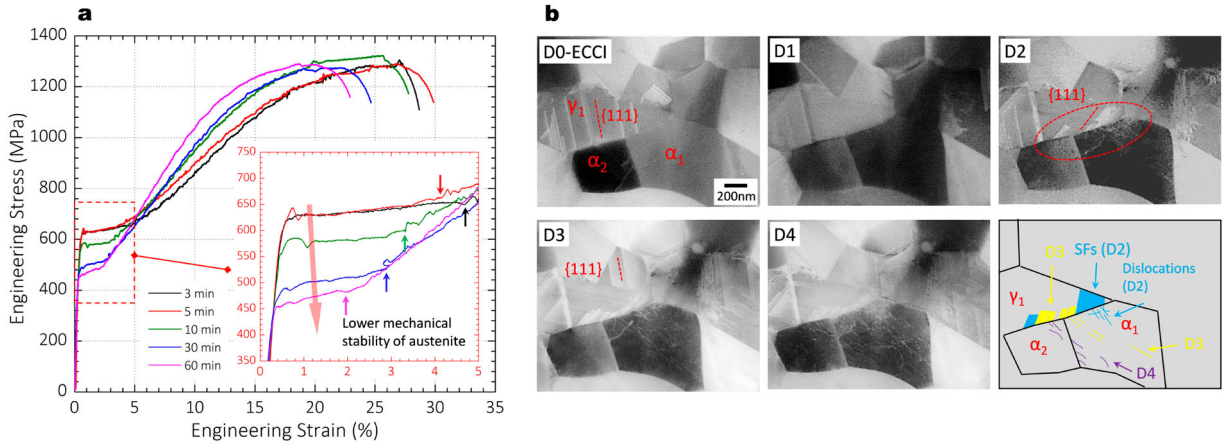

Figure 15. (a) Tensile stress-strain curves of a cold-rolled 0.2C-10.2Mn-2.8Al-1Si (in wt-%) steel intercritically annealed at 800°C for different times (from 3 min to 1 h) to yield different grain size and austenite mechanical stability. The data show the yield point elongation phenomenon and its variation with the austenite mechanical stability. (b) *In-situ* ECCI observation of the same steel (5 min annealed sample at 800°C) upon loading to different deformation stages (D0–D4) by three-point bending tests. The figure is reconstructed with permission from Ref. [50].

leading to a stress drop and the nucleation of Lüders bands; (b) The dislocation multiplication model proposed by Johnston and Gilman [186]. The mechanism suggests three promoting factors for discontinuous yielding: an initially low density of mobile dislocations, rapid dislocation multiplication upon loading and a relatively low sensitivity of dislocation velocity to applied stress. It further suggests that a portion of mobile dislocations can move even at the beginning of loading. An increasing stress enables a faster gliding and multiplication of these dislocations. The stress eventually ceases to increase (thus marking the upper yield point) when the plastic strain rate of the specimen that increases with the density and velocity of mobile dislocations equals the applied strain rate (crosshead speed divided by the gage length); (c) The ultrafine grain-induced discontinuous yielding mechanism that has been proposed in ultrafine grained materials (grain size below ~1 μm) such as pure Al, austenitic steels and interstitial-free (IF) steels [128,173,187]. This mechanism is associated with the high area fraction of the grain boundaries which act as both sinks for grown-in dislocations and sources for generating new dislocations. The former feature of grain boundaries reduces the number of mobile dislocations initially presented in the materials, and the latter contributes to plastic flow avalanches due to the large grain boundary areas (thus high-number of dislocation sources). Further, the dislocation nucleation process at grain boundary sources (e.g. ledges) needs to overcome an energy barrier [188], which means that the nucleation stress is higher than the stress needed for dislocation gliding. This factor also contributes to abrupt plastic flow avalanches [23,50].

Given that MMnS often contain ferrite as one of the major phases, the locking-unlocking mechanism has been proposed as the dominant reason for their discontinuous yielding in some earlier studies [12,143]. This point, however, encounters some difficulties, especially pertaining to the explanation of the following items:

- The discontinuous yielding also occurs in MMnS containing a high fraction of austenite (above 50%) where C atoms only interact weakly with dislocations (binding energy ~0.015 eV [189,190]) and tend not to form Cottrell atmospheres.
- In many cases, austenite is the softer phase and starts to deform first in the early micro-yielding stage [23,50,139]. The strength/hardness of individual phases and their mechanical contrast should be highly dependent on the specific composition, initial dislocation density and grain orientation. This means that before dislocation unlocking occurs from the hypothetical Cottrell atmospheres in ferrite, the early plastic deformation of austenite would already provide certain amounts of fresh mobile dislocations, a factor that is unfavourable for the occurrence of discontinuous yielding.
- Reports have shown that the value of yield drop in austenite-ferrite two-phase MMnS is relatively insensitive to the ferrite volume fraction [50]. This observation seems to be inconsistent with the locking-unlocking model which indicates that a higher ferrite fraction would lead to more dislocation unlocking events and thus contributes to a stronger yield drop [50].
- The commonly observed absence of discontinuous yielding in MMnS with a large fraction of coarse δ-ferrite is also difficult to rationalize within the locking-unlocking model.

These limitations have led to alternative explanations of the discontinuous yielding phenomenon in MMnS [23,50]. Particularly, it has been observed from *in-situ* characterization that the austenite-ferrite phase boundaries act as preferable dislocation nucleation sites for both austenite and ferrite in ultrafine grained MMnS (Figure 15(b)) [23,50]. This finding supports the ultrafine grain-induced discontinuous yielding mechanism, only that it is mainly phase boundaries (the commonly most prevalent type of planar defects in these steels) that emit dislocations rather than grain boundaries. Ma et al. [23] have further highlighted the vital role of the phase boundary chemistry in the dislocation emission process and thus in the extent of discontinuous yielding. More specific, they have found that the two-phase MMnS with C segregation at austenite-ferrite phase boundaries exhibited a more pronounced discontinuous yielding behaviour, which was explained by the effects of C segregation on enhancing the energy barrier for interface dislocation emission thus the stress difference between dislocation nucleation and gliding.

In addition to the interface characteristics (e.g. area fraction, structure and chemistry), other microstructural factors can also influence the yielding behaviour of austenite-ferrite two-phase MMnS. Documented factors include austenite mechanical stability [50,143,184], grain morphology [12,184] and initial dislocation density [143]. Particularly, the stability of austenite plays a salient role [50,143,191,192]. It is commonly observed that a reduced mechanical stability of austenite decreases the yield point elongation or the Lüders strain (Figure 16(a)) [10,50,184]. This is often attributed to the strain-induced martensite that formed within the Lüders bands and its effects on the band propagation. A higher amount of strain-induced martensite formation (reduced austenite stability) will provide a higher local strain hardening, which will increase the propagation speed of the Lüders bands for a fixed number of band fronts [50]. When the austenite mechanical stability is further reduced and stress-induced martensite formation

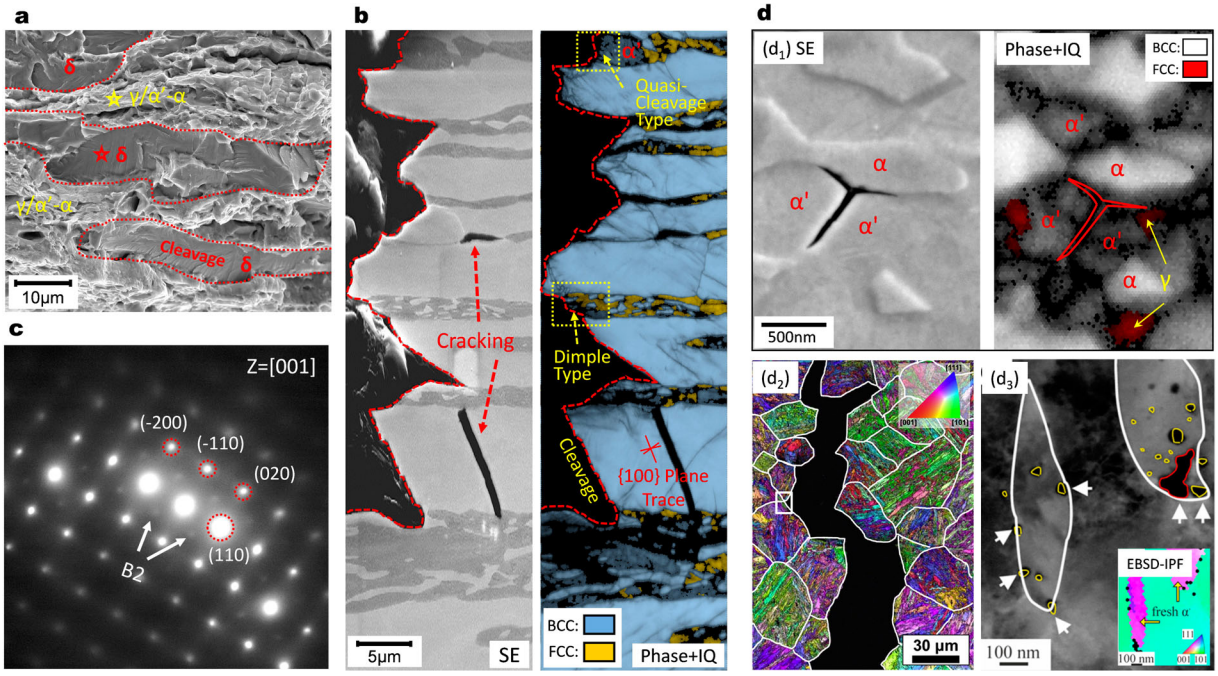

Figure 16. (a) Typical fracture surface and (b) cracking behaviour in a high-Al, high-Si added MMnS (0.2C-10Mn-3Al-3Si, wt-%) containing coarse grained δ-ferrite (the Al and Si contents in δ-ferrite are ~4 and ~3.5 wt-%, respectively). (c) Selected area diffraction (SAD) pattern of δ-ferrite in the same sample; (d) reported H-induced damage behaviour in MMnS: d_1, H-induced intergranular cracking along interfaces of ferrite and strain-induced α′-martensite and grain boundaries of parent austenite, observed in a 0.2C-10Mn-3Al-1Si (in wt-%) two-phase steel [197]; d_2, H-induced cracking along PAGB, observed in a hot rolled and annealed 0.1C-7Mn-0.5Si (in wt-%) steel containing laminated austenite-ferrite microstructure [202]; d_3, H-induced nano-void at ferrite-strain-induced α′-martensite interfaces and inside fresh martensite, observed in medium-Mn maraging steel (0.01C-9Mn-3Ni-1.4Al, in wt-%) [196]. The figure is reconstructed with permission from Refs. [31,196,197,202].

prevails, the nucleation behaviour of Lüders bands will also be influenced. Specifically, the stress-induced martensite formation, often occurred from the onset of loading, provides fresh mobile dislocations. This promoted plastic flow at the very early stages of deformation will suppress discontinuous yielding and can sometimes transfer the yielding behaviour to a continuous manner [10,50,143]. Some detailed studies on austenite-ferrite two-phase MMnS have interestingly observed multiple confined plastic zones formed in front of the Lüders bands [177,178]. These plastic zones are typically aligned with the macroscopic Lüders front and parallel in nature, with less deformed regions sandwiched between them. Varanasi et al. [177] further found that the size and distribution of these plastic zones were affected by the mechanical stability of austenite, which might be associated with the kinetics of deformation-induced martensite transformation and the resulting volume expansion.

Damage mechanisms

Deformation-driven damage nucleation and evolution

Unlike the strain-hardening behaviour, much less investigations have been carried out on the damage and fracture mechanisms in MMnS. This is partly due to the fact that this type of steels, in most microstructural states and under many testing conditions, show a ductile fracture behaviour that is governed by traditional mechanisms of micro-void nucleation, growth and coalescence [31,193–195]. In this fracture response pattern, nucleation of voids generally occurs at the various types of interfaces such as α-α′ [31,194], α-carbides [193], α′-α′ [193,194,196] and also at matrix-inclusion [194] interfaces. The underlying reason for this characteristic void nucleation pattern lies in the high stress concentrations at these interface regions, resulting from the elastic/plastic mismatch among different phases and the formation of dislocation pile-ups. The prevalence of specific void nucleation sites yet depends on the specific microstructure and the local mechanical states at the interfaces [193]. It should be noted that these interface boundaries, if not decorated with embrittling elements such as P and H, are not likely to be intrinsically brittle, as the propagation of nucleated damage features along these interfaces has not often been observed [31,193–195,197].

The fracture mode of MMnS can be changed when a large amount of Al and/or Si is added, for instance for lightweight design purposes. The additions of these two elements stabilize ferrite and can result in the formation of δ-ferrite within the microstructure, which, in some circumstances, can lead to a partially

brittle fracture behaviour [31,176,198]. Cleavage facets were often observed in the fracture surface of these high Al (or Si) added, δ-ferrite containing MMnS subjected to low-temperature or room temperature testing [31,198,199], as exemplarily shown in Figure 16 (a) [31]. Detailed studies have shown that these cleavage facets result from transgranular cracking along the {100} crystallographic planes of δ-ferrite (Figure 16(b)) [31,198]. It is known that both Al and Si promote the formation of ordering phases such as B2 and $D0_3$ inside ferrite [65,66], which has indeed been observed by Sun et al. [31] in a 0.2C-10Mn-3Al-3Si (in wt-%) steel (Figure 16(c)). Such long-range ordering effects can induce the formation of dissociated superlattice dislocations, which reduces the dislocation cross-slip frequency (which otherwise acts as a local stress-relaxation mechanism) and thus results in high stress concentrations and cracking along the cleavage plane. Another feature of these high Al, high Si added MMnS is their often layered microstructure with alternating δ-ferrite and austenite layers or layers of the austenite's respective decomposition products (e.g. ferrite and κ-carbides mixture, martensite, bainite or pearlite) [17,31,176,198,200,201]. The formation of such layered microstructures is due to the absence of the single phase austenite temperature region that makes hot rolling in the austenite-ferrite two-phase domain unavoidable [200]. Upon deformation, large plasticity mismatch is developed between the two layered components, a micromechanical state which promotes easy nucleation of damage events at the layers' interface and can even cause crack propagation along such interfaces at least over a certain distance [31,194,198].

MMnS is often embrittling when H is present, characterized by H-induced damage formation at the early deformation stages and the associated premature fracture initiation events. The behaviour of H-induced damage is complex in such steels, due to the following three factors.

(a) The large difference (more than two orders of magnitude) in H diffusivity and solubility between austenite and ferritic phases produces a complicated behaviour of internal H migration, trapping and distribution. This is substantially influenced by the change of the steels' microstructure, which can in turn alter the damage behaviour and the underlying embrittling mechanisms. Sun et al. [197] have demonstrated, in a ferrite-austenite two-phase MMnS, that the preferable damage nucleation site did not change when H was mainly trapped at lattice defects inside the ferrite phase. The degradation of ductility in this case was mainly due to the significantly increased void nucleation rate at the α-γ/α′ phase boundaries, promoted by the H-enhanced local plasticity (HELP) effect within ferrite and the resulting increased strain incompatibility between the soft ferrite and the adjacent harder γ-α′ mixed phase. However, when the volume fraction of austenite was increased such that a percolation threshold was reached, H trapping at ferrite-austenite phase boundaries and inside austenite became inevitable [197,203]. In this scenario, H-induced cracking along the α-γ/α′ interfaces and the prior-austenite grain boundaries (PAGB), promoted by the H-enhanced decohesion (HEDE) mechanism, was prevalent.

(b) A variety of phase constituents and (hetero-) interfaces typically exist in MMnS [31,142,173,194]. The different phases respond differently with H owing to their different crystal structures, substructures, defect densities and mechanical properties [204]. The different structures, chemistry and micromechanical states among the interfaces would also give rise to a different tendency for H trapping (or segregation) and for the associated reduction of their cohesive strength. The preferable crack nucleation and propagation sites would thus depend on the specific microstructure, local/global H amount and mechanical boundary conditions. It is thus not surprising that different formation sites of H-induced damage have been reported in the previous literature focusing on different microstructure and H-charging scenarios (as shown in Figure 16(d)) [196,197,202,204].

(c) The austenite-to-martensite transformation occurring in MMnS during deformation resets the local structure and micromechanical state in terms of strain/stress partitioning and localization, as well as the local thermodynamic driving force and kinetics of H migration. This means that the transformation kinetics and the timing of H ingress (e.g. before or after phase transformation) are also important factors influencing the behaviour of H-induced damages and the associated mechanisms [24].

Effect of deformation-induced martensite

Deformation-induced α′-martensite occurring in steels affects damage formation in two different ways. On one hand, the austenite-to-martensite (α′ type) transformation itself results in volume expansion (typically 3~4% at room temperature [205]) which produces a compressive stress field around the nucleated voids/cracks, suppressing their growth [31,206,207]. The transformation also dissipates mechanical work that would otherwise be available

for damage evolution [208]. A recent study on the fatigue crack growth in MMnS also suggests that the freshly formed α′-martensite can act as strong mechanical barrier blocking the advancing crack growth [209]. This arresting effect of the fatigue crack is due to the hardness of martensite as a transformation product, rather than to the actual transformation process itself [209]. On the other hand, the deformation-induced α′-martensite phase is a less tough phase compared with ferrite or austenite, especially when it has a high C content [210]. It has been shown in as-quenched martensitic steels that a brittle fracture behaviour occurs when the C concentration exceeds 0.3 wt-% [210]. This critical value can be easily reached in the parent austenite phase that is normally C enriched after intercritical annealing. Therefore, martensite cracking can occur when the deformation it needs to carry exceeds its failure tolerance (deformation at failure) [209]. Such cracking behaviour has indeed been observed by Steineder et al. [193] in a 0.1C-6Mn (in wt-%) steel where a significant amount (more than 50% by volume) fresh α′-martensite had been formed prior to fracture. The formation of martensite also locally increases the plastic mismatch among the phase constituents which promotes damage formation at the related hetero-interfaces [31].

The above-mentioned two antagonistic effects of deformation-induced martensite on damage can be better understood in a simple schematic diagram, shown in Figure 17, considering three hypothetical MMnS with different austenite mechanical stability levels, subjected to tensile deformation. Comparing Sample 1 and 2, Sample 2 with a lower austenite

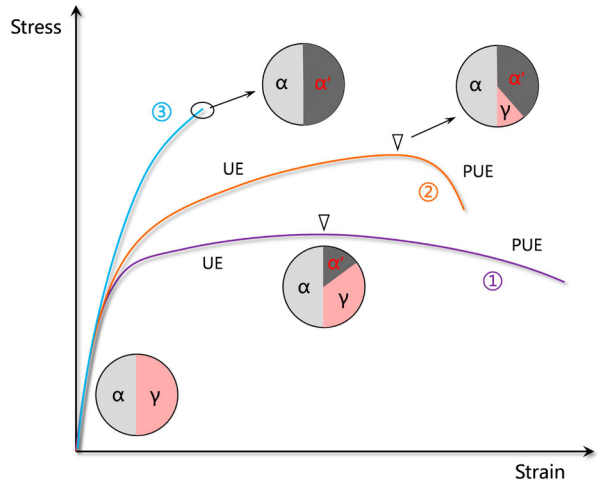

Figure 17. Schematic diagram showing the effects of deformation-induced martensite on the tensile behaviour in three hypothetical MMnS with initially a ferrite-austenite two-phase steel and different austenite mechanical stabilities (the strain point corresponding to the uniform elongation is marked by a triangle for Samples 1 and 2, UE: uniform elongation, PUE: post-uniform elongation).

stability essentially forms a higher amount of martensite at the strain corresponding to the material's global uniform elongation. The existence of the larger fraction of fresh martensite in Sample 2 can promote damage formation either inside martensite or at martensite-related interfaces during the necking regime, resulting in a smaller post-uniform elongation. This stronger TRIP effect, despite providing a higher strain-hardening ability before necking, also leaves behind less remaining austenite that can be further continuously consumed to constrain damage growth and suppress shear instability during the necking stage. For the case of a steel with an extremely unstable austenite state (Sample 3 in Figure 17), the austenite will completely transform to martensite already at a small plastic deformation (or even within the macroscopic elastic deformation regime). In this case, the failure tolerance of martensite can be rapidly achieved which can lead to premature failure of the specimen. The discussion clearly shows that, in addition to the contribution of TRIP to strain-hardening and uniform elongation, the remaining austenite available for further deformation in the localized deformation (e.g. necking) regime and the associated effect of deformation-induced martensite transformation on damage evolution must be considered when designing ductile and formable MMnS. In other words, it is important to keep in mind not only the thermodynamic stability of the austenite phase against martensite formation when designing such a steel, but more importantly, the sequential versus instantaneous transformation of the metastable austenite into martensite must be considered, where the former is usually preferable over the latter [211].

Unlike the partially beneficial role of deformation-induced martensite transformation on damage tolerance under H-free condition, the TRIP effect is commonly detrimental for the steels' H resistance, due to two factors. First, the formation of deformation-induced martensite raises the local stress which increases the driving force for crack formation and, at the same time, favours stress-driven H migration. The diffusion and accumulation of H inside the microstructure to regions of high local hydrostatic tensile stress are considered as one important reason for H embrittlement [71,212], regardless of the prevalent mechanisms. Second, the TRIP effect transforms the H atoms from their initial low-mobility solute state in the host phase (austenite) to a super-saturated and highly mobile state inside the product phase (here α′-martensite) [24,212,213]. The following rapid interaction between the super-saturated H and various types of defects (e.g. vacancies, dislocations, interfaces and free surfaces) then promotes damage nucleation and propagation. Obviously, the second factor only plays a role when the H is initially trapped inside the austenite phase. Sun et al. [24] have shown in a

ferrite-austenite two-phase 0.2C-10Mn-3Al-1Si (wt-%) steel that the fracture mode and the associated embrittling mechanism can be significantly changed depending on when the H ingress occurs. More specific they found a transition from an intergranular plus quasi-cleavage fracture mode for pre-charged specimens to a nanoscaled 'mottled', nano-dimple liked fracture surface when H was mainly introduced after most of the austenite had already been transformed to α′-martensite.

The mutually exclusive nature between the TRIP effect on the one hand and H embrittlement resistance on the other concerns for the application of MMnS in safety critical parts, especially in H-containing harsh environments. Fortunately, the large scope of microstructure tuning in such materials provides ample opportunities to circumvent critical micro-damage scenarios. For example, as reviewed in Section 3.3, a tailored heterogeneous Mn distribution with locally confined Mn-rich zones can be readily produced in MMnS (and also many other Mn-containing steels) upon thermodynamics-aided design of the corresponding heat treatments [18,21,24,42]. These Mn-rich regions locally stabilize austenite against martensite transformation, thus turning them into plastically compliant buffer zones that can arrest H-induced cracks intruding from other regions. This idea has been shown to be effective in enhancing the overall H-resistance of steels without sacrificing their strain-hardening capacity and strength-ductility combination in H-free condition [24].

Effect of solute segregation

In addition to H, segregation of other elements to interfaces can also influence the interface cohesive strength and thus the damage behaviour at these regions. It was reported that some elements (e.g. Groups IVA to VIA in the Periodic Table including P, S, Sb, Sn, As, Si, etc.) are detrimental in that respect while others (e.g. B and C) are even beneficial [214–216]. The segregation of Mn to grain boundaries has been found to be the cause of embrittlement in some MMnS [40,217]. Kuzmina et al. [217] reported a change in impact toughness of a model Fe-9Mn (wt-%) alloy as a function of annealing time at two annealing temperatures (450 and 600°C), as shown in Figure 18. When the annealing time was short (e.g. 10 s at 450°C), Mn segregated at the PAGB and substantially reduced the room temperature impact toughness. With longer annealing time (e.g. after 672 h at 450°C or 3 min at 600°C), reversion from α'-martensite to austenite occurred at grain boundaries which drastically reduced the grain boundary segregation of Mn, hence increasing the material's impact toughness (Figure 18).

Traditional explanations on the embrittlement caused by Mn segregation were proposed to be either due to the co-segregation of Mn along with other harmful impurities (e.g. P) [218,219], or a direct effect of Mn segregation on lowering the grain boundary cohesion [216,217,220], or a mixture of both effects. The co-segregation of Mn and P has indeed been observed in a hot rolled and annealed 0.1C-7Mn-0.5Si (in wt-%) steel by Han et al. [40] who

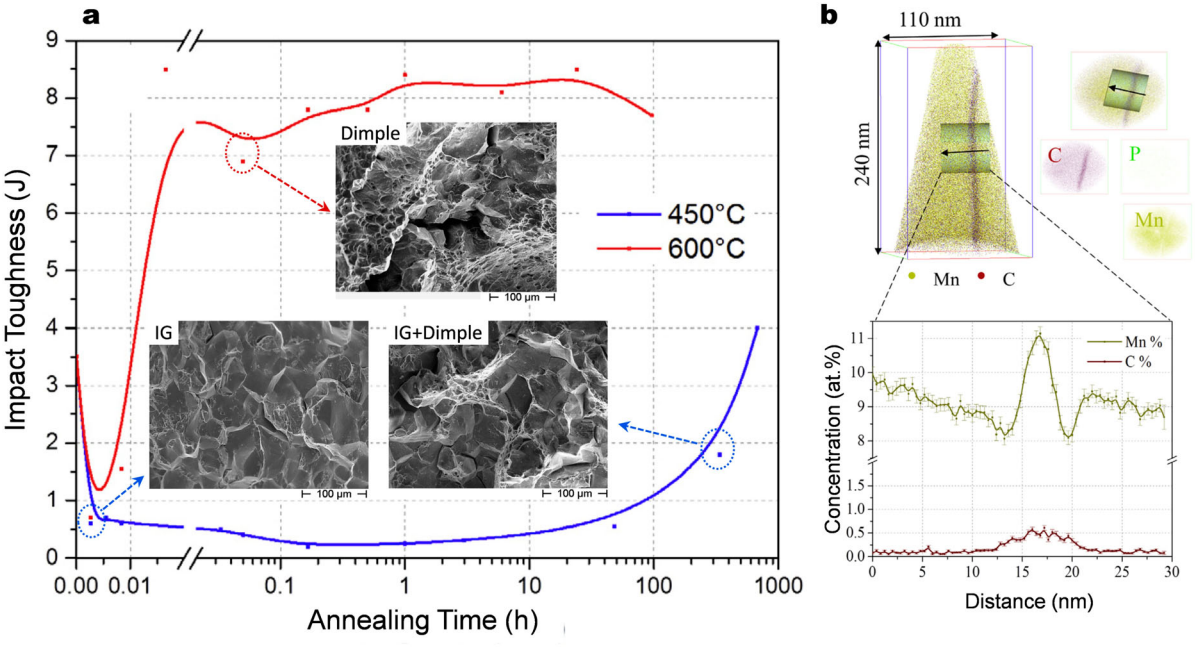

Figure 18. (a) Influence of annealing time on the room temperature Charpy impact toughness of a model Fe-9Mn (in wt-%) alloy, with the fracture surface of some conditions inset. Note that the specimens for the Charpy impact testing were subsize with a dimension of 3*4*27 mm^3. (b) The Mn segregation at a PAGB for the specimen annealed at 450°C for 1 min. The figure is reconstructed with permission from Ref. [217].

also found some degree of embrittlement of the steel when subjected to low-temperature impact testing. The detrimental effect of Mn segregation on the steels' toughness can also be inferred from the excess enthalpy of mixing of Fe and Mn for the BCC phase. At a relatively low tempering temperature (e.g. 450 °C as shown in Ref. [217]), Mn will segregate to the grain boundary due to the lower enthalpy of mixing of this element with Fe at these locations. Nevertheless, the mixing enthalpy of Mn and Fe is still positive and the total enthalpy of the boundary is increased by segregating Mn. As a result, when the alloy is cooled down and the atomic mobility is reduced, the grain boundary is quenched into a higher energy state compared to its state before the segregation took place, a factor that could facilitate its cracking.

Rationalization of processing-microstructure-mechanical property relations

Ultrafine grained austenite-ferrite two-phase microstructure

The microstructure type that has been subjected to the most detailed studies in the field of MMnS are austenite-ferrite two-phase microstructures with submicron grain size (as shown in Figure 19). Such ultrafine microstructure can be readily produced by simple intercritical annealing, a heat treatment process consisting of a heating stage to the intercritical two-phase domain, an isothermal holding stage allowing solute partitioning from ferrite to austenite and a cooling stage to retain the high-temperature microstructure. With higher intercritical annealing (IA) temperature, less C and Mn are enriched inside austenite (from a thermodynamic point of view) and the grain size of austenite also becomes coarser. These two factors reduce the austenite stability, which sometimes leads to the formation of martensite after rapid cooling. Depending on the initial microstructure, the intercritical ferrite and austenite can be either globular or laminated or a mixture of these two morphologies (Figure 19). One critical influencing factor is the stored energy in the starting microstructure, which subsequently serves as the driving force for static recrystallization during the IA process. A sufficiently large stored energy value, e.g. produced by dislocation accumulation through heavy cold rolling, gives rise to a high tendency for recrystallization that might occur before or during austenite formation at the IA temperature, thus resulting in a globular grain morphology [12,184]. On the other hand, when the initial microstructure mainly consists of quenched martensite (either after hot rolling and quenching or after a first annealing treatment), the driving force is not high enough for recrystallization or strong recovery [12,50,184]. The martensite microstructure, with its non-destroyed lath, packet, block and PAGB, serves as a template for the subsequently formed laminated structure (also shown in Figure 4).

Perhaps the most intriguing feature of intercritical annealed MMnS is their ultrafine grain size (or lamellar width for the laminated microstructure), which often reaches a submicron level. Explanations for this are not clear. The fact that low-alloyed DP steels, which undergo a similar rolling process and IA treatment, often show a much larger grain size (a few or a few tens of micrometers) [169,221] indicates that the ultrafine grain scale in IA-treated MMnS might be associated with the higher Mn content. Possible reasons were argued to be the effects of Mn on (a) lowering the IA temperatures, (b) broadening the ferrite-austenite-carbide three-phase field, (c) increasing the

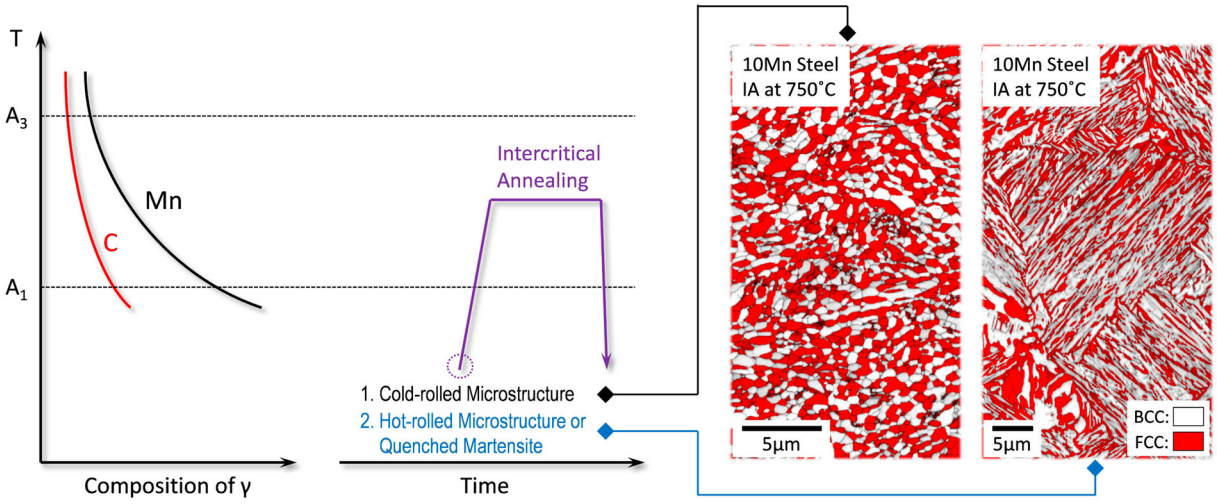

Figure 19. Schematic diagram showing the intercritical annealing process that is normally used to heat treat MMnS and the typical resulting microstructure (the EBSD phase plus IQ maps on the right side are from a 0.2C-10Mn-3Al-1Si (in wt-%) steel which was intercritically annealed from different initial conditions at 750°C for 5 min, followed by water quenching).

number of carbide particles that can pin grain boundaries and (d) reducing the grain/phase boundary mobility by solute drag [222,223]. Sun et al. [50] have found in a 10Mn steel, that the annealing at a relatively high IA temperature (800°C) only yielded a slight grain coarsening (from ~650 nm after 3 min to slightly above 1 mm after 60 min annealing). This grain stability should not involve any influence of intermediate carbide phases as the austenite reversion was nearly finished already after 3 min. These results seem to support the explanation that the solute drag effect of Mn seems to act as the dominant mechanism for the ultrafine grain size in MMnS, which, however, still needs further investigation.

The annealing temperature dependence of the room temperature tensile behaviour of a typical ultrafine austenite-ferrite MMnS is shown in Figure 20(a) (note that the samples annealed above 660°C contain certain fractions of martensite). For both types of grain morphologies, a higher annealing temperature results in a lower yield strength, mainly due to the coarser grain size and the lower dislocation density derived from more active recovery/recrystallization [14,197,200]. The strain-hardening rate, especially during the initial deformation regimes, is also increased with higher IA temperatures, which is mainly related to the lower C and Mn contents enriched within the austenite and its resulting lower mechanical stability (stronger TRIP effect) [14,47,184,200]. Other strain-hardening mechanisms could also play a role here, but the effects would be minor as already discussed in Section 4. Careful adjustment of the IA parameters and thus of the austenite stability and TRIP effect as well as the sequence of its activation and the deformation range over which it is triggered in this two-phase microstructure can lead to an optimized strength-ductility combination (up to ~80 GPa% in terms of the product of tensile strength and uniform elongation [14,27]).

A clear difference in the tensile behaviour between the globular and laminated microstructures is the more pronounced discontinuous yielding in the former case, which is manifested by a larger yield drop and yield point elongation (or Lüders strain) [12,50,184,224]. Sometimes the laminated microstructure even shows a continuous yielding behaviour, whereas clear discontinuous yielding prevails for the globular microstructure with a similar phase fraction (Figure 20(a)) [12,50,184]. Various mechanisms have been proposed to account for such difference. Han et al. [12] proposed that the softer and easily deformed ferrite phase in the globular microstructure was the major reason for the discontinuous yielding. In contrast for the laminated microstructure, both phases simultaneously yielded, and the TRIP effect occurred within the austenite provided strain-hardening and prevented localized Lüders bands formation. On the other hand, Steineder et al. [184] suggested that it was the enhanced dislocation interactions that provided the local strain-hardening ability in the laminated microstructure rather than the TRIP effect. Sun et al. [23,50] recently provided an alternative view based on their direct observation of the preferable dislocation nucleation at phase boundaries of MMnS (Figure 15(b)). More specific, it was proposed for the case of the laminated microstructure, that dislocations only tended to nucleate at the lamella tips due to the much higher number of pile-up dislocations and stress concentrations at these locations. This was assumed to strongly reduce the effective number of dislocation sources, producing a much lower dislocation density increase rate compared to steels with globular microstructures. As dislocation avalanches are the essential condition for the occurrence of discontinuous yielding (Section 3.4), the reduced

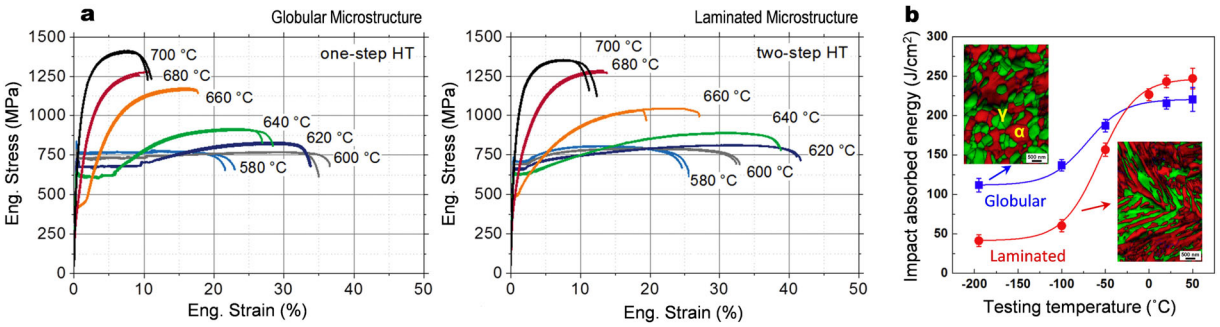

Figure 20. (a) Annealing temperature dependence of the room temperature tensile behaviour of a cold-rolled 0.1C-6.4Mn (in wt-%) steel treated to produce material variants with a globular and laminated microstructure, respectively. The globular microstructure was produced by IA treatments directly following cold rolling and the laminated microstructure was produced by a first austenitization treatment and then intercritical annealing. The IA time for all samples was 8 h. Note that samples subjected to IA temperatures above 660°C also contain certain fractions of martensite [184]. (b) Comparison of Charpy impact toughness between the two types of microstructures (data were taken from a 0.1C-7Mn-0.5Si steel in hot-rolled plus intercritical annealed condition (i.e. laminated) and cold-rolled plus intercritical annealed condition (i.e. globular) [40]). The figure is reconstructed with permission from Refs. [40,184].

dislocation multiplication rate in the laminated microstructure was believed to be the dominant reason for the suppressed discontinuous yielding.

Besides the differences in tensile properties, the two types of microstructure morphologies also show different fracture tolerance. Han et al. [12] have compared the Charpy impact toughness between the two microstructures with a similar phase fraction (Figure 20(b)). The laminated microstructure was shown to have an inferior impact toughness at low temperatures, which was claimed to be due to the unintentionally introduced P and Mn segregation at PAGBs and the facilitated interfacial cracking [12]. Since segregation of detrimental elements is highly relevant to the impurity level and the steel's processing history, the observed inferior impact toughness for the laminated microstructure cannot be considered as a universal rule. In fact, a variety of studies [13,15,225,226] have shown a beneficial role of laminated microstructures on fracture resistance, yet, with various operating mechanisms, such as interface delamination-induced toughening [15,225,226] and roughness-induced crack termination [13]. Whether these toughening effects work in the ultrafine laminated MMnS, however, requires further investigation.

With respect to the influence of grain morphology on the resistance to H embrittlement, the literature is in part in controversy. Han et al. [202] have studied the H embrittlement mechanisms of a 0.1C-7Mn-0.5Si (in wt-%) steel. They found that the two morphologies, with a similar austenite volume fraction (~50%) and mechanical stability, possessed a similar H concentration when subjected to the same H precharging procedure. However, a lower H-induced ductility loss (thus a better H embrittlement resistance) was observed for the material variant with globular microstructure. The authors attributed this finding to the more frequent deflection of H-induced cracks along the ultrafine equiaxed grains. However, different conclusions were drawn from the study of Jeong et al. [227] who found that the MMnS with laminated microstructure was more resistant to H embrittlement due to the slower H uptake and diffusivity associated with a higher degree of austenite percolation. The discrepancies among the different findings reported in literature might be caused by some unnoticed but important additional influencing factors such as the possible segregation of other detrimental elements [12], extent of localized plastic flow [224] and the amount of local H trapping [197], which might be greatly different between the two types of microstructures. It should also be taken into account in this context that different alloy compositions can also lead to different oxide layers and different H uptake kinetics for the different variants of these steels, so that sometimes there may not have been comparable H charging among the materials. Similar aspects have to be taken into account for the possible loss of H between charging and the actual tensile tests. This means that the comparability between different studies regarding the exact H embrittlement susceptibility is often only possible to a limited extent.

Austenite-martensite microstructure

A mixture of austenite and martensite has been considered as the ideal microstructure for the third-generation AHSS, as it combines the strongest phase (martensite) and the toughest phase (austenite) of steels which can theoretically result in an optimum mechanical performance [228]. Such microstructure can be produced in MMnS by a variety of ways. Perhaps the easiest method is by annealing the material into its fully austenitic state (above A_3), followed by rapid quenching (Route 1 shown in Figure 21). This will retain certain fractions of austenite within a martensite matrix when the C and Mn contents are sufficiently high to reduce the M_f (martensite finish) temperature below room temperature. However, the retained austenite produced through this processing route is not C or Mn enriched and thus is mechanically very unstable, which often transforms completely

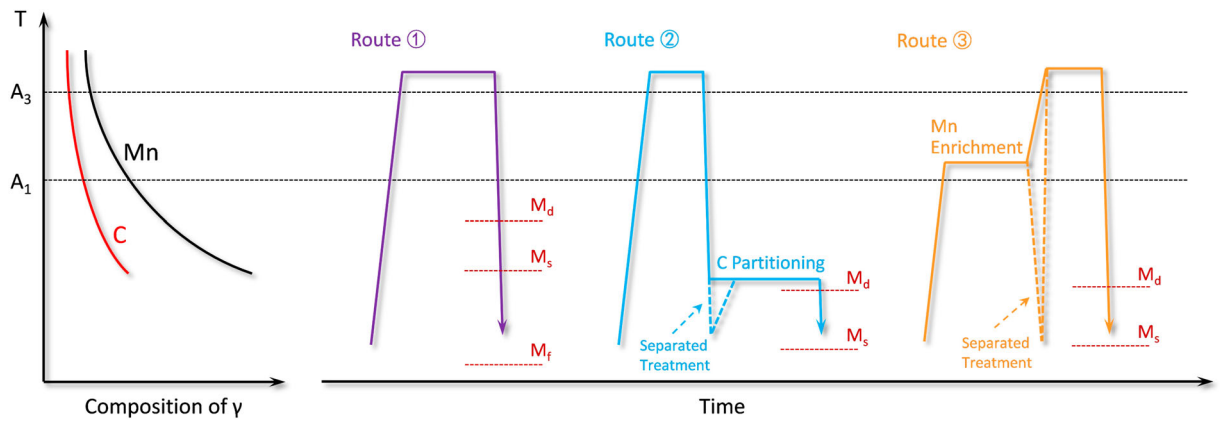

Figure 21. Different processing routes for producing austenite-martensite microstructure in MMnS. Routes 2 and 3 show two typical strategies to enhance the stability of austenite for a more persistent TRIP effect.

to martensite at early stages of deformation [3]. This means that the TRIP effect is easily exhausted which leads to only limited ductility of the material. In order to increase the austenite's mechanical stability, additional C partitioning treatments (Route 2 in Figure 21) and/or Mn enrichment treatments (Route 3 in Figure 21) in combination with the austenitization (or partial austenitization/intercritical annealing) were suggested [11,16,18,24,25,115,229,230]. These additional treatments can either be conducted within one thermal cycle along with the (partial) austenitization or in separated cycles (Figure 21). The C partitioning treatment is typically conducted at low temperatures where the diffusion of substitutional elements is negligible [16,25,229,230]. During this process, the formation of carbides is suppressed by the presence of Si and Al, thus C is likely to diffuse from the C-super-saturated quenched α'-martensite or deformation-induced α'-martensite into untransformed austenite. The related thermodynamics and kinetics of such process have been thoroughly reviewed in the literature [231,232]. On the other hand, the treatment required for Mn enrichment is often carried out within the intercritical range to allow for Mn partitioning from ferrite to austenite [11,18,229]. Due to the sluggish Mn diffusivity inside austenite, such locally enriched Mn can to some extent be maintained after austenization, thereby locally enhancing the stability of austenite [18,229]. Note that routes 2 and 3 in Figure 21 only provide two typical examples demonstrating the underlying principles for further stabilizing austenite. Different processing strategies with a similar purpose can also be explored and some of them utilizing chemical heterogeneity have already been covered in Section 3.3.

The tensile properties of MMnS containing martensite and austenite (also sometimes ferrite) are summarized in Figure 22(a), along with the data from the austenite-ferrite two-phase microstructure for comparison. It is demonstrated that the martensite-containing microstructure, fabricated by a single-step annealing, has a higher strength level than the intercritically annealed austenite-ferrite microstructure, but with a much lower ductility. Additional treatments for further C and/or Mn enrichment have led to an enhanced ductility with no sacrifice in strength. In some cases, the ductility can even be comparable to the austenite-ferrite microstructure (Figure 22(b)). This improved ductility is a result of the increased austenite mechanical stability which ensures a more persistent TRIP effect and strain hardening [18,42,115,229]. The tempering of martensite upon the partitioning treatment can also to some extent increase the ductility of the materials [18,42].

Bimodal microstructure

The bimodal microstructure in MMnS refers here to such microstructures that have a bimodal grain distribution consisting of a fine-grained γ+α aggregate (ranging from the submicron scale to only a few micrometers) and coarse δ-ferrite or austenite with a grain size normally above ~5 μm. Representative δ-ferrite containing and coarse-austenite containing bimodal microstructures are shown in Figure 23(a, b), respectively. The δ-ferrite generally exists in MMnS with a high Al and/or Si addition [2,17,31,198]. The increase of these elements strongly stabilizes ferrite and at a critical concentration, the single-phase austenite domain no longer exists in the

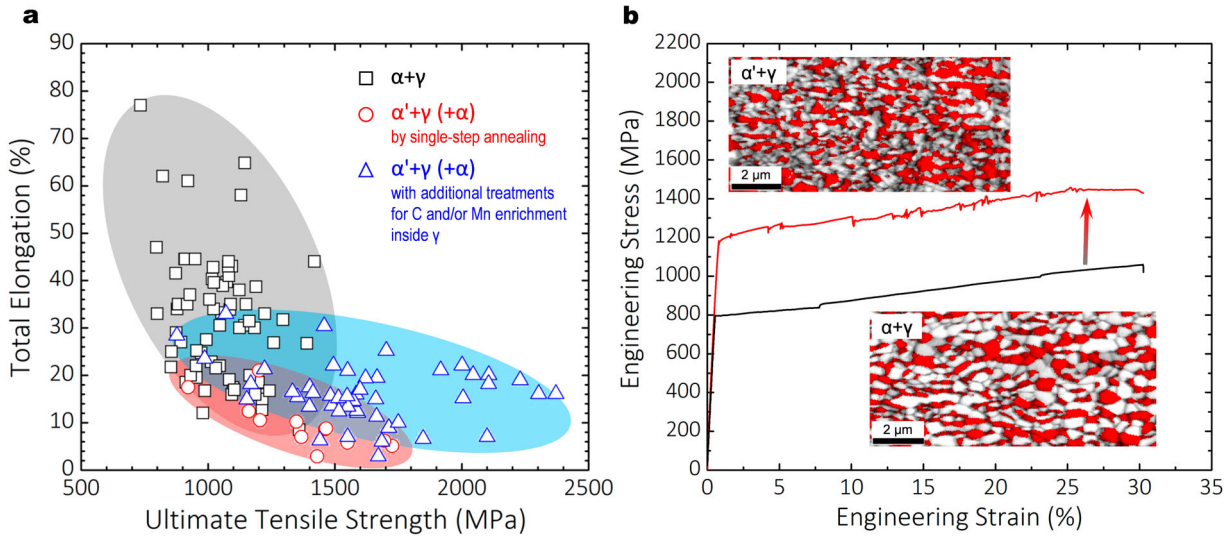

Figure 22. (a) Strength-ductility combinations of MMnS with different types of microstructure (plotted based on published data [1,8,14,16,18,42,47,68,141,151,192,229,233–245]); (b) Tensile behaviour of a 0.18C-8Mn (wt-%) steel fabricated to have either an austenite-ferrite microstructure (lower curve) and austenite-martensite microstructure (upper curve) with a similar austenite fraction (~44%); the austenite in the latter type of microstructure was stabilized by specially designed heat treatments for enabling sufficiently high-Mn and C enrichment. (b) is reconstructed with permission from Ref. [18].

phase diagram (Figure 23(a)). Above this critical point, the liquid phase directly transforms to the ferrite phase (often termed δ-ferrite) upon casting of the alloy. During the subsequent thermomechanical processing, there are certain fractions of δ-ferrite that do not participate into any phase transformation processes [17,176,200]. Although these ferrite grains can undergo recrystallization [200], the accomplished grain refinement level is lower than that achieved by reverse transformation, explaining the different grain scale between δ-ferrite and the reverted γ+α aggregate. The underlying reason for the formation of coarse-grained austenite in MMnS is similar. The only difference is that, in this case, the alloy is normally enriched with austenite stabilizers (e.g. C and Mn), which causes certain fractions of the austenite to remain during the whole casting and thermomechanical treatments without transforming into ferrite or martensite upon cooling or deformation [15,25,153,246,247].

It is important to note that the thermomechanical processing sequence of MMnS requires more care when a high amount of Al and/or Si is added and δ-ferrite is present. The unavoidable hot deformation (rolling or forging) within the austenite-ferrite two-phase domain increases the risks of damage formation and hot cracking. Figure 24(a) shows the mechanical response of a 0.2C-10Mn-3Al-3Si steel subjected to hot torsion tests at 1000°C and 1 s^{-1}. The sample demonstrates a strikingly early failure at ~1.0 strain, which is much lower than that measured for plane-carbon steels deformed above the A_3 temperature (up to more than 3.0 true strain [248]). The underlying reason for the poor hot ductility of the high-Al and/or high-Si MMnS has not been revealed. It can, however, be deduced that the plastic mismatch between the austenite and ferrite phase, resulting from their different hardness and kinetics/extent of dynamic restoration (Figure 24(b)), would result in high stress/strain concentrations at the phase boundaries which might promote damage formation.

Compared with material variants with ultrafine grained microstructure and globular grain morphology, the bimodal microstructure is more likely to show a continuous yielding behaviour [9,50,67,151,194,249]. This can be interpreted by the decreased interface area fraction due to the presence of the coarse grains, which effectively reduces the density of dislocation sources and thus suppresses the avalanching-driven increase in the number of mobile dislocations [50]. With respect to the strength-ductility combination, this type of microstructure performs similar to the ultrafine grained austenite-ferrite MMnS reviewed in Section 7.1. The characteristics of austenite and the associated strain-hardening capacity have also been considered as the key influencing factor for the overall tensile properties. However, it should be noted that the presence of the coarse grains has also been considered to promote the alloys' strain-hardening, due to the high amount of GNDs close to the interfaces with fine-grained microstructure regions and the triggered high back-stress hardening [250]. The relative contribution of this factor, in relation to other mechanisms such as TRIP and TWIP, requires further evaluation.

Further opportunities of microstructure design and improvement of the strength-ductility synergy

The aforementioned sections have revealed a large scope of possible microstructure conditions that can

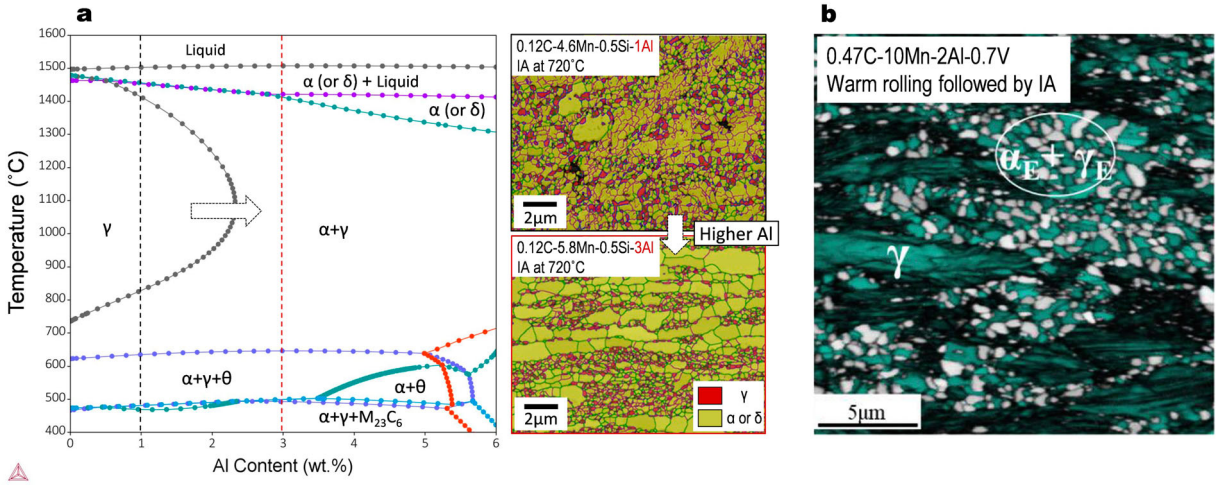

Figure 23. (a) Pseudo-binary equilibrium phase diagram for the 0.12C-5Mn-0.5Si-xAl steel system and typical microstructure of this steel system with different Al additions after cold rolling and intercritical annealing (IA) at 720°C. The steel with 3 wt-% Al shows a bimodal microstructure with coarse δ-ferrite. The phase diagram was calculated by the Thermo-Calc software using the TCFE 11 database. The EBSD figures were reconstructed with permission from Ref. [8]. (b) Typical bimodal microstructure with coarse-grained austenite (reconstructed with permission from Ref. [246]). The microstructure was acquired from a 0.47C-10Mn-2Al-0.7 V steel subjected to warm rolling and intercritical annealing at 620° C [246].

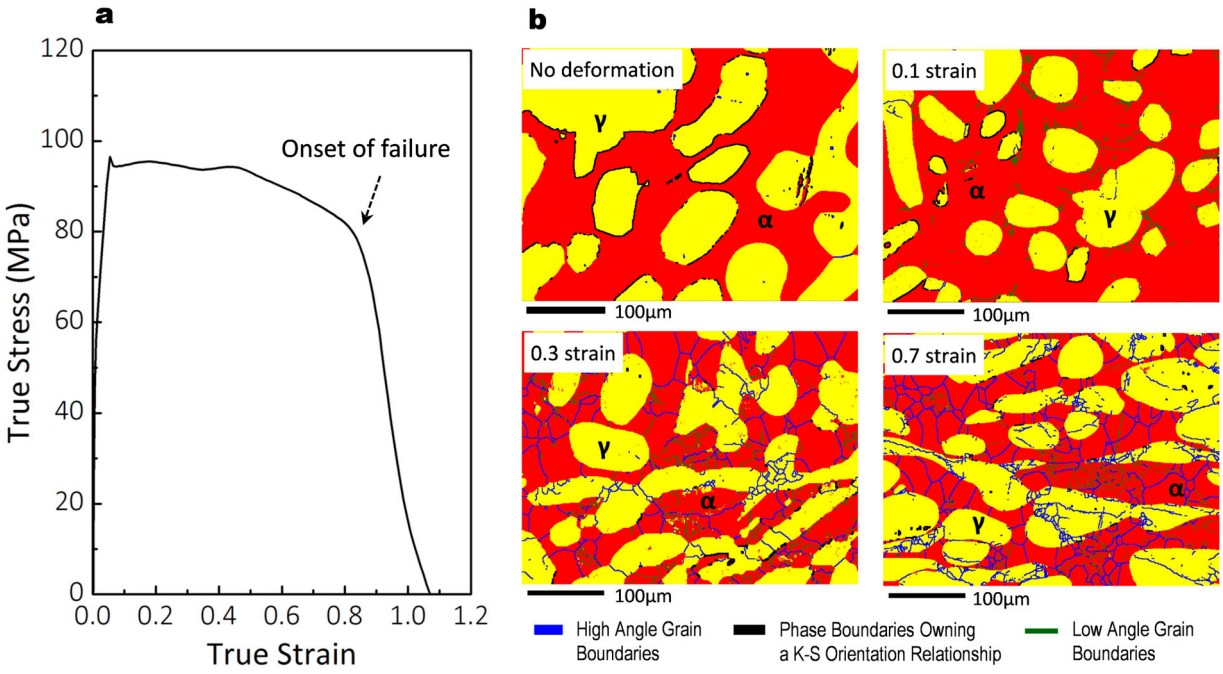

Figure 24. (a) True stress–strain curve of a 0.2C-10Mn-3Al-3Si steel subjected to hot torsion testing at 1000°C and 1 s^{-1}; (b) Microstructure evolution of the same steel during hot compression at the same temperature and strain rate, showing a higher extent/kinetics of dynamic recrystallization inside the ferrite phase compared with that in austenite and (b) is reconstructed with permission from Ref. [200].

be produced in MMnS, each allowing to activate and/or tweak a variety of deformation mechanisms. The access to such a large variety of different possible microstructure states is due to the medium-Mn content of these materials, which enlarges the processing window to control the characteristics of austenite and its transformation products. Previous literature has shown a very wide range of phase fractions (austenite typically from ~10 to ~80 vol.-% [10,247,251]), grain sizes (typically from ~200 nm to a few tens of micrometers [31,247,252]), morphologies (grain aspect ratio from ~1 to a few tens [12,50,252]) and austenite mechanical stability [10,47,143,197] that are tuneable in MMnS. The design and optimization of these microstructural factors have been subjected to a tremendous research effort in the field of MMnS, which has triggered the invention of many steel grades falling into that category with excellent mechanical performance. Figure 25 exhibits that the tensile strength-ductility combination of MMnS is superior than those of first-generation AHSS and can reach a similar level of properties as the second-generation high-Mn AHSS (Figure 25). Particularly, some of the grades can show an exceptional strength level (above 2 GPa) combined with a relatively high ductility (above 20%), a property spectrum that has not been reached by other types of bulk-produced steels or other bulk-produced metallic materials, to the best of the authors' knowledge.

Considering the wide compositional range and immense microstructural factors that are tuneable in MMnS, some more headroom probably still remains for further improvement of the alloys' mechanical properties. This goal can be achieved by continuous thermodynamics-aided optimization of the steels' composition, phase constituents and fractions, phase distribution and percolation, texture, grain size and morphology and the stability and deformation modes of austenite. In addition, a precise microstructure design at confined local regions could emerge as a new avenue for further advancement of MMnS. The

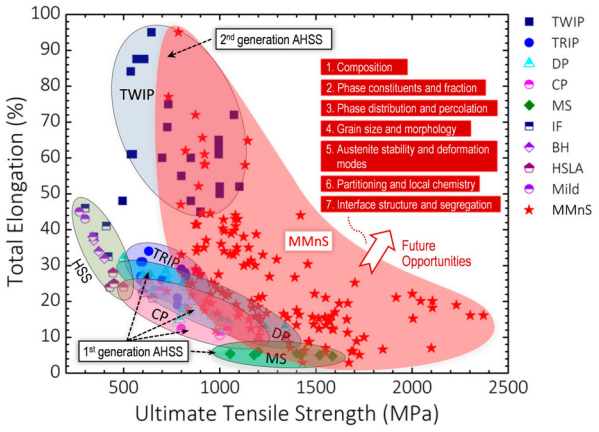

Figure 25. Comparison of tensile properties between MMnS and typical first/second-generation AHSS (plotted based on published data [1,8,14,16,18,26,42,47,68,141,151,192,229,233–245,253–262]). HSS: conventional high-strength steels, IF: interstitial-free steels, BH: bake hardenable steels, HSLA: high-strength low-alloy steels, Mild: mild steels, DP: dual-phase steels, CP: complex phase steels, MS: martensitic steels, TRIP: transformation-induced plasticity steels, TWIP: twinning-induced plasticity steels.

essence of such microstructure strategy lies in a careful control of solute enrichment and segregation within the grain interior or at lattice defects, with the aim to locally alter the mechanical properties to provide additional strengthening and/or damage-tolerant effects.

The influence of solute heterogeneity on localized austenite formation and decomposition has been reviewed in Section 3.3. A proper control of this localized phase transformation has been proven to be capable of providing a more persistent TRIP effect [11,18,42,115,229] or improving the local resistance to damages [19,24,217], enabling a better mechanical performance. On the other hand, the occurrence of solute segregation at lattice defects (e.g. dislocations and interfaces) have been occasionally reported in MMnS [15,22,23,31,40]. However, how to control such segregation to produce a positive effect on the mechanical behaviour remains poorly understood. The pioneering work from Ma et al. [23] provides some insights into this direction. They have studied the yielding behaviour of a 0.06C-11.7Mn-2.9Al steel subjected to intercritical annealing with varying cooling rates (i.e. water quenching and air cooling). A pronounced C segregation (~1.6 at-%) at the ferrite-austenite phase boundaries was observed in the air-cooled sample rather than the water-quenched steel variant, which was proposed to be driven by the requirement for the reduction of the interfacial energy (i.e. Gibbs adsorption isotherm) and/or by the C partitioning across the phase boundaries to maintain local equilibrium. Such chemical decoration impeded dislocation emission at phase boundaries and therefore increased the stress level for activating dislocation nucleation and initiating the plastic flow in both phases, which consequently resulted in a yield strength increase by more than 100 MPa [23]. This work thus highlights the importance of phase boundaries and their intrinsic characteristics, which should be considered as another factor involved in future microstructure manipulation strategies in MMnS.

Industrial relevance of MMnS

At the time of writing, the industrial development of MMnS with Mn contents in the range 3 wt-% < Mn < 12 wt-% is still at the pre-commercialization stage. This is actually quite curious, as the basic metallurgy was postulated exactly 50 years ago [1] and the application to cold-rolled sheets for the automotive sector has been pursued for more than a decade now. Further, carbon steels at both ends of this Mn spectrum are already in production, e.g. quenching and partitioning (Q&P) steels containing up to 3 wt-% Mn and Hadfield/TWIP grades with 12–22 wt-% Mn are available from multiple vendors [263–265].

Setting to one side the technical challenges described in this review, the most likely explanation is found in the economics of industrial processing. Steels with Mn contents up to 3 wt-% are straightforward to produce by both the standard blast furnace/basic oxygen furnace (BF/BOF) and electric arc furnace/ladle metallurgical furnace (EAF/LMF) routes, at a tariff that is not significantly greater than that of first-generation AHSS and therefore acceptable to automotive manufacturers. However, adding more Mn introduces a rapid escalation in production costs. For example, the standard BF/BOF process is complicated by the difficulty of maintaining sufficient temperature in the ladle treatment system during extensive ferromanganese additions. Recently, Voestalpine have reported on a successful industrial trial of an alloy containing 5.8 wt-% Mn using a Rurhstahl Heraeus (RH) vacuum degassing step in a BF/BOF plant [266], but have not published the Mn recovery rate. The alternative EAF production route requires the use of an argon oxygen decarburizing or vacuum oxygen decarburizing (AOD/VOD) station (i.e. a stainless steel plant) to prevent excessively low-Mn recovery. These economic issues are exacerbated when the high cost of the low C ferromanganese additions required for MMnS is taken into account, particularly where the P content must be controlled to reduce the susceptibility to H embrittlement. The latter difficulty can be solved using electrolytic Mn, usually at even greater expense. The development of TWIP steels has suffered from exactly the same economic handicaps and the long term future of TWIP alloys most likely lies outside of the automotive sector, for example in cryogenic applications [265].

Assuming that the steelmaking issues can be overcome, then continuous casting of MMnS is not expected to be problematic as long as the Al content can be kept low enough so that mold powder crystallization does not occur. Most of the other casting difficulties related to high-Mn alloying contents have already been resolved for Hadfield and TWIP grades. One additional constraint of MMnS production, compared to fully austenitic Mn steels, is the need for hot charging of slabs to the reheat furnace in order to avoid transformation stresses leading to cracking during slab cooling/reheating.

Regarding the downstream process, hot rolling of MMnS is usually not difficult (except for Al and Si levels sufficient to promote significant δ-ferrite formation), however, maintaining good temperature uniformity during coil cooling is an important parameter to avoid the development of hard spots. Cold rolling of martensitic structures is always an issue due to the high rolling loads and the associated difficulties to maintain good strip shape in wide formats. In fact, nearly all of the industrial processes so far proposed for MMnS involve an intermediate batch annealing step to soften the hot band. This introduces extra

costs and can be detrimental to the final properties. Further, experience has shown that MMnS are susceptible to edge cracking during cold rolling, which, in the worst cases, could lead to excessive edge trimming and low yields. Austenite reversion treatment in the intercritical temperature range is a crucial step in determining MMnS final properties. If this is done via a batch anneal process, then alloys which show strong variations in tensile properties within a very narrow temperature range are going to be unsuitable for production, as they will require extensive coil head/tail cropping leading to excessive wastage. Hence, the possibility of using continuous as opposed to batch annealing is obviously another important technical and economic improvement that needs to be pursued. Also, more advanced microstructural design approach through, for instance, controlling chemical heterogeneity or solute segregation at defects, for the optimization of mechanical properties often requires a more complex thermomechanical processing route and a more precise control of heat treatment parameters at each step. Whether this is feasible or affordable for large-scale industrial production remains an open question at this stage. The adaptability of the alloy and microstructure design approaches presented in this paper to the current industrial practice is thus an ongoing challenge which requires further research work on the development of adequate thermomechanical processes for MMnS and their compatibility with current process equipment. Finally, it is quite likely that the first commercial MMnS coils will be electrogalvanized as the difficulties involved in continuous galvannealed (GA)/galvanized (GI) strip production have not yet been overcome, although efforts are continuing [267].

Concerning MMnS in-use properties for the automotive sector, there are several areas where improvements are needed. One of these is the dynamical deformation properties at strain rates typical of anti-intrusion components under crash conditions (<10^3 s^{-1}). The presence of DSA in austenitic steels is usually accompanied by a NSRS within a certain range of strain rates and the same is true for many MMnS grades (see Figure 12(b)). This is an undesirable property which must be either eliminated or controlled. For example, Cai et al. [268] showed that the UTS of a Fe-0.2C-11Mn-2Al (in wt.-%) steel decreased from 1456 to 1086 MPa when the strain rate was increased from 2×10^{-4} s^{-1} to 2×10^{2} s^{-1}, although fortunately the yield strength and uniform elongation remained relatively constant. To counteract NSRS, MMnS alloys with a positive strain rate sensitivity (PSRS) have been produced [269], but so far the overall mechanical properties obtained for PSRS alloys are inferior to their NSRS counterparts. Weldability is another crucial parameter for alloy acceptance. Resistance spot welding (RSW) and laser welding are the two most widely used techniques used for automotive structure assemblies. MMnS spot welds can show low load bearing capacity due to Mn segregation between martensite laths which decreases the crack resistance in the fusion zone and promotes the interfacial failure mode under shear-tension loading [270]. Laser welding shows similar problems related to martensite formation [271]. One solution that has been proposed for spot welds is to introduce a Ni interlayer between the MMnS sheets to suppress martensite formation in the weld nugget [270]. The presence of a Zn coating can also result in liquid metal embrittlement of spot welds although this can be mitigated by reducing the alloy Si content [272].

The current challenge for MMnS industrialization is thus twofold. First, greater efforts need to be made to reduce the overall processing costs and to improve the properties robustness. Second, steelmakers and automotive manufacturers need to see a clear distinction between MMnS and competing metallurgies (e.g. carbon-free bainitic steels and Q&P steels), either in terms of performance or costs or ease of use. One very interesting possibility lies in the direct production of thin gauge (<1.5 mm) hot-rolled MMnS strip that is now possible using the most recent hot strip mills (HSMs). These products would be significantly less expensive than cold-rolled equivalents and can show better processing robustness.

Summary and outlook

Extensive work during the last ~15 years has led to significant progress in the field of MMnS, especially pertaining to novel microstructure design, rooted in the understanding of phase transformation thermodynamics and kinetics, and to the leap of mechanical performance that has been achieved (Figure 25). Such excellent strength-ductility combinations, achieved with relatively lean composition in these steels mark the key driving force for their further development and application. Advances on the basic understanding of MMnS have also been achieved in the last decade, particularly in austenite reversion and solute partitioning kinetics, thermodynamics of local solute enrichment, austenite deformation behaviour and the impact of deformation-induced martensite transformation on yielding, strain-hardening behaviour and damage evolution (with or without the presence of H). However, the level of understanding in microstructural and micromechanical fundamentals of MMnS is still far less than what has been achieved for other types of steels (e.g. DP and TWIP steels). This is largely due to their immense complexity which directly links to the medium-Mn content and the resulting multiphase microstructure with a large scope of tuneable phase constituents and conditions. Therefore, a number of opportunities are still pending for further fundamental research in this field. In this context, unresolved basic topics include, but are not

limited to: (a) the nucleation of austenite from different complex initial microstructural states; (b) interface mobility and phase growth; (c) the interaction between recrystallization and austenite reversion; (d) local chemistry and austenite reversion/stability; (e) nucleation mechanisms of deformation-induced martensite; (f) quantitative contribution of individual deformation mechanisms to overall tensile performance; (g) detailed characteristics of PLC bands and the associated DSA mechanisms; (h) the effects of micro-alloying and precipitation; and (i) the characteristics of various types of interfaces and their relevance for damage and H embrittlement.

In addition, another critical research direction is to develop reliable microstructure and constitutive micromechanical models that provide quantitative guidance for further optimization and discovery of alternative composition and microstructure variants. The accurate control of local chemistry within the grain interior or at the interfaces have appeared as a novel and effective microstructure engineering method for the enhancement of the steels' strength, strain-hardening ability and damage tolerance. Further exploration utilizing this strategy is encouraged, however, the complexity of the required thermomechanical processing should be minimized when considering the compatibility to the current industrial practice. In summary, the current limits on the fundamental understanding of MMnS indicate that there is plenty of room for their further development, which justifies future research efforts from both a scientific and engineering perspective. These research activities are likely to continuously bring new knowledge to the whole community of steels, just like what has happened in the last ~15 years.

Disclosure statement

No potential conflict of interest was reported by the author(s).

Funding

Binhan Sun acknowledges the financial support from the National Natural Science Foundation of China [grant number 52275147]. Hao Chen acknowledges the financial support from National Key R&D program of China (Grant 2022YFE0110800 and 2022YFB3705203) and the National Natural Science Foundation of China (grants 51922054 and U1808208).

ORCID

Binhan Sun http://orcid.org/0000-0001-9561-7019

References

[1] Miller RL. Ultrafine-grained microstructures and mechanical properties of alloy steels. Metall Trans. 1972;3:905–912.
[2] Chen S, Rana R, Haldar A, et al. Current state of Fe-Mn-Al-C low density steels. Prog Mater Sci. 2017;89:345–391.
[3] Gibbs P. Design considerations for the third generation advanced high strength steel. PhD thesis, Colorado School of Mines; 2012.
[4] Hu B, Luo H, Yang F, et al. Recent progress in medium-Mn steels made with new designing strategies, a review. J Mater Sci Technol. 2017;33:1457–1464.
[5] Kim H, Suh DW, Kim NJ. Fe-Al-Mn-C lightweight structural alloys: a review on the microstructures and mechanical properties. Sci Technol Adv Mater. 2013;14:014205.
[6] Lee YK, Han J. Current opinion in medium manganese steel. Mater Sci Technol. 2014;31:843–856.
[7] Suh D-W, Kim S-J. Medium Mn transformation-induced plasticity steels: recent progress and challenges. Scr Mater. 2017;126:63–67.
[8] Suh D-W, Park S-J, Lee T-H, et al. Influence of Al on the microstructural evolution and mechanical behavior of low-carbon, manganese transformation-induced-plasticity steel. Metall Mater Trans A. 2010;41:397–408.
[9] Sun B, Fazeli F, Scott C, et al. The influence of silicon additions on the deformation behavior of austenite-ferrite duplex medium manganese steels. Acta Mater. 2018;148:249–262.
[10] Sun B, Fazeli F, Scott C, et al. Microstructural characteristics and tensile behavior of medium manganese steels with different manganese additions. Mater Sci Eng A. 2018;729:496–507.
[11] De Moor E, Speer J, Matlock D, et al. Heat treating opportunities for medium manganese steels. Proceedings of the First International Conference on Automobile Steel & the 3rd International Conference on High Manganese Steels, Chengdu, China; 2016: p. 15–18.
[12] Han J, Lee S-J, Jung J-G, et al. The effects of the initial martensite microstructure on the microstructure and tensile properties of intercritically annealed Fe-9Mn-0.05 C steel. Acta Mater. 2014;78:369–377.
[13] Koyama M, Zhang Z, Wang M, et al. Bone-like crack resistance in hierarchical metastable nanolaminate steels. Science. 2017;355:1055–1057.
[14] Lee S, De Cooman BC. Annealing temperature dependence of the tensile behavior of 10 pct Mn multi-phase TWIP-TRIP steel. Metall Mater Trans A. 2014;45:6039–6052.
[15] Liu L, Yu Q, Wang Z, et al. Making ultrastrong steel tough by grain-boundary delamination. Science. 2020;368:1347–1352.
[16] Seo EJ, Cho L, Estrin Y, et al. Microstructure-mechanical properties relationships for quenching and partitioning (Q&P) processed steel. Acta Mater. 2016;113:124–139.
[17] Sun B, Fazeli F, Scott C, et al. Phase transformation behavior of medium manganese steels with 3 wt pct aluminum and 3 wt pct silicon during intercritical annealing. Metall Mater Trans A. 2016;47:4869–4882.
[18] Ding R, Yao Y, Sun B, et al. Chemical boundary engineering: a new route toward lean, ultrastrong yet ductile steels. Sci Adv. 2020;6:eaay1430.
[19] Raabe D, Sandlöbes S, Millán J, et al. Segregation engineering enables nanoscale martensite to austenite phase transformation at grain boundaries: a

pathway to ductile martensite. Acta Mater. 2013;61:6132–6152.
[20] Da Silva AK, Ponge D, Peng Z, et al. Phase nucleation through confined spinodal fluctuations at crystal defects evidenced in Fe-Mn alloys. Nat Commun. 2018;9:1137.
[21] Belde M, Springer H, Inden G, et al. Multiphase microstructures via confined precipitation and dissolution of vessel phases: example of austenite in martensitic steel. Acta Mater. 2015;86:1–14.
[22] Kuzmina M, Herbig M, Ponge D, et al. Linear complexions: confined chemical and structural states at dislocations. Science. 2015;349:1080–1083.
[23] Ma Y, Sun B, Schökel A, et al. Phase boundary segregation-induced strengthening and discontinuous yielding in ultrafine-grained duplex medium-Mn steels. Acta Mater. 2020;200:389–403.
[24] Sun B, Lu W, Gault B, et al. Chemical heterogeneity enhances hydrogen resistance in high-strength steels. Nat Mater. 2021;20:1629–1634.
[25] He B, Hu B, Yen H, et al. High dislocation density-induced large ductility in deformed and partitioned steels. Science. 2017;357:1029–1032.
[26] Sohn SS, Song H, Kwak JH, et al. Dramatic improvement of strain hardening and ductility to 95% in highly-deformable high-strength duplex lightweight steels. Sci Rep. 2017;7:1927.
[27] Yang F, Zhou J, Han Y, et al. A novel cold-rolled medium Mn steel with an ultra-high product of tensile strength and elongation. Mater Lett. 2020;258:126804.
[28] Ma Y. Medium-manganese steels processed by austenite-reverted-transformation annealing for automotive applications. Mater Sci Technol. 2017;33:1713–1727.
[29] Furukawa T, Huang H, Matsumura O. Effects of carbon content on mechanical properties of 5% Mn steels exhibiting transformation induced plasticity. Mater Sci Technol. 1994;10:964–970.
[30] Zhao C, Song R, Zhang L, et al. Effect of annealing temperature on the microstructure and tensile properties of Fe-10Mn-10Al-0.7 C low-density steel. Mater Des. 2016;91:348–360.
[31] Sun B, Palanisamy D, Ponge D, et al. Revealing fracture mechanisms of medium manganese steels with and without delta-ferrite. Acta Mater. 2019;164:683–696.
[32] Andrews K. Empirical formulae for the calculation of some transformation temperatures. J Iron Steel Inst. 1965;203:721–727.
[33] Capdevila C, et al. Determination of Ms temperature in steels: a bayesian neural network model. ISIJ international. 2002;42:894–902.
[34] Grange R, Stewart H. The temperature range of martensite formation. Trans AIME. 1946;167:467–501.
[35] Lee T-H, Oh C-S, Kim S-J. Effects of nitrogen on deformation-induced martensitic transformation in metastable austenitic Fe-18Cr-10Mn-N steels. Scr Mater. 2008;58:110–113.
[36] Angel T. Formation of martensite in austenitic stainless steels-effects of deformation, temperature, and composition. J Iron Steel Inst. 1954;177:165.
[37] Lee Y-K, Choi C. Driving force for γ→ε martensitic transformation and stacking fault energy of γ in Fe-Mn binary system. Metall Mater Trans A. 2000;31:355–360.
[38] Cabanas N, Penning J, Akdut N, et al. High-temperature deformation properties of austenitic Fe-Mn alloys. Metall Mater Trans A. 2006;37:3305–3315.
[39] De Cooman BC. High Mn TWIP steel and medium Mn steel. In: Radhakanta Rana and Shiv Brat Singh, editors. Automotive steels. Woodhead Publishing; 2017. p. 317–385.
[40] Han J, da Silva AK, Ponge D, et al. The effects of prior austenite grain boundaries and microstructural morphology on the impact toughness of intercritically annealed medium Mn steel. Acta Mater. 2017;122:199–206.
[41] Kwiatkowski da Silva A, Kamachali RD, Ponge D, et al. Thermodynamics of grain boundary segregation, interfacial spinodal and their relevance for nucleation during solid-solid phase transitions. Acta Mater. 2019;168:109–120.
[42] Sun WW, Wu YX, Yang SC, et al. Advanced high strength steel (AHSS) development through chemical patterning of austenite. Scr Mater. 2018;146:60–63.
[43] Latypov MI, Shin S, De Cooman BC, et al. Micromechanical finite element analysis of strain partitioning in multiphase medium manganese TWIP+TRIP steel. Acta Mater. 2016;108:219–228.
[44] Lee T-H, Ha H-Y, Hwang B, et al. Effect of carbon fraction on stacking fault energy of austenitic stainless steels. Metall Mater Trans A. 2012;43:4455–4459.
[45] Brofman P, Ansell G. On the effect of carbon on the stacking fault energy of austenitic stainless steels. Metall Mater Trans A. 1978;9:879–880.
[46] Lee T-H, Shin E, Oh C-S, et al. Correlation between stacking fault energy and deformation microstructure in high-interstitial-alloyed austenitic steels. Acta Mater. 2010;58:3173–3186.
[47] Gibbs P, De Moor E, Merwin M, et al. Austenite stability effects on tensile behavior of manganese-enriched-austenite transformation-induced plasticity steel. Metall Mater Trans A. 2011;42:3691–3702.
[48] Wang X, Wang L, Huang M. Kinematic and thermal characteristics of Lüders and Portevin-Le Châtelier bands in a medium Mn transformation-induced plasticity steel. Acta Mater. 2017;124:17–29.
[49] Sun B, Vanderesse N, Fazeli F, et al. Discontinuous strain-induced martensite transformation related to the Portevin-Le Chatelier effect in a medium manganese steel. Scr Mater. 2017;133:9–13.
[50] Sun B, Ma Y, Vanderesse N, et al. Macroscopic to nanoscopic in situ investigation on yielding mechanisms in ultrafine grained medium Mn steels: role of the austenite-ferrite interface. Acta Mater. 2019;178:10–25.
[51] Elkot MN, Sun B, Zhou X, et al. Hydrogen-assisted decohesion associated with nanosized grain boundary κ-carbides in a high-Mn lightweight steel. Acta Mater. 2022;241:118392.
[52] Oh B, Cho S, Kim Y, et al. Effect of aluminium on deformation mode and mechanical properties of austenitic Fe-Mn-Cr-Al-C alloys. Mater Sci Eng A. 1995;197:147–156.
[53] Kim J, Lee S-J, De Cooman BC. Effect of Al on the stacking fault energy of Fe-18Mn-0.6 C twinning-induced plasticity. Scr Mater. 2011;65:363–366.
[54] Lehnhoff G, Findley K, De Cooman B. The influence of silicon and aluminum alloying on the lattice parameter and stacking fault energy of austenitic steel. Scr Mater. 2014;92:19–22.
[55] Kang M, Woo W, Lee Y-K, et al. Neutron diffraction analysis of stacking fault energy in Fe–18Mn–2Al–0.6 C twinning-induced plasticity steels. Mater Lett. 2012;76:93–95.

[56] Saeed-Akbari A, Imlau J, Prahl U, et al. Derivation and variation in composition-dependent stacking fault energy maps based on subregular solution model in high-manganese steels. Metall Mater Trans A. 2009;40:3076–3090.
[57] Ryu JH, Kim SK, Lee CS, et al. Effect of aluminium on hydrogen-induced fracture behaviour in austenitic Fe-Mn-C steel. Proc R. Soc A Math, Phys Eng Sci. 2013;469:20120458.
[58] Koyama M, Akiyama E, Lee Y-K, et al. Overview of hydrogen embrittlement in high-Mn steels. Int J Hydrogen Energy. 2017;42:12706–12723.
[59] Song EJ, Bhadeshia H, Suh D-W. Interaction of aluminium with hydrogen in twinning-induced plasticity steel. Scr Mater. 2014;87:9–12.
[60] Han D, Lee S, Noh S, et al. Effect of aluminium on hydrogen permeation of high-manganese twinning-induced plasticity steel. Scr Mater. 2015;99:45–48.
[61] Park I-J, Jeong K-H, Jung J-G, et al. The mechanism of enhanced resistance to the hydrogen delayed fracture in Al-added Fe–18Mn–0.6 C twinning-induced plasticity steels. Int J Hydrogen Energy. 2012;37:9925–9932.
[62] Shun T, Wan C, Byrne J. A study of work hardening in austenitic Fe-Mn-C and Fe-Mn-Al-C alloys. Acta Metall Mater. 1992;40:3407–3412.
[63] De Cooman BC, Estrin Y, Kim SK. Twinning-induced plasticity (TWIP) steels. Acta Mater. 2018;142:283–362.
[64] Dumay A, Chateau JP, Allain S, et al. Influence of addition elements on the stacking-fault energy and mechanical properties of an austenitic Fe-Mn-C steel. Mater Sci Eng A. 2008;483–484:184–187.
[65] Miyazaki T, Kozakai T, Tsuzuki T. Phase decompositions of Fe-Si-Al ordered alloys. J Mater Sci. 1986;21:2557–2564.
[66] Marker MC, Skolyszewska-Kuhberger B, Effenberger HS, et al. Phase equilibria and structural investigations in the system Al-Fe-Si. Intermetallics. 2011;19:1919–1929.
[67] Lee S, Estrin Y, De Cooman BC. Constitutive modeling of the mechanical properties of V-added medium manganese TRIP steel. Metall Mater Trans A. 2013;44:3136–3146.
[68] He BB, Hu B, Yen HW, et al. High dislocation density-induced large ductility in deformed and partitioned steels. Science. 2017;357:1029–1032.
[69] Cai M, Li Z, Chao Q, et al. A novel Mo and Nb microalloyed medium Mn trip steel with maximal ultimate strength and moderate ductility. Metall Mater Trans A. 2014;45:5624–5634.
[70] Han Y, Shi J, Xu L, et al. Effects of Ti addition and reheating quenching on grain refinement and mechanical properties in low carbon medium manganese martensitic steel. Mater Des. 2012;34:427–434.
[71] Bhadeshia HKDH. Prevention of hydrogen embrittlement in steels. ISIJ Int. 2016;56:24–36.
[72] Park TM, Kim H-J, Um HY, et al. The possibility of enhanced hydrogen embrittlement resistance of medium-Mn steels by addition of micro-alloying elements. Mater Charact. 2020;165:110386.
[73] Xu Z, Shen X, Allam T, et al. Austenite reversion and nano-precipitation during a compact two-step heat treatment of medium-Mn steel containing Cu and Ni. J Mater Res Technol. 2022;17:2601–2613.
[74] Li S, Wen P, Li S, et al. A novel medium-Mn steel with superior mechanical properties and marginal oxidization after press hardening. Acta Mater. 2021;205:116567.
[75] Allam T, Guo X, Sevsek S, et al. Development of a Cr-Ni-VN medium manganese steel with balanced mechanical and corrosion properties. Metals (Basel). 2019;9:705.
[76] De Moor E, Matlock DK, Speer JG, et al. Austenite stabilization through manganese enrichment. Scr Mater. 2011;64:185–188.
[77] Van Bohemen S. Bainite and martensite start temperature calculated with exponential carbon dependence. Mater Sci Technol. 2012;28:487–495.
[78] Dai ZB, Chen H, Ding R, et al. Fundamentals and application of solid-state phase transformations for advanced high strength steels containing metastable retained austenite. Mater Sci Eng R-Reports. 2021;143:100590.
[79] Wycliffe PA, Purdy GR, Embury JD. Growth of austenite in the intercritical annealing of Fe-C-Mn dual phase steels. Can Metall Q. 1981;20:339–350.
[80] Ågren J. Computer simulations of the austenite/ferrite diffusional transformations in low alloyed steels. Acta Metall. 1982;30:841–851.
[81] Wei R, Enomoto M, Hadian R, et al. Growth of austenite from as-quenched martensite during intercritical annealing in an Fe-0.1 C-3Mn-1.5 Si alloy. Acta Mater. 2013;61:697–707.
[82] Huyan F, Yan J-Y, Höglund L, et al. Simulation of the growth of austenite from as-quenched martensite in medium Mn steels. Metall Mater Trans A. 2018;49:1053–1060.
[83] Wu YX, Sun WW, Gao X, et al. The effect of alloying elements on cementite coarsening during martensite tempering. Acta Mater. 2020;183:418–437.
[84] Miyamoto G, Usuki H, Li Z-D, et al. Effects of Mn, Si and Cr addition on reverse transformation at 1073 K from spheroidized cementite structure in Fe-0.6 mass % C alloy. Acta Mater. 2010;58:4492–4502.
[85] Wu YX, Sun WW, Styles MJ, et al. Cementite coarsening during the tempering of Fe-C-Mn martensite. Acta Mater. 2018;159:209–224.
[86] Wu YX, Wang LY, Sun WW, et al. Austenite formation kinetics from multicomponent cementite-ferrite aggregates. Acta Mater. 2020;196:470–487.
[87] Mueller JJ, Hu X, Sun X, et al. Austenite formation and cementite dissolution during intercritical annealing of a medium-manganese steel from a martensitic condition. Mater Des. 2021;203:109598.
[88] Lai Q, Gouné M, Perlade A, et al. Mechanism of austenite formation from spheroidized microstructure in an intermediate Fe-0.1 C-3.5 Mn steel. Metall Mater Trans A. 2016;47:3375–3386.
[89] Nehrenberg A. The growth of austenite as related to prior structure. JOM. 1950;2:162–174.
[90] Kimmins S, Gooch D. Austenite memory effect in 1Cr-1Mo-0.75V (Ti, B) steel. Metal Science. 1983;17:519–532.
[91] Zhang X, Miyamoto G, Toji Y, et al. Orientation of austenite reverted from martensite in Fe-2Mn-1.5Si-0.3C alloy. Acta Mater. 2018;144:601–612.
[92] Dmitrieva O, Ponge D, Inden G, et al. Chemical gradients across phase boundaries between martensite and austenite in steel studied by atom probe tomography and simulation. Acta Mater. 2011;59:364–374.
[93] Zhang X, Miyamoto G, Kaneshita T, et al. Growth mode of austenite during reversion from martensite in Fe-2Mn-1.5Si-0.3C alloy: a transition in kinetics and morphology. Acta Mater. 2018;154:1–13.

[94] Huang J, Poole W, Militzer M. Austenite formation during intercritical annealing. Metall Mater Trans A. 2004;35:3363–3375.
[95] Zheng C, Raabe D. Interaction between recrystallization and phase transformation during intercritical annealing in a cold-rolled dual-phase steel: a cellular automaton model. Acta Mater. 2013;61:5504–5517.
[96] Kulakov M, Poole W, Militzer M. The effect of the initial microstructure on recrystallization and austenite formation in a DP600 steel. Metall Mater Trans A. 2013;44:3564–3576.
[97] Ollat M, Massardier V, Fabregue D, et al. Modeling of the recrystallization and austenite formation overlapping in cold-rolled dual-phase steels during intercritical treatments. Metall Mater Trans A. 2017;48:4486–4499.
[98] Garcia CI, Deardo AJ. Formation of austenite in 1.5 pct Mn steels. Metall Trans A. 1981;12:521–530.
[99] Kozeschnik E. A Scheil-Gulliver model with back-diffusion applied to the microsegregation of chromium in Fe-Cr-C alloys. Metall Mater Trans A. 2000;31:1682–1684.
[100] Inden G. Ordering and segregation reactions in b.c.c. binary alloys. Acta Metall. 1974;22:945–951.
[101] Büth J, Inden G. Ordering and segregation reactions in f.c.c. binary alloys. Acta Metall. 1982;30:213–224.
[102] Gault B, Breen AJ, Chang Y, et al. Interfaces and defect composition at the near-atomic scale through atom probe tomography investigations. J Mater Res. 2018;23:4018–4030.
[103] Kwiatkowski da Silva A, Inden G, Kumar A, et al. Competition between formation of carbides and reversed austenite during tempering of a medium-manganese steel studied by thermodynamic-kinetic simulations and atom probe tomography. Acta Mater. 2018;147:165–175.
[104] Kwiatkowski da Silva A, Leyson G, Kuzmina M, et al. Confined chemical and structural states at dislocations in Fe-9wt%Mn steels: a correlative TEM-atom probe study combined with multiscale modelling. Acta Mater. 2017;124:305–315.
[105] Kwiatkowski da Silva A, Souza Filho IR, Lu W, et al. A sustainable ultra-high strength Fe18Mn3Ti maraging steel through controlled solute segregation and α-Mn nanoprecipitation. Nat Commun. 2022;13:2330.
[106] Guttmann M. Equilibrium segregation in a ternary solution-model for temper embrittlement. Surf Sci. 1975;53:213–227.
[107] Guttmann M. Grain-boundary segregation, two dimensional compound formation, and precipitation. Metall Trans A. 1977;8:1383–1401.
[108] Lejček P. Models of equilibrium grain boundary segregation. In: Pavel Lejcek, editor. Grain boundary segregation in metals. Berlin: Springer; 2010. p. 51–102.
[109] Darvishi Kamachali R, Kwiatkowski da Silva A, McEniry E, et al. Segregation-assisted spinodal and transient spinodal phase separation at grain boundaries. NPJ Comput Mater. 2020;6:191.
[110] Souza Filho IR, Kwiatkowski da Silva A, Sandim MJR, et al. Martensite to austenite reversion in a high-Mn steel: partitioning-dependent two-stage kinetics revealed by atom probe tomography, in-situ magnetic measurements and simulation. Acta Mater. 2019;166:178–191.
[111] Peng Z, Lu Y, Hatzoglou C, et al. An automated computational approach for complete in-plane compositional interface analysis by atom probe tomography. Microsc Microanal. 2019;25:389–400.
[112] Benzing JT, Kwiatkowski da Silva A, Morsdorf L, et al. Multi-scale characterization of austenite reversion and martensite recovery in a cold-rolled medium-Mn steel. Acta Mater. 2019;166:512–530.
[113] Lee H, Jo MC, Sohn SS, et al. Novel medium-Mn (austenite+martensite) duplex hot-rolled steel achieving 1.6 GPa strength with 20% ductility by Mn-segregation-induced TRIP mechanism. Acta Mater. 2018;147:247–260.
[114] Liu G, Li T, Yang Z, et al. On the role of chemical heterogeneity in phase transformations and mechanical behavior of flash annealed quenching & partitioning steels. Acta Mater. 2020;201:266–277.
[115] Sun B, Ding R, Brodusch N, et al. Improving the ductility of ultrahigh-strength medium Mn steels via introducing pre-existed austenite acting as a "reservoir" for Mn atoms. Mater Sci Eng A. 2019;749:235–240.
[116] Liu G, Dai Z, Yang Z, et al. Kinetic transitions and Mn partitioning during austenite growth from a mixture of partitioned cementite and ferrite: role of heating rate. J Mater Sci Technol. 2020;49:70–80.
[117] Kim JH, Gu G, Koo M, et al. Enhanced ductility of as-quenched martensite by highly stable nano-sized austenite. Scr Mater. 2021;201:113955.
[118] Kim JH, Kwon M-H, Gu G, et al. Quenching and partitioning (Q&P) processed medium Mn steel starting from heterogeneous microstructure. Materialia. 2020;12:100757.
[119] Kim JH, Gu G, Kwon M-H, et al. Microstructure and tensile properties of chemically heterogeneous steel consisting of martensite and austenite. Acta Mater. 2022;223:117506.
[120] Wang M, Jiang M, Tasan CC. Manganese micro-segregation governed austenite re-reversion and its mechanical effects. Scr Mater. 2020;179:75–79.
[121] Jeong MS, Park TM, Choi S, et al. Recovering the ductility of medium-Mn steel by restoring the original microstructure. Scr Mater. 2021;190:16–21.
[122] Enomoto M, Li S, Yang Z, et al. Partition and non-partition transition of austenite growth from a ferrite and cementite mixture in hypo-and hypereutectoid Fe-C-Mn alloys. Calphad. 2018;61:116–125.
[123] Wan X, Liu G, Ding R, et al. Stabilizing austenite via a core-shell structure in the medium Mn steels. Scr Mater. 2019;166:68–72.
[124] Liu J, Chen C, Feng Q, et al. Dislocation activities at the martensite phase transformation interface in metastable austenitic stainless steel: an in-situ TEM study. Mater Sci Eng A. 2017;703:236–243.
[125] Bouaziz O, Estrin Y, Brechet Y, et al. Critical grain size for dislocation storage and consequences for strain hardening of nanocrystalline materials. Scr Mater. 2010;63:477–479.
[126] Gutierrez-Urrutia I, Zaefferer S, Raabe D. The effect of grain size and grain orientation on deformation twinning in a Fe-22 wt.% Mn-0.6 wt.% C TWIP steel. Mater Sci Eng A. 2010;527:3552–3560.
[127] Park K-T, Shin DH. Microstructural interpretation of negligible strain-hardening behavior of submicrometer-grained low-carbon steel during tensile deformation. Metall Mater Trans A. 2002;33:705–707.
[128] Ueji R, Tsuchida N, Terada D, et al. Tensile properties and twinning behavior of high manganese

austenitic steel with fine-grained structure. Scr Mater. 2008;59:963–966.
[129] Tamura I. Deformation-induced martensitic transformation and transformation-induced plasticity in steels. Met Sci. 1982;16:245–253.
[130] Palumbo M. Thermodynamics of martensitic transformations in the framework of the CALPHAD approach. Calphad. 2008;32:693–708.
[131] Olson G, Cohen M. A mechanism for the strain-induced nucleation of martensitic transformations. J Less Common Met. 1972;28:107–118.
[132] Bogers AJ, Burgers WG. Partial dislocations on the {110} planes in the B.C.C. lattice and the transition of the F.C.C. into the B.C.C. lattice. Acta Metall. 1964;12:255–261.
[133] Olson G, Cohen M. A general mechanism of martensitic nucleation: Part II. FCC→ BCC and other martensitic transformations. Metall Trans A. 1976;7:1905–1914.
[134] Yang X-S, Sun S, Zhang T-Y. The mechanism of bcc α′ nucleation in single hcp ε laths in the fcc γ →hcp ε →bcc α′ martensitic phase transformation. Acta Mater. 2015;95:264–273.
[135] Fujita H, Katayama T. In-situ observation of strain-induced γ→ε→α′ and γ→α′ martensitic transformations in Fe-Cr-Ni alloys. Mater Trans JIM. 1992;33:243–252.
[136] Yang XS, Sun S, Wu XL, et al. Dissecting the mechanism of martensitic transformation via atomic-scale observations. Sci Rep. 2014;4:6141.
[137] Bracke L, Kestens L, Penning J. Transformation mechanism of a'-martensite in an austenitic Fe-Mn-C-N alloy. Scr Mater. 2007;57:385–388.
[138] Van Tol R, Kim J, Zhao L, et al. α′-Martensite formation in deep-drawn Mn-based TWIP steel. J Mater Sci. 2012;47:4845–4850.
[139] Lee S, Woo W, De Cooman BC. Analysis of the tensile behavior of 12 pct Mn multi-phase (α + γ) TWIP + TRIP steel by neutron diffraction. Metall Mater Trans A. 2016;47:2125–2140.
[140] Nimaga O, He B, Cheng G, et al. Revealing orientation-dependent martensitic transformation in a medium Mn steel by micropillar compression. Int J Plast. 2019;123:165–177.
[141] Yen H-W, Ooi SW, Eizadjou M, et al. Role of stress-assisted martensite in the design of strong ultrafine-grained duplex steels. Acta Mater. 2015;82:100–114.
[142] Field D, Garza-Martinez L, Van Aken D. Processing and properties of medium-Mn TRIP steel to obtain a two-stage TRIP behavior. Metall Mater Trans A. 2020;51:4427–4433.
[143] De Cooman BC, Gibbs P, Lee S, et al. Transmission electron microscopy analysis of yielding in ultrafine-grained medium Mn transformation-induced plasticity steel. Metall Mater Trans A. 2013;44:2563–2572.
[144] Gibbs PJ, De Cooman B, Brown DW, et al. Strain partitioning in ultra-fine grained medium-manganese transformation induced plasticity steel. Mater Sci Eng A. 2014;609:323–333.
[145] He B. On the factors governing austenite stability: intrinsic versus extrinsic. Materials (Basel). 2020;13:3440.
[146] Soleimani M, Kalhor A, Mirzadeh H. Transformation-induced plasticity (TRIP) in advanced steels: a review. Mater Sci Eng A. 2020;795:140023.
[147] Gutierrez-Urrutia I, Raabe D. Dislocation and twin substructure evolution during strain hardening of an Fe-22wt.% Mn-0.6wt.% C TWIP steel observed by electron channeling contrast imaging. Acta Mater. 2011;59:6449–6462.
[148] Bouaziz O, Guelton N. Modelling of TWIP effect on work-hardening. Mater Sci Eng A. 2001;319:246–249.
[149] Bouaziz O, Allain S, Scott C. Effect of grain and twin boundaries on the hardening mechanisms of twinning-induced plasticity steels. Scr Mater. 2008;58:484–487.
[150] Bouaziz O, Allain S, Scott C, et al. High manganese austenitic twinning induced plasticity steels: a review of the microstructure properties relationships. Curr Opin Solid State Mater Sci. 2011;15:141–168.
[151] Sohn SS, Choi K, Kwak J-H, et al. Novel ferrite-austenite duplex lightweight steel with 77% ductility by transformation induced plasticity and twinning induced plasticity mechanisms. Acta Mater. 2014;78:181–189.
[152] Lee C-Y, Jeong J, Han J, et al. Coupled strengthening in a medium manganese lightweight steel with an inhomogeneously grained structure of austenite. Acta Mater. 2015;84:1–8.
[153] Kwok T, Rahman K, Xu X, et al. Design of a high strength, high ductility 12 wt% Mn medium manganese steel with hierarchical deformation behaviour. Mater Sci Eng A. 2020;782:139258.
[154] Park TM, Jeong MS, Jung C, et al. Improved strength of a medium-Mn steel by V addition without sacrificing ductility. Mater Sci Eng A. 2021;802:140681.
[155] Tian Y, Bai Y, Zhao L, et al. A novel ultrafine-grained Fe22Mn0.6C TWIP steel with superior strength and ductility. Mater Charact. 2017;126:74–80.
[156] Gutierrez-Urrutia I, Raabe D. Grain size effect on strain hardening in twinning-induced plasticity steels. Scr Mater. 2012;66:992–996.
[157] Rahman K, Vorontsov V, Dye D. The effect of grain size on the twin initiation stress in a TWIP steel. Acta Mater. 2015;89:247–257.
[158] McCormigk P. A model for the Portevin-Le chatelier effect in substitutional alloys. Acta Metall. 1972;20:351–354.
[159] Nam J-H, Oh S-K, Park M-h, et al. The mechanism of dynamic strain aging for type A serrations in tensile curves of a medium-Mn steel. Acta Mater. 2021;206:116613.
[160] Field DM, Van Aken DC. Dynamic strain aging phenomena and tensile response of medium-Mn TRIP steel. Metall Mater Trans A. 2018;49:1152–1166.
[161] Yang F, Luo H, Pu E, et al. On the characteristics of Portevin-Le Chatelier bands in cold-rolled 7Mn steel showing transformation-induced plasticity. Int J Plast. 2018;103:188–202.
[162] Rose K, Gloverj S. A study of strain-ageing in austenite. Acta Metall. 1966;14:1505–1516.
[163] Lee S-J, Kim J, Kane SN, et al. On the origin of dynamic strain aging in twinning-induced plasticity steels. Acta Mater. 2011;59:6809–6819.
[164] Oh S-K, Kilic ME, Seol J-B, et al. The mechanism of dynamic strain aging for type A serrations in tensile flow curves of Fe-18Mn-0.55 C (wt. %) twinning-induced plasticity steel. Acta Materialia. 2020;188:366–375.

[165] Mola J, Luan G, Huang Q, et al. Dynamic strain aging mechanisms in a metastable austenitic stainless steel. Acta Mater. 2021;212:116888.
[166] Tasan CC, Diehl M, Yan D, et al. An overview of dual-phase steels: advances in microstructure-oriented processing and micromechanically guided design. Annu Rev Mater Res. 2015;45:391–431.
[167] Sodjit S, Uthaisangsuk V. Microstructure based prediction of strain hardening behavior of dual phase steels. Mater Des. 2012;41:370–379.
[168] Ashby M. Work hardening of dispersion-hardened crystals. Philos Mag. 1966;14:1157–1178.
[169] Jiang Z, Guan Z, Lian J. Effects of microstructural variables on the deformation behaviour of dual-phase steel. Mater Sci Eng A. 1995;190:55–64.
[170] Calcagnotto M, Ponge D, Demir E, et al. Orientation gradients and geometrically necessary dislocations in ultrafine grained dual-phase steels studied by 2D and 3D EBSD. Mater Sci Eng A. 2010;527:2738–2746.
[171] He B, Huang M. Strong and ductile medium Mn steel without transformation-induced plasticity effect. Mater Res Lett. 2018;6:365–371.
[172] Calcagnotto M, Adachi Y, Ponge D, et al. Deformation and fracture mechanisms in fine-and ultrafine-grained ferrite/martensite dual-phase steels and the effect of aging. Acta Mater. 2011;59:658–670.
[173] Raabe D, Sun B, Da Silva AK, et al. Current challenges and opportunities in microstructure-related properties of advanced high-strength steels. Metall Mater Trans A. 2020;51:5517–5586.
[174] Dutta A, Ponge D, Sandlöbes S, et al. Strain partitioning and strain localization in medium manganese steels measured by in situ microscopic digital image correlation. Materialia. 2019;5:100252.
[175] Cong ZH, Jia N, Sun X, et al. Stress and strain partitioning of ferrite and martensite during deformation. Metall Mater Trans A. 2009;40:1383–1387.
[176] Sun B, Fazeli F, Scott C, et al. Critical role of strain partitioning and deformation twinning on cracking phenomenon occurring during cold rolling of two duplex medium manganese steels. Scr Mater. 2017;130:49–53.
[177] Varanasi RS, Zaefferer S, Sun B, et al. Localized deformation inside the Lüders front of a medium manganese steel. Mater Sci Eng A. 2021;824:141816.
[178] Koyama M, Yamashita T, Morooka S, et al. Microstructure and plasticity evolution during Lüders deformation in an Fe-5Mn-0.1C medium-Mn steel. ISIJ Int. 2022;62:2036–2042.
[179] He BB, Liang ZY, Huang MX. Nanoindentation investigation on the initiation of yield point phenomenon in a medium Mn steel. Scr Mater. 2018;150:134–138.
[180] Wang XG, Liu CH, He BB, et al. Microscopic strain partitioning in Lüders band of an ultrafine-grained medium Mn steel. Mater Sci Eng A. 2019;761:138050.
[181] Li Z, Ding H, Misra RDK, et al. Deformation behavior in cold-rolled medium-manganese TRIP steel and effect of pre-strain on the Lüders bands. Mater Sci Eng A. 2017;679:230–239.
[182] Zhang M, Li R, Ding J, et al. In situ high-energy X-ray diffraction mapping of Lüders band propagation in medium-Mn transformation-induced plasticity steels. Mater Res Lett. 2018;6:662–667.
[183] Luo H, Dong H, Huang M. Effect of intercritical annealing on the Lüders strains of medium Mn transformation-induced plasticity steels. Mater Des. 2015;83:42–48.
[184] Steineder K, Krizan D, Schneider R, et al. On the microstructural characteristics influencing the yielding behavior of ultra-fine grained medium-Mn steels. Acta Mater. 2017;139:39–50.
[185] Cottrell AH, Bilby BA. Dislocation theory of yielding and strain ageing of iron. Proc Phys Soc London Sect A. 1949;62:49.
[186] Johnston WG, Gilman JJ. Dislocation velocities, dislocation densities and plastic flow in lithium fluoride crystals. J Appl Phys. 1959;30:129–144.
[187] Tsuji N, Ito Y, Saito Y, et al. Strength and ductility of ultrafine grained aluminum and iron produced by ARB and annealing. Scr Mater. 2002;47:893–899.
[188] Capolungo L, Spearot D, Cherkaoui M, et al. Dislocation nucleation from bicrystal interfaces and grain boundary ledges: relationship to nanocrystalline deformation. J Mech Phys Solids. 2007;55:2300–2327.
[189] Blanter MS, Golovin IS, De Batist R, et al. Effect of plastic deformation on the carbon internal friction peak in austenitic steels. Phys Status Solidi (a). 2000;178:621–632.
[190] Li YZ, Luo ZC, Liang ZY, et al. Effect of carbon on strain-rate and temperature sensitivity of twinning-induced plasticity steels: modeling and experiments. Acta Mater. 2019;165:278–293.
[191] Schneider R, Steineder K, Krizan D, et al. Effect of the heat treatment on the microstructure and mechanical properties of medium-Mn-steels. Mater Sci Technol. 2019;35:2045–2053.
[192] Lee S, Lee S-J, Santhosh Kumar S, et al. Localized deformation in multiphase, ultra-fine-grained 6 pct Mn transformation-induced plasticity steel. Metall Mater Trans A. 2011;42:3638–3651.
[193] Steineder K, Krizan D, Schneider R, et al. On the damage behavior of a 0.1C6Mn medium-Mn steel. Steel Res Int. 2018;89:1700378.
[194] Choi H, Lee S, Lee J, et al. Characterization of fracture in medium Mn steel. Mater Sci Eng A. 2017;687:200–210.
[195] Wang M-M, Tasan CC, Ponge D, et al. Nanolaminate transformation-induced plasticity–twinning-induced plasticity steel with dynamic strain partitioning and enhanced damage resistance. Acta Mater. 2015;85:216–228.
[196] Wang M, Tasan CC, Koyama M, et al. Enhancing hydrogen embrittlement resistance of lath martensite by introducing nano-films of interlath austenite. Metall Mater Trans A. 2015;46:3797–3802.
[197] Sun B, Krieger W, Rohwerder M, et al. Dependence of hydrogen embrittlement mechanisms on microstructure-driven hydrogen distribution in medium Mn steels. Acta Mater. 2020;183:313–328.
[198] Kim MT, Park TM, Baik K-H, et al. Crucial microstructural feature to determine the impact toughness of intercritically annealed medium-Mn steel with triplex-phase microstructure. Acta Mater. 2019;164:122–134.
[199] Tonizzo Q, Gourgues-Lorenzon A-F, Mazière M, et al. Microstructure, plastic flow and fracture behavior of ferrite-austenite duplex low density medium Mn steel. Mater Sci Eng A. 2017;706:217–226.
[200] Sun B, Aydin H, Fazeli F, et al. Microstructure evolution of a medium manganese steel during

thermomechanical processing. Metall Mater Trans A. 2016;47:1782–1791.
[201] Sohn SS, Lee B-J, Kwak J-H, et al. Effects of annealing treatment prior to cold rolling on the edge cracking phenomenon of ferritic lightweight steel. Metall Mater Trans A. 2014;45:3844–3856.
[202] Han J, Nam J-H, Lee Y-K. The mechanism of hydrogen embrittlement in intercritically annealed medium Mn TRIP steel. Acta Mater. 2016;113:1–10.
[203] Fielding L, Song EJ, Han D-K, et al. Hydrogen diffusion and the percolation of austenite in nanostructured bainitic steel. Proc R. Soc A Math Phys Eng Sci. 2014;470:20140108.
[204] Dong X, Wang D, Thoudden-Sukumar P, et al. Hydrogen-associated decohesion and localized plasticity in a high-Mn and high-Al two-phase lightweight steel. Acta Mater. 2022;239:118296.
[205] Moyer J, Ansell G. The volume expansion accompanying the martensite transformation in iron-carbon alloys. Metall Trans A. 1975;6:1785.
[206] Hornbogen E. Martensitic transformation at a propagating crack. Acta Metall. 1978;26:147–152.
[207] Evans AG, Cannon R. Toughening of brittle solids by martensitic transformations. Acta Metall. 1986;34:761–800.
[208] Antolovich SD, Singh B. On the toughness increment associated with the austenite to martensite phase transformation in TRIP steels. Metall Mater Trans B. 1971;2:2135–2141.
[209] Wang X, Liu C, Sun B, et al. The dual role of martensitic transformation in fatigue crack growth. Proc Natl Acad Sci USA. 2022;119:e2110139119.
[210] Krauss G. Martensite in steel: strength and structure. Mater Sci Eng A. 1999;273:40–57.
[211] Raabe D, Li Z, Ponge D. Metastability alloy design. MRS Bull. 2019;44:266–272.
[212] Sun B, Wang D, Lu X, et al. Current challenges and opportunities toward understanding Hydrogen Embrittlement mechanisms in advanced high-strength steels: a review. Acta Metall Sinica (English Lett). 2021;6:741–754.
[213] Ryu JH, Chun YS, Lee CS, et al. Effect of deformation on hydrogen trapping and effusion in TRIP-assisted steel. Acta Mater. 2012;60:4085–4092.
[214] Krauss G. Deformation and fracture in martensitic carbon steels tempered at low temperatures. Metall Mater Trans B. 2001;32:205–221.
[215] Raabe D, Herbig M, Sandlöbes S, et al. Grain boundary segregation engineering in metallic alloys: a pathway to the design of interfaces. Curr Opin Solid State Mater Sci. 2014;18:253–261.
[216] Seah M. Adsorption-induced interface decohesion. Acta Metall. 1980;28:955–962.
[217] Kuzmina M, Ponge D, Raabe D. Grain boundary segregation engineering and austenite reversion turn embrittlement into toughness: example of a 9 wt.% medium Mn steel. Acta Mater. 2015;86:182–192.
[218] Yu J, McMahon C. The effects of composition and carbide precipitation on temper embrittlement of 2.25 Cr-1 Mo steel: Part II. Effects of Mn and Si. Metall Trans A. 1980;11:291.
[219] Guttmann M, Dumoulin P, Wayman M. The thermodynamics of interactive co-segregation of phosphorus and alloying elements in iron and temper-brittle steels. Metall Trans A. 1982;13:1693–1711.
[220] Ito K, Sawada H, Ogata S. First-principles study on the grain boundary embrittlement of bcc-Fe by Mn segregation. Phys Rev Mater. 2019;3:013609.
[221] Lai Q, Bouaziz O, Gouné M, et al. Damage and fracture of dual-phase steels: influence of martensite volume fraction. Mater Sci Eng A. 2015;646:322–331.
[222] Calcagnotto M, Ponge D, Raabe D. On the effect of manganese on grain size stability and hardenability in ultrafine-grained ferrite/martensite dual-phase steels. Metall Mater Trans A. 2012;43:37–46.
[223] Gamsjäger E, Wiessner M, Schider S, et al. Analysis of the mobility of migrating austenite–ferrite interfaces. Philos Mag. 2015;95:2899–2917.
[224] Zhang J, Huang M, Sun B, et al. Critical role of Lüders banding in hydrogen embrittlement susceptibility of medium Mn steels. Scr Mater. 2021;190:32–37.
[225] Cao W, Zhang M, Huang C, et al. Ultrahigh Charpy impact toughness (~450J) achieved in high strength ferrite/martensite laminated steels. Sci Rep. 2017;7:41459.
[226] Kimura Y, Inoue T, Yin F, et al. Inverse temperature dependence of toughness in an ultrafine grain-structure steel. Science. 2008;320:1057–1060.
[227] Jeong I, Ryu KM, Lee DG, et al. Austenite morphology and resistance to hydrogen embrittlement in medium Mn transformation-induced plasticity steel. Scr Mater. 2019;169:52–56.
[228] Matlock DK, Speer JG. Third generation of AHSS: microstructure design concepts. In: Arunansu Haldar, Satyam Suwas, Debashish Bhattacharjee, editors. Microstructure and texture in steels. Springer; 2009. p. 185–205.
[229] Liu S, Xiong Z, Guo H, et al. The significance of multi-step partitioning: processing-structure-property relationship in governing high strength-high ductility combination in medium-manganese steels. Acta Mater. 2017;124:159–172.
[230] He B, Liu L, Huang M. Room-temperature quenching and partitioning steel. Metall Mater Trans A. 2018;49:3167–3172.
[231] Speer J. Phase transformations in quenched and partitioned steels. In: Elena Pereloma and David V. Edmonds, editors. Phase transformations in steels. Elsevier; 2012. p. 247–270.
[232] Speer JG, De Moor E, Clarke AJ. Critical assessment 7: quenching and partitioning. Mater Sci Technol. 2015;31:3–9.
[233] Dong H, Cao W, Liu Z, et al. The medium manganese steels: phenomena and industry potentials. Proceedings of HMnS2011 Conference, Seoul, Korea; 2011.
[234] Shi J, Sun X, Wang M, et al. Enhanced work-hardening behavior and mechanical properties in ultrafine-grained steels with large-fractioned metastable austenite. Scr Mater. 2010;63:815–818.
[235] Zhang Y, Wang L, Findley KO, et al. Influence of temperature and grain size on austenite stability in medium manganese steels. Metall Mater Trans A. 2017;48:2140–2149.
[236] Han Q, Zhang Y, Wang L. Effect of annealing time on microstructural evolution and deformation characteristics in 10Mn1.5Al TRIP steel. Metall Mater Trans A. 2015;46:1917–1926.
[237] Jun HJ, Yakubovsky O, Fonstein N. On stability of retained austenite in medium Mn TRIP steels, Proceedings of HMnS2011 Conference, Seoul, Korea; 2011.

[238] Shao C, Hui W, Zhang Y, et al. Microstructure and mechanical properties of hot-rolled medium-Mn steel containing 3% aluminum. Mater Sci Eng A. 2017;682:45–53.
[239] Lee S, Lee K, De Cooman BC. Observation of the TWIP + TRIP plasticity-enhancement mechanism in Al-Added 6 Wt Pct medium Mn steel. Metall Mater Trans A. 2015;46:2356–2363.
[240] Wang C, Cao W, Shi J, et al. Deformation microstructures and strengthening mechanisms of an ultrafine grained duplex medium-Mn steel. Mater Sci Eng A. 2013;562:89–95.
[241] Cho L, Seo EJ, De Cooman BC. Near-Ac3 austenitized ultra-fine-grained quenching and partitioning (Q&P) steel. Scr Mater. 2016;123:69–72.
[242] Zhao Z, Liang J, Zhao A, et al. Effects of the austenitizing temperature on the mechanical properties of cold-rolled medium-Mn steel system. J Alloys Compd. 2017;691:51–59.
[243] Tsuchiyama T, Inoue T, Tobata J, et al. Microstructure and mechanical properties of a medium manganese steel treated with interrupted quenching and intercritical annealing. Scr Mater. 2016;122:36–39.
[244] Heo Y-U, Kim DH, Heo NH, et al. Deformation behavior in medium Mn steel of nanometer-sized α′+ γ lamellar structure. Metall Mater Trans A. 2016;47:6004–6016.
[245] Cooman BC, Lee SJ, Shin S, et al. Combined intercritical annealing and Q&P processing of medium Mn steel. Metall Mater Trans A. 2016;1:39–45.
[246] Hu B, He B, Cheng G, et al. Super-high-strength and formable medium Mn steel manufactured by warm rolling process. Acta Mater. 2019;174:131–141.
[247] He B, Luo H, Huang M. Experimental investigation on a novel medium Mn steel combining transformation-induced plasticity and twinning-induced plasticity effects. Int J Plast. 2016;78:173–186.
[248] Aranas Jr C, Wang T, Jonas JJ. Effect of interpass time on the dynamic transformation of a plain C–Mn and a Nb microalloyed steel. ISIJ Int. 2015;55:647–654.
[249] Song H, Sohn SS, Kwak J-H, et al. Effect of austenite stability on microstructural evolution and tensile properties in intercritically annealed medium-Mn lightweight steels. Metall Mater Trans A. 2016;47:2674–2685.
[250] Zhu Y, Ameyama K, Anderson PM, et al. Heterostructured materials: superior properties from hetero-zone interaction. Mater Res Lett. 2021;9:1–31.
[251] Lee S, Woo W, De Cooman BC. Analysis of the plasticity-enhancing mechanisms in 12 pct Mn austenoferritic steel by in Situ neutron diffraction. Metall Mater Trans A. 2014;45:5823–5828.
[252] Han J, Lee Y-K. The effects of the heating rate on the reverse transformation mechanism and the phase stability of reverted austenite in medium Mn steels. Acta Mater. 2014;67:354–361.
[253] Chin K-G, Kang C-Y, Shin SY, et al. Effects of Al addition on deformation and fracture mechanisms in two high manganese TWIP steels. Mater Sci Eng A. 2011;528:2922–2928.
[254] Curtze S, Kuokkala V-T. Dependence of tensile deformation behavior of TWIP steels on stacking fault energy, temperature and strain rate. Acta Mater. 2010;58:5129–5141.
[255] Kang S, Jung Y-S, Jun J-H, et al. Effects of recrystallization annealing temperature on carbide precipitation, microstructure, and mechanical properties in Fe-18Mn-0.6 C-1.5 Al TWIP steel. Mater Sci Eng A. 2010;527:745–751.
[256] Kwon O. Development of high performance high manganese TWIP steels in POSCO. Proceedings of HMnS2011 Conference, Seoul, Korea; 2011.
[257] Opbroek E. Advanced high strength steel (AHSS) application guidelines: version 4.1. Brussels: World Steel Association; 2009.
[258] Otto DJM, Schmidt-Juergensen R, Springub B, et al. HSD® - steels - optimized twip steels. Proceedings of HMnS2011 Conference, Seoul, Korea; 2011.
[259] Grässel O, Frommeyer G. Effect of martensitic phase transformation and deformation twinning on mechanical properties of Fe-Mn-Si-AI steels. Mater Sci Technol. 1998;14:1213–1217.
[260] Weng Y, Dong H, Gan Y. Advanced steels: the recent scenario in steel science and technology. Springer; 2011.
[261] Cho K, Redkin K, Hua M, et al. Recent development of Nb-containing DP590, DP780 and DP980 steels for production on continuous galvanizing lines. In: Yuqing Weng, Han Dong, Yong Gan, editors. Advanced steels. Springer; 2011. p. 177–185.
[262] Song H, Lee SG, Sohn SS, et al. Effect of strain-induced age hardening on yield strength improvement in ferrite-austenite duplex lightweight steels. Metall Mater Trans A. 2016;47:5372–5382.
[263] Hu XH, Sun X, Hector LG, et al. Individual phase constitutive properties of a TRIP-assisted QP980 steel from a combined synchrotron X-ray diffraction and crystal plasticity approach. Acta Mater. 2017;132:230–244.
[264] Otto M. Fe-Mn-Al-Si-steels, lightweight potential for cars, trucks and trains. Young. 2017;80:30.
[265] Choi JK, Lee S-G, Park Y-H, et al. High manganese austenitic steel for cryogenic applications, Proceedings of the Twenty-Second International Offshore and Polar Engineering Conference; 2012, OnePetro.
[266] Steineder K, Krizan D, Schickinger M, et al. Wärmebehandlungsoptionen von medium-Mn-Stählen für den (Automobil-)Leichtbau. BHM Berg-Huettenmaenn Monatsh. 2019;164:379–384.
[267] Bhadhon KM, Wang X, McNally EA, et al. Effect of intercritical annealing parameters and starting microstructure on the microstructural evolution and mechanical properties of a medium-Mn third generation advanced high strength steel. Metals. 2022;12:356.
[268] Cai Z, Zhang D, Ma L, et al. Competing deformation mechanisms in an austenite-ferrite medium-Mn steel at different strain rates. Mater Sci Eng A. 2021;818:141357.
[269] Benzing JT, Luecke WE, Mates S, et al. Intercritical annealing to achieve a positive strain-rate sensitivity of mechanical properties and suppression of macroscopic plastic instabilities in multi-phase medium-Mn steels. Mater Sci Eng A. 2021;803:140469.
[270] Sarmast-Ghahfarokhi S, Zhang S, Midawi AR, et al. The failure mechanism of resistance spot welded third-generation medium-Mn steel during shear-tension loading. J Manuf Process. 2022;79:520–531.
[271] Lun N, Saha D, Macwan A, et al. Microstructure and mechanical properties of fibre laser welded medium manganese TRIP steel. Mater Des. 2017;131:450–459.
[272] DiGiovanni C, Kalashami AG, Goodwin F, et al. Occurrence of sub-critical heat affected zone liquid metal embrittlement in joining of advanced high strength steel. J Mater Process Technol. 2021;288:116917.